

**EPITAXIAL GROWTH OF LANTHANIDE-DOPED
UPCONVERSION CRYSTALS**

YUHAI ZHANG

National University of Singapore

2015

EPITAXIAL GROWTH OF LANTHANIDE-DOPED
UPCONVERSION CRYSTALS

YUHAI ZHANG

(M.Eng., Kyungwon University)

A THESIS SUBMITTED
FOR THE DEGREE OF DOCTOR OF
PHILOSOPHY

DEPARTMENT OF CHEMISTRY

NATIONAL UNIVERSITY OF SINGAPORE

2015

Declaration

I hereby declare that this thesis is my original work and it has been written by me in its entirety, under the supervision of Associate Professor Xiaogang Liu, (in the laboratory S8-05-14), Chemistry Department, National University of Singapore, between August 2011 and July 2015.

I have duly acknowledged all the sources of information which have been used in the thesis.

This thesis has also not been submitted for any degree in any university previously.

The content of the thesis has been partly published in:

- 1) Subwavelength imaging through ion-beam-induced upconversion.

Mi, Z., **Zhang, Y. (co-first-author)**, Vanga, S., Chen, C., Tan, H., Watt, F. *, Liu, X. *, & Bettiol, A. A. * *Nature Communications*. **2015**, in press.

- 2) Multicolor barcoding in a single upconversion crystal.

Zhang, Y., Zhang, L., Deng, R., Tian, J., Zong, Y., Jin, D., & Liu, X.* *Journal of the American Chemical Society*, **2014**, 136, 4893-4896.

- 3) Nanocrystals: Shining a light on upconversion.

Zhang, Y., & Liu, X.* *Nature Nanotechnology*, **2013**, 8, 702-703.

Zhang Yuhai

Name

Signature

Date

Acknowledgements

This dissertation would not been finished without the generous support from many people, to whom I would like to deliver my acknowledgements here.

First of all, I would like to express my sincere gratitude to my advisor, Dr. Xiaogang Liu, for his guidance, motivation, and support during my PhD career at National University of Singapore. I appreciate his forgiveness on my rookie mistakes in the beginning of PhD career, his trust for allowing me to spend a large amount of funding on my project, and his harsh but efficient training on my academic writing skills. I also thank him for giving me so many opportunities to collaborate with top scientists in upconversion community including Dr. Dayong Jin from Macquarie University, and Dr. Daniel Jaque García from Universidad Autónoma de Madrid. Hereby, I would like give a big thank you to Dayong and Daniel for their generous financial support on my travelling and joint-research abroad.

I owe a big thank you to all the members in Dr. Liu's group. It was a wonderful experience to work with so many dedicated young researchers of particular expertise in science. More importantly, most of the group members love playing badminton, which indeed enriches our daily life. My greatest gratitude goes to my dear badminton partners and labmates, Dr. Zaifa Pan, Dr. Xian Qin, Mr. Qiang Sun, Mr. Xiaowang Liu, Dr. Suli Wu, Dr. Xiyang Li, Dr. Sanyang Han, Mr. Xiao Zeng, Dr. Yali Yuan, Dr. Xiaoji Xie and Dr. Xuejia Xue. You all know how great it feels when playing in the badminton court after 8-hour hard working in the lab. I would like give a special thank you to Dr. Renren Deng, who always has a unique insight into my concern and prepares to share. I would never forget all those useful discussions in fundamental science with my lab friends, including Dr. Yu Wang, Mr. Liangliang Liang, Dr. Zhongfu An, Mr. Yiming Wu, Ms. Jiahui Xu, Dr. Weifeng Yang, Dr. Qiushui Chen, and Dr. Bo Zhou.

Particular thanks go to my oversea collaborators, including Dr. Lixin Zhang, Dr. Patricia Haro González, and Dr. Yinlan Ruan, for their kindness to help me in understanding optical instrumentations. I would also like to thank Prof. Thorsten Wohland, Prof. Frank Watt, Mr. Zhaohong Mi, three domestic physicians who taught me a lot on particle-beams and optics

alignment. Particularly, I can't finish chapter 5 without the collaboration with Mr. Zhaohong Mi.

Last but not least, I would like to express my deepest gratitude towards my father, mother and my beloved wife, for their constant support on every single decision that I made during my PhD career. They may not know what I am working on for research, but they do know who I am.

Table of Contents

| | |
|--|------------|
| Declaration | I |
| Acknowledgements | III |
| Table of Contents | V |
| Summary | IX |
| List of Figures | XI |
| 1 CHAPTER 1 | 1 |
| Brief Introduction of Lanthanide-Doped Upconversion Materials and Crystal Growth Techniques | 1 |
| 1.1 Introduction | 2 |
| 1.1.1 Luminescence from Lanthanide-doped Materials | 2 |
| 1.1.2 Upconversion Luminescence | 5 |
| 1.1.3 Upconversion Bulk-, Micro-, and Nano-crystals | 8 |
| 1.1.4 Seeded-Crystal Growth | 10 |
| 1.2 Scope of the Thesis | 10 |
| 1.3 References | 12 |
| 2 CHAPTER 2 | 15 |
| Spectroscopic Evidence for Lanthanide Ion Diffusion In NaYF₄ Nanocrystals | 15 |
| 2.1 Introduction | 16 |
| 2.2 Materials and Methods | 17 |
| 2.2.1 Reagents | 17 |
| 2.2.2 Synthesis of NaYF ₄ :Tm (30 mol%) Core Nanocrystals | 17 |
| 2.2.3 Synthesis of NaYF ₄ :Tm@NaYF ₄ :Yb Nanocrystals | 18 |
| 2.2.4 Synthesis of NaYF ₄ :Tm@NaYF ₄ @NaYF ₄ :Yb Nanocrystals | 18 |
| 2.2.5 Diffusion Experiment for Core@shell Nanocrystals | 19 |
| 2.2.6 Physical Measurements | 19 |
| 2.3 Results and Discussion | 20 |
| 2.3.1 Zero-dimensional Epitaxy of NaYF ₄ Nanocrystals | 20 |
| 2.3.2 Upconversion Luminescence Spectra of Nanocrystals before Diffusion | 20 |
| 2.3.3 Upconversion Luminescence Spectra of Nanocrystals after Diffusion | 26 |
| 2.3.4 Ostwald Ripening | 32 |
| 2.4 Conclusion | 32 |
| 2.5 References | 33 |
| 3 CHAPTER 3 | 35 |
| Epitaxy in One-Dimensional Upconversion Crystals: Multicolor Barcoding on A Single Particle | 35 |
| 3.1 Introduction | 36 |
| 3.2 Materials and Methods | 37 |
| 3.2.1 Reagents | 37 |
| 3.2.2 Synthesis of β -NaYF ₄ Microrod | 37 |

| | | |
|------------|--|-----------|
| 3.2.3 | Synthesis of α -NaYF ₄ Nanoparticle..... | 37 |
| 3.2.4 | Synthesis of β -NaYF ₄ Microrods with Dual-Color Emissions | 38 |
| 3.2.5 | Physical Measurements | 38 |
| 3.2.6 | Luminescence Lifetime Measurement of a Single Microrod..... | 38 |
| 3.2.7 | Preparation of Microrod-based Ink for Security Printing | 41 |
| 3.2.8 | Cell Coding and Tracking | 41 |
| 3.3 | Results and Discussion | 43 |
| 3.3.1 | Resolution of Optical Microscope | 43 |
| 3.3.2 | Epitaxy Design and Characterization | 43 |
| 3.3.3 | General Considerations on Epitaxy | 49 |
| 3.3.4 | Characterization of Dual-Color-Banded Barcodes | 50 |
| 3.3.5 | Epitaxial Growth Monitoring | 50 |
| 3.3.6 | Energy Transfer at the Junction | 57 |
| 3.3.7 | Barcoding Crystals for Anti-counterfeiting Application | 60 |
| 3.3.8 | Barcoding Crystals for Cell Labelling | 63 |
| 3.4 | Conclusion..... | 63 |
| 3.5 | References..... | 64 |
| 4 | CHAPTER 4 | 67 |
| | Epitaxy Habits In NaLnF₄ System Revealed for Color Multiplexing on Single-Crystal Level..... | 67 |
| 4.1 | Introduction | 68 |
| 4.2 | Materials and Methods..... | 69 |
| 4.2.1 | Reagents | 69 |
| 4.2.2 | Synthetic Methods for Particles of Different Sizes..... | 69 |
| 4.2.3 | Seeded Epitaxial Growth of NaLnF ₄ Crystals | 70 |
| 4.2.4 | Epitaxy Along <i>a</i> -axis (<i>a</i> -condition) | 72 |
| 4.2.5 | Epitaxy Along <i>c</i> -axis (<i>c</i> -condition)..... | 72 |
| 4.2.6 | Physical Measurements | 72 |
| 4.3 | Results and Discussion | 74 |
| 4.3.1 | Seeding Crystals | 74 |
| 4.3.2 | Epitaxy on Seeding Crystals..... | 78 |
| 4.3.3 | Kinetics and Thermodynamics of Epitaxy..... | 83 |
| 4.3.4 | Epitaxy Orientation Control | 89 |
| 4.4 | Conclusion | 92 |
| 4.5 | References..... | 93 |
| 5 | CHAPTER 5 | 95 |
| | Subwavelength Imaging through Ion-Beam Induced Upconversion Luminescence | 95 |
| 5.1 | Introduction | 96 |
| 5.2 | Materials and Methods..... | 97 |
| 5.2.1 | Reagents | 97 |
| 5.2.2 | Synthesis of NaYF ₄ :Yb/Tm (x/y mol%) Nanorods | 97 |
| 5.2.3 | Synthesis of NaYF ₄ :Yb/Tm (60/2 mol%) Nanoparticles..... | 98 |

| | | |
|-------------|---|------------|
| 5.2.4 | Physical Measurements | 98 |
| 5.2.5 | Ion-beam Microscopy Construction | 99 |
| 5.3 | Results and Discussion | 102 |
| 5.3.1 | Theoretical Simulation on Energy Distribution of Ionized Electrons..... | 102 |
| 5.3.2 | Experimental Evidence for Ionoluminescence | 102 |
| 5.3.3 | Subwavelength Imaging of Upconversion Nanorods | 107 |
| 5.3.4 | Subwavelength Imaging of Upconversion Nanocrystals in Cell | 109 |
| 5.4 | Conclusion | 111 |
| 5.5 | References..... | 112 |
| 6 | CHAPTER 6 | 115 |
| | Conclusion and Outlook | 115 |
| I. | Curriculum Vitae | 117 |
| II. | List of Publications | 119 |
| III. | Symposia/Conferences Attended | 121 |

Summary

Crystal epitaxy plays a pivotal role in nanotechnology due to its ability to generate a broad class of heterogeneous materials, including core-shell semiconductor nanoparticles, segmented nanowires, sandwiched thin films, and hybrid nanoarrays. In particular, epitaxy in lanthanide-doped crystal system has not only enabled the fine control over emission intensity and colors, but also unveiled a new energy upconversion mechanism, i.e., the energy migration upconversion. The primary work of this thesis is focused on the study of epitaxial growth of NaLnF_4 crystals, including zero-dimensional (0-D), one-dimensional (1-D), and two-dimensional (2-D) crystals. These epitaxy experiments readily afford a large amount of heterogeneous crystals in a bottom-up synthetic manner. The usefulness of these heterogeneous single-crystals was demonstrated in each individual chapter.

In Chapter 2, the epitaxy of NaYF_4 nanocrystals was performed in an oil-based coprecipitation system. 0-D epitaxy was termed because the size of those nanocrystals was substantially small (10~30 nm in diameter). The resulted core@shell nanocrystals were used as a platform to study the atomic diffusion in crystal lattice;

In Chapter 3, the epitaxy of NaYF_4 nanorods was conducted in a hydrothermal reactor. By using a nanorod as template, the epitaxial segments can be instantly verified through the use of a conventional optical microscope coupling with a 980-nm laser. Due to the encoded feature of microstructure, the resulted 1-D banded multicolor crystals were used for anti-counterfeiting purpose.

In Chapter 4, I examined the epitaxy behavior of several lanthanide-doped crystal systems, including NaYF_4 , NaYbF_4 , and NaLuF_4 . By using various hydrothermal conditions, the control over epitaxy dimension and orientation was achieved. Based on a series of experiments involving kinetic and thermodynamic studies, two epitaxy habits were generalized.

In Chapter 5, a super-resolution technique by using an ion-beam as excitation source was introduced. Due to the high penetration ability of ion-beam, the lanthanide-doped nanocrystals inside a whole cell can be excited, and therefore imaged in a scanning manner.

The resolution of the constructed microscope is determined to be 28-nm, exhibiting a 10-fold enhancement when compared to regular optical microscope.

The findings presented in this thesis enable a fine control over epitaxy behavior in NaLnF_4 crystal systems, providing a flexible method for making upconversion heterogeneous structure on single-crystal level.

List of Figures

| | |
|--|----|
| Figure 1.1 Energy level diagram for trivalent lanthanide ions doped in a low symmetry LaF_3 crystal..... | 4 |
| Figure 1.2 Several unique properties of the luminescence from lanthanide-doped materials..... | 7 |
| Figure 1.3 Images of single crystals of hexagonal-phase NaLnF_4 with various sizes..... | 8 |
| Figure 2.1 Schematic showing the two-step synthetic method..... | 22 |
| Figure 2.2 Synthetic scheme and TEM image of the $\text{NaYF}_4:\text{Tm}(30 \text{ mol}\% @\text{NaYF}_4:\text{Yb}(30 \text{ mol}\%))$ nanocrystals..... | 23 |
| Figure 2.3 Synthetic scheme and TEM image of $\text{NaYF}_4:\text{Tm}(30 \text{ mol}\%)@ \text{NaYF}_4 @\text{NaYF}_4:\text{Yb}(30 \text{ mol}\%)$ heterogeneous structure..... | 24 |
| Figure 2.4 Room temperature upconversion spectra of as-synthesized nanocrystals under an excitation of 980-nm laser..... | 25 |
| Figure 2.5 Schematic showing the diffusion experimentation..... | 28 |
| Figure 2.6 The integrated intensity of upconversion luminescence of homogeneous nanocrystals evolves against diffusion time..... | 29 |
| Figure 2.7 A control experiment shows that the morphology of $\text{NaYF}_4:\text{Tm}(30 \text{ mol}\%)@ \text{NaYF}_4:\text{Yb}(30 \text{ mol}\%)$ core@shell nanocrystals is maintained during thermal diffusion process..... | 30 |
| Figure 2.8 A control experiment showing the diffusion of Er ions in crystal lattice..... | 31 |
| Figure 3.1 Simplified layout of a home-made upconversion characterization system..... | 40 |
| Figure 3.2 The point spread function (red line) of the intensity profile is fitted with Gaussian function (green line), and the full width at half maximum (FWHM) is taken as the resolution..... | 45 |
| Figure 3.3 XRD characterization and TEM image of the as-synthesized cubic phase | |

| | |
|---|----|
| NaYF ₄ :Yb/Er nanoparticles..... | 46 |
| Figure 3.4 Typical SEM and TEM image of the hexagonal-phase NaYF ₄ :Yb/Er (5/0.05 mol%) nanorods..... | 47 |
| Figure 3.5 Room-temperature upconversion emission spectra and micrographs of hexagonal-phase NaYF ₄ microrods with different Yb/Er/Tm doping compositions.. | 48 |
| Figure 3.6 Design of the bottom-up synthesis of a dual-color-banded hexagonal-phase NaYF ₄ :Yb/Er upconversion microrod through an oriented epitaxial growth method..... | 49 |
| Figure 3.7 Characterization of dual-color emitting NaYF ₄ microrods after the end-on epitaxial growth over NaYF ₄ :Yb/Er (5/0.05 mol%, green) nanorods with cubic-phase NaYF ₄ :Yb/Er (50/0.05 mol%, red) precursors..... | 52 |
| Figure 3.8 Spot scan elemental analysis of an individual dual-color-emitting NaYF ₄ microrod..... | 53 |
| Figure 3.9 Characterization of the epitaxial junction of a single dual-color NaYF ₄ microrod..... | 54 |
| Figure 3.10 XRD pattern and upconversion emission spectra of the tip-modified NaYF ₄ microrods..... | 55 |
| Figure 3.11 Upconversion micrographs of the as-synthesized dual-color-emitting microrods prepared through the use of different precursors..... | 56 |
| Figure 3.12 Lifetime measurement of a single upconversion microrod by using a confocal microscope..... | 58 |
| Figure 3.13 Plausible energy transfer pathways between excited Er ³⁺ and Tm ³⁺ at the tip-junction of a dual-color-emitting (YBY) microrod..... | 59 |
| Figure 3.14 Security ink comprising NaYF ₄ :Yb/Er (10/0.05 mol%) microrods is used for anticounterfeiting purpose..... | 61 |
| Figure 3.15 A single living HeLa cell labeled with green-emitting upconversion microrods..... | 62 |

| | |
|---|-----|
| Figure 4.1 Typical TEM images showing the as-synthesize NaYF ₄ nanocrystals with a feature size of 47 nm and 158 nm, respectively. | 75 |
| Figure 4.2 Typical SEM images of as-synthesized NaLnF ₄ hexagon-like crystals by using a hydrothermal reaction | 76 |
| Figure 4.3 Rod-like NaLnF ₄ crystals of various lengths synthesized through a hydrothermal method..... | 77 |
| Figure 4.4 Characterization of two-dimensional epitaxy of NaYF ₄ microcrystals using NaLuF ₄ precursor. | 80 |
| Figure 4.5 TEM image and corresponding elemental mapping images of NaYbF ₄ @NaLuF ₄ core@shell crystals..... | 81 |
| Figure 4.6 Typical SEM image and corresponding elemental mapping images of NaYF ₄ :Yb/Er (20/0.5 mol%)@NaLuF ₄ :Yb/Tm (5/0.5 mol%) core@shell crystals. | 82 |
| Figure 4.7 Kinetic study of a typical epitaxy growth in NaYbF ₄ crystal system based on XRD patterns evolution against reaction time..... | 84 |
| Figure 4.8 Thermodynamic study of a typical epitaxy growth in NaYbF ₄ crystal system | 86 |
| Figure 4.9 Control experiment shows the existence of a maximum size around 3.5 μm in NaLuF ₄ crystals epitaxy system. | 87 |
| Figure 4.10 Kinetic and thermodynamic study of a typical epitaxy growth in NaYbF ₄ system, showing a maximal crystal size limited by seedless hydrothermal condition..... | 88 |
| Figure 4.11 Epitaxy orientation control over <i>c</i> axis and <i>a</i> axis when using NaYF ₄ nanorods as the seeding crystals..... | 90 |
| Figure 4.12 Construction of multicolor NaLnF ₄ crystals by multi-step epitaxy with control over orientation. | 91 |
| Figure 5.1 Experimental set-up and emission mechanism of lanthanide-doped nanocrystals by using a α-particle beam as excitation source..... | 100 |

| | |
|---|-----|
| Figure 5.2 Schematic showing the different penetration ability of slow (30 keV) and fast (1.6 MeV) α -beam and photograph of the home-made α -beam microscope..... | 101 |
| Figure 5.3 Superior prospect of α -beam excitation over 980-nm laser for excitation purpose. | 104 |
| Figure 5.4 Spectral verification and optimization of doping concentration for maximum luminescence output. | 105 |
| Figure 5.5 Spectroscopic investigation of upconversion luminescence in NaYF ₄ :Yb/Tm crystals under α -beam excitation. | 106 |
| Figure 5.6 Ionoluminescence imaging and ionobleaching of NaYF ₄ :Yb/Tm (60/2 mol%) nanorods..... | 108 |
| Figure 5.7 Simultaneous structure and fluorescence imaging in a single Hela cancer cell. | 110 |

1 CHAPTER 1

Brief Introduction of Lanthanide-doped Upconversion Materials and Crystal Growth Techniques

1.1 Introduction

1.1.1 Luminescence from Lanthanide-doped Materials

The lanthanide series of chemical elements comprises 15 metallic elements with atomic number increasing from 57 to 71, including lanthanum (La), cerium (Ce), praseodymium (Pr), neodymium (Nd), promethium (Pm), samarium (Sm), europium (Eu), gadolinium (Gd), terbium (Tb), dysprosium (Dy), holmium (Ho), erbium (Er), thulium (Tm), ytterbium (Yb), and lutetium (Lu). These elements have been found of unique chemical and physical properties, and therefore have been widely used in practical industries as indispensable units, such as catalysts, superconductors, capacities, and lasers. In particular, the featured 4f-4f electron transition of lanthanide ions gives rise to a rich set of optical emissions spanning from ultraviolet-visible (UV-Vis) to near infrared (NIR) that have constantly drawn extensive attention in the past century (Figure 1.1). Back to the 1880s, the luminescence of the lanthanide has been used as an analytical tool by scientists to examine the purity of crystals and to identify possible new elements¹. In 1937, the ending of exploratory phase in lanthanide optical properties was benchmarked by an article: The Puzzle of Rare Earth Spectra in Solids, after which the lanthanide luminescence began to be widely utilized in daily life².

To obtain a decent luminescence from lanthanide ions, researchers usually dope a trace amount of such ions into a crystal or a glass matrix, to form a so-called lanthanide-doped material. The crystal or glass matrix is termed as host material, while the dopant ions are termed as activators. Unlike the fluorescence of semiconductor materials, the luminescence of lanthanide-doped materials is not generated from the bandgap of host material, but from the trivial amount of lanthanide dopants. The luminescence from lanthanide activators holds several unique features superior to that from conventional fluorescent probes like quantum dots or organic dyes^{3,6}. First, the emission bands are generally narrow and sharp, typically 5 to 15 nm in full-width-at-half-maximum (Figure 1.2a); second, the lifetimes of the excited states are in the range of 0.1~10 ms, several orders of magnitude longer than those of quantum dots (Figure 1.2c); third, the emission profile exhibits a multi-peak style, or a so-called fingerprint

CHAPTER 1

feature. Broadly, these features are universal for all those lanthanide-based luminescence, including downshifting, quantum cutting, and upconversion luminescence. Due to limited time, only the upconversion luminescence will be covered in this thesis. Readers who are interested in quantum cutting or downshifting luminescence may refer to reviews elsewhere^{3,4}.

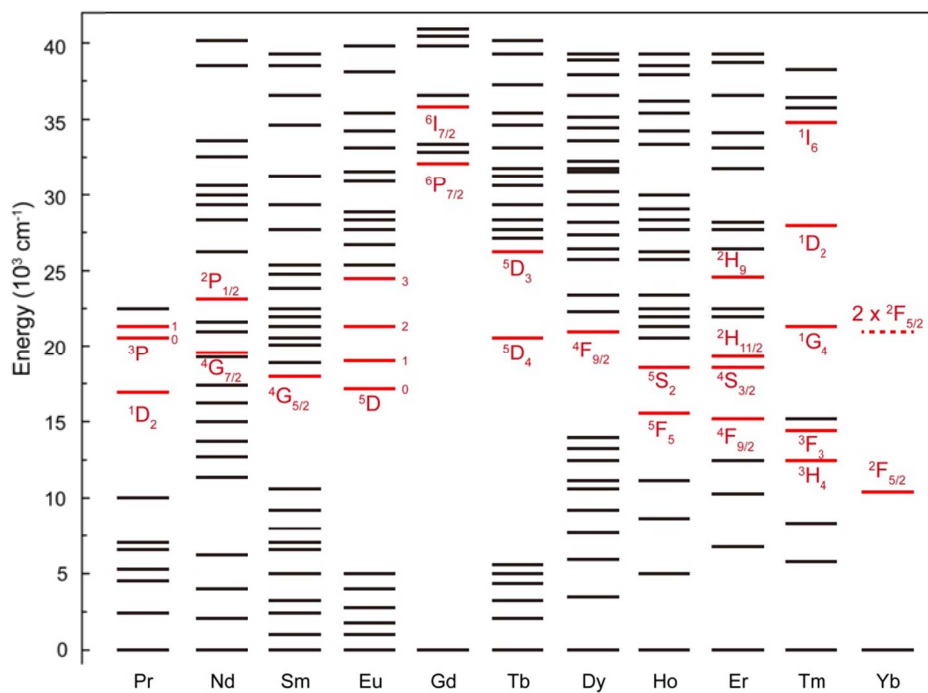


Figure 1.1 Energy level diagram for trivalent lanthanide ions doped in a low symmetry crystal, LaF₃. The primary emissive energy levels are highlighted in red color.

1.1.2 Upconversion Luminescence

Photon upconversion is a nonlinear optical process that can convert two or more lower-energy photons into one higher-energy photon. In recent decades, the photon upconversion has attracted considerable attention due to its wide application in many areas, such as laser making, data storage, 3D display, and biomedicine^{5,6,7}. In particular, the use of a near infrared (NIR) laser as the excitation source makes upconversion luminescence into an extraordinary legitimate signal for deep tissue imaging due to the biological window. Initially, organic dyes or quantum dots were used as deep tissue luminescent probe to generate upconversion emission through a two-photon-absorption (TPA) process. However, such upconversion process suffers low efficiency and high power threshold in practical use. In stark contrast, lanthanide-doped upconversion materials exhibit a number of outstanding advantages, including a low trigger threshold down to 1 W cm^{-2} and a decent quantum efficiency up to $\sim 4\%$ (Figure 1.2 b). The high efficacy arises from the abundant ladder-like energy levels of lanthanide ions (Figure 1.1), between which resonant energy transfer is very efficient according to energy matching principle. For example, the energy gaps of Tm^{3+} (activator), such as $^3\text{H}_5 \rightarrow ^3\text{H}_6$, $^3\text{F}_2 \rightarrow ^3\text{F}_4$, and $^1\text{G}_4 \rightarrow ^3\text{H}_4$, are highly matching to the energy gap of Yb^{3+} ($^2\text{F}_{5/2} \rightarrow ^2\text{F}_{7/2}$, sensitizer), leading to a strong upconversion luminescence in $\text{NaYF}_4:\text{Yb}/\text{Tm}$ crystals. Another example is the energy migration upconversion (EMU)⁸, in which Gd^{3+} ions are used as migrators to transfer energy from Tm^{3+} to other activators (e.g., Tb^{3+} , Eu^{3+} , Sm^{3+} , Dy^{3+}). This process, again, deeply relies on the ladder-like arrangement of energy levels, since $^1\text{I}_6 \rightarrow ^3\text{H}_6$ (Tm^{3+}) is perfectly matching with $^6\text{P}_{3/2} \rightarrow ^8\text{S}_{7/2}$ (Gd^{3+}).

Apart from the selection of sensitizer/activator or migrator/activator pair, an efficient upconversion process also requires a selection of host matrix in material groups and crystalline phases. Hexagonal-phase NaYF_4 crystal has been established as the most efficient host material for photon upconversion⁹. This host matrix is extensively used as luminescent probe in biological study due to not only its intense luminescence output, but also its excellent chemical stability and biocompatibility. For example, *caenorhabditis elegans* has been used to evaluate the *in vivo* toxicity of $\text{NaYF}_4:\text{Yb}/\text{Er}$ nanoparticles¹⁰. No malformation in the worm's

CHAPTER 1

behavior was found after high dose treatment (5 mg mL^{-1}) for a long period (24 h). Due to these virtues, hexagonal-phase NaLnF_4 were chosen as the objective of study throughout this thesis.

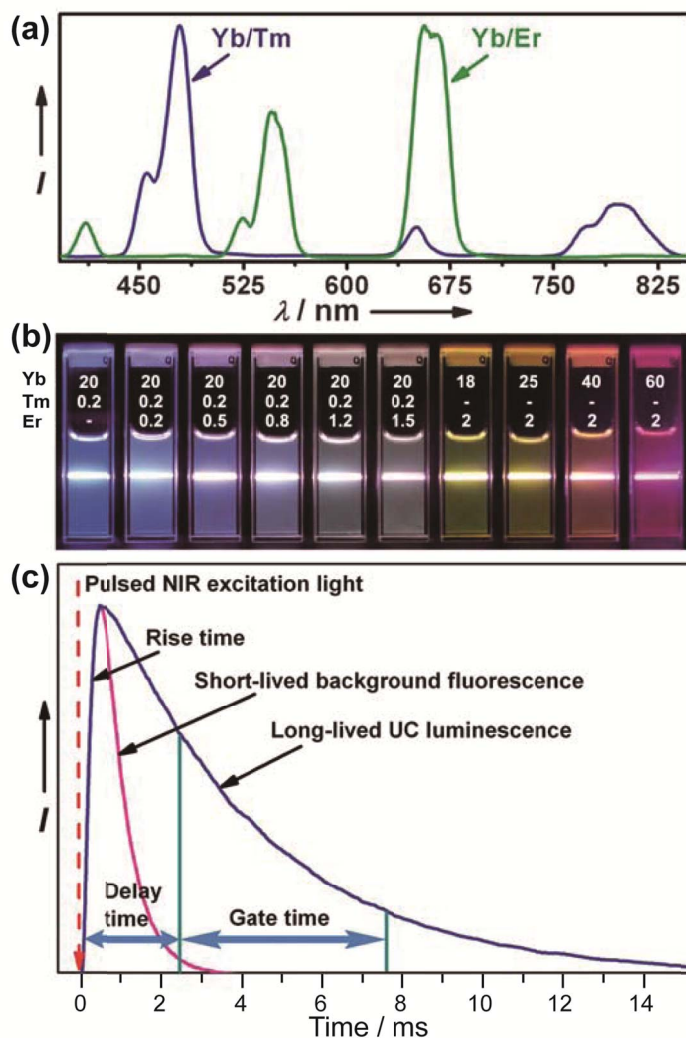


Figure 1.2 Several unique properties of the luminescence from lanthanide-doped materials. (a) Typical upconversion luminescence spectra of Yb/Tm or Yb/Er doped NaYF₄ nanocrystals. (b) Photographs of lanthanide-doped NaYF₄ nanocrystals in aqueous solutions, showing their multicolor emissions upon various doping compositions. Note that the images were taken under a 980-nm laser excitation at a power density of 15 W cm⁻². (c) Typical time-resolved spectra of background fluorescence (pink curve) and upconversion luminescence (blue curve). The long-lived upconversion luminescence enables elimination of background fluorescence through a time-gated imaging technique. **Adapted with permission from Ref. [6]. Copyright 2009, Royal Society of Chemistry.**

1.1.3 Upconversion Bulk-, Micro-, and Nano-crystals

As required by practical use and fundamental study, upconversion crystals, especially NaLnF_4 crystals, have been extensively investigated in the past decades. In the following section, I will provide a brief review on several previously reported findings for growing such crystals in the scale of centimeter, micrometer, and nanometer, respectively. Thereafter, seeded crystal growth will be introduced.

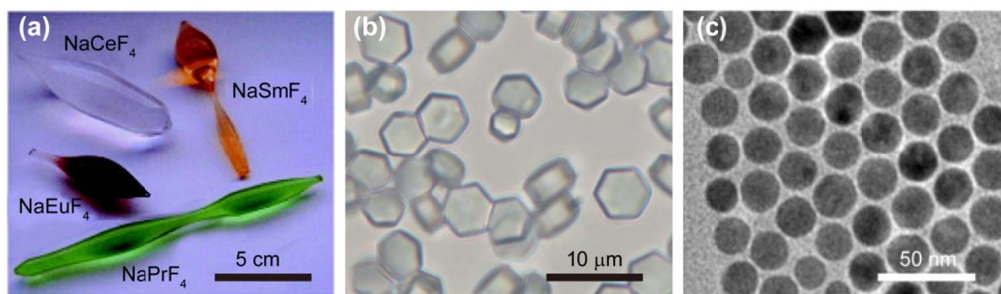


Figure 1.3 Images of single crystals of hexagonal-phase NaLnF_4 with various sizes. (a) Bulk crystals with a feature size of 10 cm. This image was taken using a conventional digital camera. (b) NaLuF_4 microcrystals with a feature size of $5\ \mu\text{m}$. This image was taken under an optical microscope. (c) NaYF_4 nanocrystals with a feature size of 18 nm. This image was taken under an electron transmission microscope. **Adapted with permission from Ref. [12]. Copyright 2005, American Chemical Society.**

Crystallization is a process of forming a crystalline structure from a fluid or from materials dissolved in a fluid. Specific industrial technique to produce bulk NaLnF_4 single crystals (called *boules*, from several centimeters to one meter scale) is a Czochralski crystallization process¹¹, which was developed in 1963 by Thoma *et al.* They systematically investigated the phase equilibria in the system of NaF-YF_3 , and identified eight possible crystal phases. Unfortunately, no information about the crystal quality was presented. In 2005, Lage *et al.* modified the Czochralski method, and successfully synthesized a series of NaLnF_4 single crystals with a good quality and a large size up to several centimeters¹². To obtain NaLnF_4 single crystals, they used NaF-rich melt to depress the melting point of the mixture to a value below the decomposition crystal temperature. This method is analogous to the procedure developed to obtain YF_3 crystals, which also melt incongruently. Nevertheless, they could only obtain single crystals for large Ln ions ranging from La to Gd. The growth of

single crystals of NaLnF_4 with small Ln ions (Tb to Lu) is still a challenging issue.

Due to the need for cell imaging purpose, the synthetic methods for nanometer sized NaLnF_4 have been developed in the past two decades. Krämer *et al.* reported the hexagonal-phase NaYF_4 nanocrystals in 2004 for the first time^{23,24}. The colloidal dispersion exhibits high transparency and stability, suggesting a successful preparation of monodispersed upconversion nanoparticles. Yi *et al.* reported another synthetic approach for size tunable NaYF_4 nanocrystal ranging from 30 nm to 130 nm in the same year¹³. However, the as-prepared nanocrystals adopted a cubic-phase crystalline, which is not an efficient host for maximum luminescence output. Post-treatment, such as annealing at 600 °C, was compulsory to complete the crystalline phase transition from cubic to hexagonal. Unfortunately, aggregation is inevitable after annealing. Yan *et al.* reported a thermal decomposition method¹⁴, providing a versatile synthetic solution for both cubic-phase and hexagonal-phase NaYF_4 nanocrystals in 2006. Liu *et al.* reported a gadolinium doping strategy⁵, realizing the simultaneous control over size and phase of NaYF_4 in 2010. Although these works paved the way for making lanthanide-doped nanoparticles, the crystal-growth mechanism remains unclear.

Single crystals with a size of several micrometers are particularly important for understanding the crystal-growth mechanism, because they are situated in an intermediate stage between nucleation (in nanometer scale) of initial crystallization and bulk crystal (in centimeter scale) of completed crystallization. Li *et al.* synthesized the first lanthanide-doped microcrystal through a hydrothermal procedure¹⁵, but the size of the crystals was not uniform. Lin *et al.* modified this procedure and investigated a series of NaLnF_4 crystals, of which NaYbF_4 crystals were found to be highly uniform in size¹⁶. They attempted to study the morphology evolution with reaction time by quenching reactions at various time intervals. However, the intermediate kinetic products are irregular in morphology, and thus it is questionable to perform statistical analysis on those samples. It is envisioned that the addition of seeding nanocrystals into microcrystal precursor may provide a benchmark for time-dependent evolution of NaLnF_4 crystal-growth process.

1.1.4 Seeded-Crystal Growth

Seeded-crystal growth has been extensively studied in diverse material systems, including Au@Ag core/shell nanocrystals¹⁷, CdSe@ZnS quantum dots¹⁸, and Au/Fe₃O₄ “Janus” material¹⁹. In particular, epitaxy over NaLnF₄ nanocrystals has attracted considerable attention in recent years due to its ability to enhance upconversion efficiency and to construct a core@shell heterogeneous structure. Wang *et al.* observed a 450-fold enhancement in emission intensity after growing a passive NaGdF₄ shell over a 10-nm NaGdF₄:Yb,Tm core²⁰. Zhang *et al.* developed a layer-by-layer strategy that can control the epitaxy thickness in a precision down to 1 nm²¹. Veggel *et al.* reported a self-focus ripening method that takes advantage of a cubic-to-hexagonal phase transition to realize a fine control over epitaxy thickness and epitaxy material species²².

Although much effort has been devoted in this area, several fundamental issues associated with epitaxy are inextricable. For example, the epitaxy thickness is quite limited using current epitaxy techniques (i.e., co-precipitation method), usually less than 5 nm in one trial. To obtain a desired epitaxy thickness, one has to repeat the epitaxy experiment multiple times. It is almost impossible for such a method to generate a microscopic shell beyond optical resolution limit (~ 300 nm), as required by the encoding and decoding processes through the use of optical microscope. Furthermore, a fine control over epitaxy orientation remains a challenging issue. Although it has been well established that surfactants play a pivotal role in crystal morphology control under seedless condition, it is unclear whether the surfactants play a similar role in epitaxy under seeded condition.

1.2 Scope of the Thesis

In this thesis, I would like to present a systematic study on crystal epitaxy in NaLnF₄ material system, aiming to unveil the epitaxy habits pertaining in hydrothermal reactions. The epitaxy products are further used as platforms for investigation of several fundamental issues, such as atomic thermal diffusion and energy transfer between lanthanide ions. The specific objectives of this thesis are listed as follows:

1. To provide solid spectroscopic evidences for large atom diffusion in NaYF_4 crystal lattice through the use of core@shell heterogeneous structures produced by zero-dimensional (0-D) epitaxy technique.
2. To extend the scope of bio-probes and security inks by introducing a multicolor barcode synthesized through one-dimensional (1-D) epitaxy technique.
3. To glean insights into the epitaxy habits pertaining in hydrothermal reactions on the basis of the analysis on two-dimensional (2-D) epitaxy.
4. To achieve subwavelength intracellular imaging by the use of lanthanide-doped nanocrystals as luminescent probes.

Note that the material systems involved in this thesis are mainly hexagonal-phase NaLnF_4 crystals. Other lanthanides compounds, such as lanthanide oxide and sulfide, are beyond the scope of the thesis. The synthetic methods used for material preparation are basically modified hydrothermal procedures. Other synthetic methods, such as solid sintering and thermal decomposition, are not covered in this thesis. The findings in this thesis would make possible for several frontier research topics, such as single-particle bio-probe, microscale upconversion laser, and microscale waveguide.

The detailed content of the thesis will be individually presented in the following chapters. In Chapter 1, lanthanide-doped materials and related crystal-growth techniques will be briefly introduced. In Chapter 2, 0-D epitaxy experiments in NaYF_4 nanocrystal system will be conducted, and the resulted core@shell product will be used for thermal diffusion study. In Chapter 3, 1-D epitaxy in NaYF_4 microrod system will be demonstrated. Related applications of epitaxial microrods, such as anti-counterfeiting and bio-probe, will be covered as well. In Chapter 4, 2-D epitaxy in NaLnF_4 microplate system will be explored, followed by a discussion of epitaxy habits. In Chapter 5, the lanthanide-doped nanocrystals will be used as bio-probes for subwavelength imaging in ion-beam microscopy. Eventually, conclusions and perspectives will be included in Chapter 6.

1.3 References

1. Hänninen P, Härmä H. *Lanthanide luminescence: photophysical, analytical and biological aspects*, vol. 7. Springer Science & Business Media, 2011.
2. Vleck Jv. The puzzle of rare-earth spectra in solids. *J. Phy. Chem.* 1937, **41**(1): 67-80.
3. Huang X, Han S, Huang W, Liu X. Enhancing solar cell efficiency: the search for luminescent materials as spectral converters. *Chem. Soc. Rev.* 2013, **42**(1): 173-201.
4. Auzel F. Upconversion and anti-stokes processes with f and d ions in solids. *Chem. Rev.* 2004, **104**(1): 139-174.
5. Wang F. *et al.* Simultaneous phase and size control of upconversion nanocrystals through lanthanide doping. *Nature* 2010, **463**(7284): 1061-1065.
6. Wang F, Liu X. Recent advances in the chemistry of lanthanide-doped upconversion nanocrystals. *Chem. Soc. Rev.* 2009, **38**(4): 976-989.
7. Idris NM. *et al.* In vivo photodynamic therapy using upconversion nanoparticles as remote-controlled nanotransducers. *Nat. Med.* 2012, **18**(10): 1580-1585.
8. Wang F. *et al.* Tuning upconversion through energy migration in core-shell nanoparticles. *Nat. Mater.* 2011, **10**(12): 968-973.
9. Li Z, Zhang Y. An efficient and user-friendly method for the synthesis of hexagonal-phase NaYF₄: Yb, Er/Tm nanocrystals with controllable shape and upconversion fluorescence. *Nanotechnology* 2008, **19**(34): 345606.
10. Lim SF. *et al.* In vivo and scanning electron microscopy imaging of upconverting nanophosphors in *Caenorhabditis elegans*. *Nano Lett.* 2006, **6**(2): 169-174.
11. Thoma R, Hebert G, Insley H, Weaver C. Phase equilibria in the system sodium fluoride-yttrium fluoride. *Inorg. Chem.* 1963, **2**(5): 1005-1012.
12. Lage MM, Moreira RL, Matinaga FM, Gesland J-Y. Raman and infrared reflectivity determination of phonon modes and crystal structure of Czochralski-grown NaLnF₄ (Ln= La, Ce, Pr, Sm, Eu, and Gd) single crystals. *Chem. Mater.* 2005, **17**(17): 4523-4529.
13. Yi G. *et al.* Synthesis, characterization, and biological application of size-controlled

nanocrystalline NaYF₄: Yb, Er infrared-to-visible up-conversion phosphors. *Nano Lett.* 2004, **4**(11): 2191-2196.

14. Mai H-X. *et al.* High-quality sodium rare-earth fluoride nanocrystals: controlled synthesis and optical properties. *J. Am. Chem. Soc.* 2006, **128**(19): 6426-6436.

15. Wang L. *et al.* Fluorescence resonant energy transfer biosensor based on upconversion-luminescent nanoparticles. *Angew. Chem. Int. Ed.* 2005, **44**(37): 6054-6057.

16. Li C, Quan Z, Yang J, Yang P, Lin J. Highly uniform and monodisperse β -NaYF₄:Ln³⁺ (Ln = Eu, Tb, Yb/Er, and Yb/Tm) hexagonal microprism crystals: hydrothermal synthesis and luminescent properties. *Inorg. Chem.* 2007, **46**(16): 6329-6337.

17. Tsuji M. *et al.* Crystal structures and growth mechanisms of Au@ Ag core-shell nanoparticles prepared by the microwave-polyol method. *Cryst. Growth. Des.* 2006, **6**(8): 1801-1807.

18. Dabbousi B. *et al.* (CdSe) ZnS core-shell quantum dots: synthesis and characterization of a size series of highly luminescent nanocrystallites. *J. Phy. Chem. B* 1997, **101**(46): 9463-9475.

19. Yu H. *et al.* Dumbbell-like bifunctional Au-Fe₃O₄ nanoparticles. *Nano Lett.* 2005, **5**(2): 379-382.

20. Wang F, Wang J, Liu X. Direct evidence of a surface quenching effect on size-dependent luminescence of upconversion nanoparticles. *Angew. Chem.* 2010, **122**(41): 7618-7622.

21. Zhang F. *et al.* Direct imaging the upconversion nanocrystal core/shell structure at the subnanometer level: shell thickness dependence in upconverting optical properties. *Nano Lett.* 2012, **12**(6): 2852-2858.

22. Johnson NJ, Korinek A, Dong C, van Veggel FC. Self-focusing by Ostwald ripening: a strategy for layer-by-layer epitaxial growth on upconverting nanocrystals. *J. Am. Chem. Soc.* 2012, **134**(27): 11068-11071.

23. Krämer KW. *et al.* Hexagonal sodium yttrium fluoride based green and blue emitting upconversion phosphors. *Chem. Mater.* 2004, **16**(7): 1244-1251.

24. Heer S., Kömpe K., Güdel HU., & Haase M. Highly efficient multicolour upconversion emission in transparent colloids of lanthanide-doped NaYF₄ nanocrystals. *Adv. Mater.*, 2004, **16**(23–24): 2102-2105.

2 CHAPTER 2

Spectroscopic Evidence for Lanthanide Ion Diffusion in NaYF₄ Nanocrystals

2.1 Introduction

Diffusion process in crystals plays a critical role in practical applications, such as doping in microelectronic devices¹, solid electrolytes for battery and fuel cells², surface hardening of steel through carburization³, and sintering⁴. Since atomic diffusivity in crystalline is positively correlated to temperature⁵, bulk crystals at high temperature (> 1000 K) were generally used as experimental prototype in previous reports in order to impose a pronounced diffusion effect for the ease of observation. Nanocrystals are a class of materials with size ranging from 1 to 100 nm in at least one dimension. Such small crystals generally have extremely large surface-to-volume ratio when comparing with their bulk counterparts, and therefore, potentially have a large number of surface defects. Theoretically, the diffusion in nanocrystals is very likely to be observed at relatively low temperature because an elevated defect concentration leads to a larger diffusivity. However, experimental demonstrations on this point are scarce.

Sodium lanthanide fluoride (NaLnF_4) nanocrystals provide a prototype that is particularly useful for diffusion study in nanoscale. First, a number of well-established methods have been developed to produce NaLnF_4 nanocrystals of uniform size, versatile morphology, tunable phase, and even core@shell heterogeneous structures⁶, which readily provide a concentration gradient for diffusion study; second, such nanocrystals have been used as efficient host materials for luminescent ion doping⁷, and the diffusion-induced variation on doping concentration can be sensitively reflected on upconversion luminescent spectra. Conventional techniques for diffusion measurement involve tracer diffusion method, impedance spectroscopy, NMR lineshape spectroscopy, and NMR spin-lattice relaxation spectroscopy⁵. However, these techniques require either stringent experimentations or harmful reactants. For example, tracer diffusion method requires the use of radioactive chemicals, such as ^{18}O for the study of oxygen diffusion in ZrO_2 crystal. It is thus very important to develop new user-friendly tools to observe the diffusion behavior in nanoscale. On a separate note, the current diffusion studies are constrained in elements of small atomic size, such as O^{2-} , Li^+ or F^- . It is still challenging to confirm the occurrence of large atom diffusion.

In this chapter, sodium lanthanide fluoride (NaLnF_4) nanocrystals with heterogeneous core@shell architecture were employed as a platform to study the large ions (Tm^{3+} or Er^{3+}) diffusion in crystal lattice. Such core@shell design in structure provides a sharp ion concentration gradient in the core-shell interface, meeting the prerequisite for diffusion to occur. Core@shell nanocrystals were synthesized under a relatively low temperature ($270\text{ }^\circ\text{C}$) through epitaxial growth in a high-boiling point solvent. Diffusion experiment was then conducted under a relatively high temperature ($320\text{ }^\circ\text{C}$) to generate a pronounced diffusion speed. The evolution of upconversion luminescence spectra was used as an indicator to probe the diffusion activity.

2.2 Materials and Methods

2.2.1 Reagents

Yttrium(III) chloride (99.9%), ytterbium(III) chloride (99.9%), thulium(III) chloride (99.9%), erbium(III) chloride (99.9%), sodium hydroxide (NaOH , >98%), ammonium fluoride (NH_4F , >98%), oleic acid (90%), sodium citrate (>99%), and 1-octadecene (ODE, 90%) were all purchased from Sigma-Aldrich and used as received.

2.2.2 Synthesis of $\text{NaYF}_4\text{:Tm}$ (30 mol%) Core Nanocrystals

The $\text{NaYF}_4\text{:Tm}$ (30 mol%) core nanocrystals were synthesized by a co-precipitation method⁸. In a typical experiment, 3 mL of oleic acid and 7 mL of ODE were mixed with 2 mL aqueous solution of YCl_3 ($\text{Y/Tm} = 70/30$ mol%; 0.2 M) in a 50 mL round-bottom flask under vigorous stirring. The resulting mixture was then heated to $150\text{ }^\circ\text{C}$ for 1 h to form a transparent lanthanide oleate complex. After cooling down to room temperature, the complex colloidal was added into a methanol solution (6 mL) containing NH_4F (1.6 mmol) and NaOH (1 mmol), followed by evaporation of methanol at $100\text{ }^\circ\text{C}$ under stirring. The resulted mixture was then heated to $270\text{ }^\circ\text{C}$ and kept at that temperature for 1.5 h under a flow of nitrogen. The nanoparticles were precipitated by addition of ethanol and collected by centrifugation. The pellet was dispersed in 4 mL cyclohexane to form a transparent colloidal for further use.

2.2.3 Synthesis of NaYF₄:Tm@NaYF₄:Yb Nanocrystals

The NaYF₄:Tm (30 mol%)@NaYF₄:Yb (30 mol%) core@shell nanocrystals were synthesized by a similar co-precipitation method as described above. In a typical experiment, 3 mL of oleic acid and 7 mL of ODE were mixed with 2 mL aqueous solution of YCl₃ (Y/Yb = 70/30 mol%; 0.2 M) in a 50 mL round-bottom flask under vigorous stirring. The resulting mixture was then heated to 150 °C for 1 h to form a transparent lanthanide oleate complex. After cooling down to room temperature, the complex colloidal was mixed with 0.4 mmol NaYF₄:Tm (30 mol%) core nanocrystals contained in 4 mL cyclohexane, followed by addition of a methanol solution (6 mL) containing NH₄F (1.6 mmol) and NaOH (1 mmol). The evaporation of methanol and cyclohexane was performed at 100 °C under stirring for 15 min. The resulted mixture was then heated to 270 °C and kept at that temperature for 1.5 h under a flow of nitrogen. The nanoparticles were precipitated by addition of ethanol and collected by centrifugation. The pellet was dispersed in 4 mL cyclohexane to form a transparent colloidal for further use. Note that the NaYF₄:Er (30 mol%)@NaYF₄:Yb (30 mol%) core@shell nanocrystals were synthesized in a similar method as above, except for the composition of the core nanocrystals.

2.2.4 Synthesis of NaYF₄:Tm@NaYF₄@NaYF₄:Yb Nanocrystals

The NaYF₄:Tm (30 mol%)@NaYF₄ core@shell nanocrystals were synthesized following a similar procedure as above, except for the composition of the shell precursor. To coat another shell over these core@shell nanocrystals, 3 mL of oleic acid and 7 mL of ODE were mixed with 2 mL aqueous solution of YCl₃ (Y/Yb = 70/30 mol%; 0.2 M) in a 50 mL round-bottom flask under vigorous stirring. The resulting mixture was then heated to 150 °C for 1 h to form a transparent lanthanide oleate complex. After cooling down to room temperature, the complex colloidal was mixed with 0.4 mmol NaYF₄:Tm (30 mol%)@NaYF₄ core@shell nanocrystals contained in 4 mL cyclohexane, followed by addition of a methanol solution (6 mL) containing NH₄F (1.6 mmol) and NaOH (1 mmol). The evaporation of methanol and cyclohexane was performed at 100 °C under stirring for 15 min. The resulted mixture was then heated to 270 °C and kept at that temperature for 1.5 h under a flow of nitrogen. The

nanoparticles were precipitated by addition of ethanol and collected by centrifugation. The pellet was dispersed in 4 mL cyclohexane to form a transparent colloidal for further use.

2.2.5 Diffusion Experiment for Core@shell Nanocrystals

In a typical experiment, 1 mL cyclohexane dispersion containing 0.1 mmol NaYF₄:Tm (30 mol%)@NaYF₄:Yb (30 mol%) core@shell nanocrystals was mixed with 10 mL ODE in a 50 mL round-bottom flask under vigorous stirring. The resulting mixture was then heated to 100 °C for 15 min to completely evaporate the cyclohexane and further pumped for 15 min to remove residual moistures. The resulted transparent colloidal was subsequently heated up to 320 °C, and maintained at that temperature for 1 hours, during which period the aliquots (0.5 mL per sampling) were retrieved using a glass syringe at 1 min, 10 min, 30 min, and 60 min, respectively.

2.2.6 Physical Measurements

TEM measurements were carried out on a JEOL-JEM 2010F field emission TEM operated at an acceleration voltage of 200 kV. Luminescence spectra were recorded at room temperature with a DM150i monochromator equipped with a R928 photon counting photomultiplier tube and a 980-nm diode laser. Size distribution histograms were graphed based on the size counting of 100 nanocrystals.

2.3 Results and Discussion

2.3.1 Zero-dimensional Epitaxy of NaYF₄ Nanocrystals

To generate a core@shell structure with a large concentration gradient, a two-step method involving co-precipitation and epitaxy was used (Figure 2.1). In the first step, the reaction precursor was elevated to 270 °C and maintained at that temperature for 1.5 hour, affording a type of core NaYF₄:Tm (30 mol%) nanocrystals of uniform size. In the second step, an epitaxy NaYF₄:Yb (30 mol%) precursor was mixed with the core nanocrystals, followed by heating up to 270 °C and maintained at that temperature for 1.5 hour. Such epitaxy method produces a class of NaYF₄:Tm (30 mol%)@NaYF₄:Yb (30 mol%) core@shell nanocrystals of uniform size. Transmission electron microscope images (Figure 2.2) show that the core and core@shell nanocrystals have a feature diameter of 17 nm and 23 nm, respectively. Therefore, the shell thickness is determined to be 3 nm. The size distributions are very narrow, featuring a standard deviation less than 5%.

Since the epitaxial growth of the shell is conducted at high temperature (270 °C) for a substantially long period, atomic diffusion across the core/shell boundary may occur, which may pose uncertainty to the following thermal diffusion experiment. In an attempt to alleviate the diffusion effect induced by the synthesis, a core@shell@shell heterogeneous structure comprising of NaYF₄:Tm (30 mol%)@NaYF₄@NaYF₄:Yb (30 mol%) was prepared. In such a structure, an inert shell of pure NaYF₄ was introduced to isolate the Yb and Tm ions in diffusion during the synthesis. TEM images (Figure 2.3) show that the core, core@shell, and core@shell@shell structures have a feature diameter of 18 nm, 26 nm, and 31 nm, respectively, indicating the thickness of the inert NaYF₄ shell is about 4 nm. The size distributions are very narrow, featuring a standard deviation less than 5%.

2.3.2 Upconversion Luminescence Spectra of Nanocrystals before Diffusion

Upconversion luminescence in lanthanide-doped nanocrystals arises from the efficient energy transfer resulted from the vicinity of sensitizer and activator ions, such as Yb and Tm

ions⁹. When the nanocrystals were singly doped with only one type of lanthanide ions, there would be barely any upconversion luminescence under NIR laser excitation. For example, no upconversion luminescence was observed from NaYF₄:Tm (30 mol%) or NaYF₄:Yb (30 mol%) nanocrystals (Figure 2.4a, and c). Surprisingly, intense upconversion luminescence was observed in NaYF₄:Tm (30 mol%)@NaYF₄:Yb (30 mol%) nanocrystals (Figure 2.4b). This is interesting because the upconversion luminescence is supposed to be very weak since sensitizer ions and activator ions were trapped in core and shell crystal matrices with a substantial distance. Such an abnormal luminescence may arise from the thermal diffusion during the high-temperature synthesis. In an attempt to suppress the unwanted luminescence, a core@shell@shell heterogeneous structure comprising of NaYF₄:Tm (30 mol%)@NaYF₄@NaYF₄:Yb (30 mol%) was prepared. The inert NaYF₄ was designed to act as a block layer to isolate Tm and Yb ions during synthesis. However, the strong upconversion luminescence arising from these crystals (Figure 2.4d) proves that there are still a number of Yb/Tm ion pairs that can accomplish energy transfer upconversion process. Such Yb/Tm ion pairs may exist in the inert NaYF₄ shell, where they can diffuse from their original matrix layers. These experiments verify that it is impossible to eliminate the diffusion effect caused in synthetic procedures even if using inert-shell design. Therefore, NaYF₄:Tm (30 mol%)@NaYF₄:Yb (30 mol%) nanocrystals will be used as platform to investigate the spectral evolution behavior during thermal diffusion process.

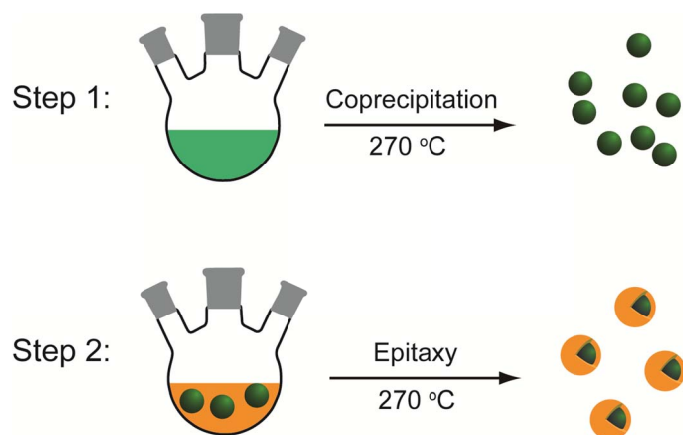


Figure 2.1 Schematic showing the two-step synthetic method. In step 1, the NaYF₄:Tm (30 mol%) core nanocrystals were synthesized at 270 °C; in step 2, these core nanocrystals were used as seeds to over coat an epitaxial shell comprising NaYF₄:Yb (30 mol%).

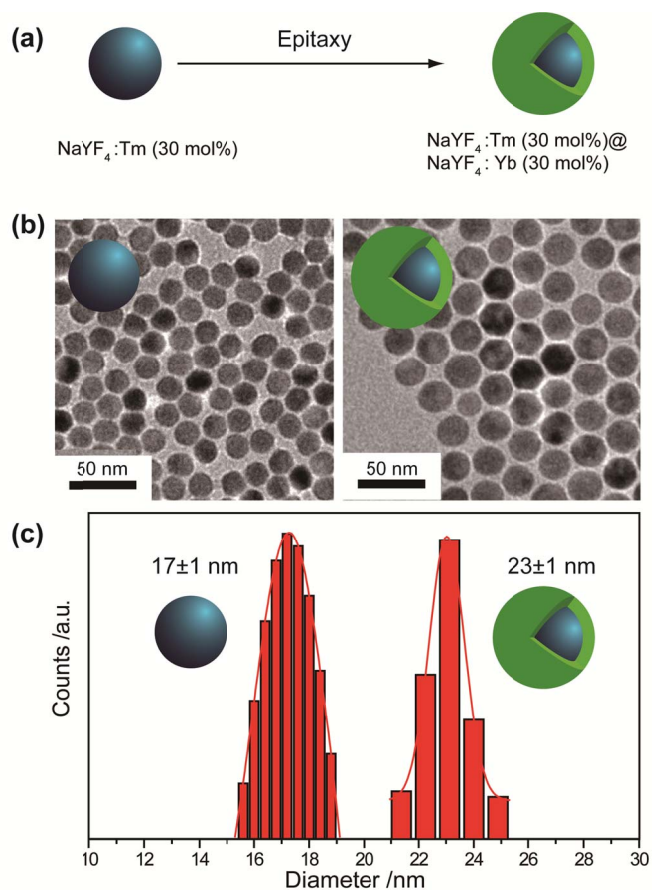


Figure 2.2 (a) Schematic showing the synthesis of a core@shell heterogeneous structure with a composition of $\text{NaYF}_4:\text{Tm}$ (30 mol%)@ $\text{NaYF}_4:\text{Yb}$ (30 mol%). (b) Typical TEM images of the core and core@shell nanocrystals, showing a uniform morphology of these particles. (c) Size distribution histogram of core and core@shell nanoparticles, revealing the epitaxy shell with a feature thickness of 3 nm.

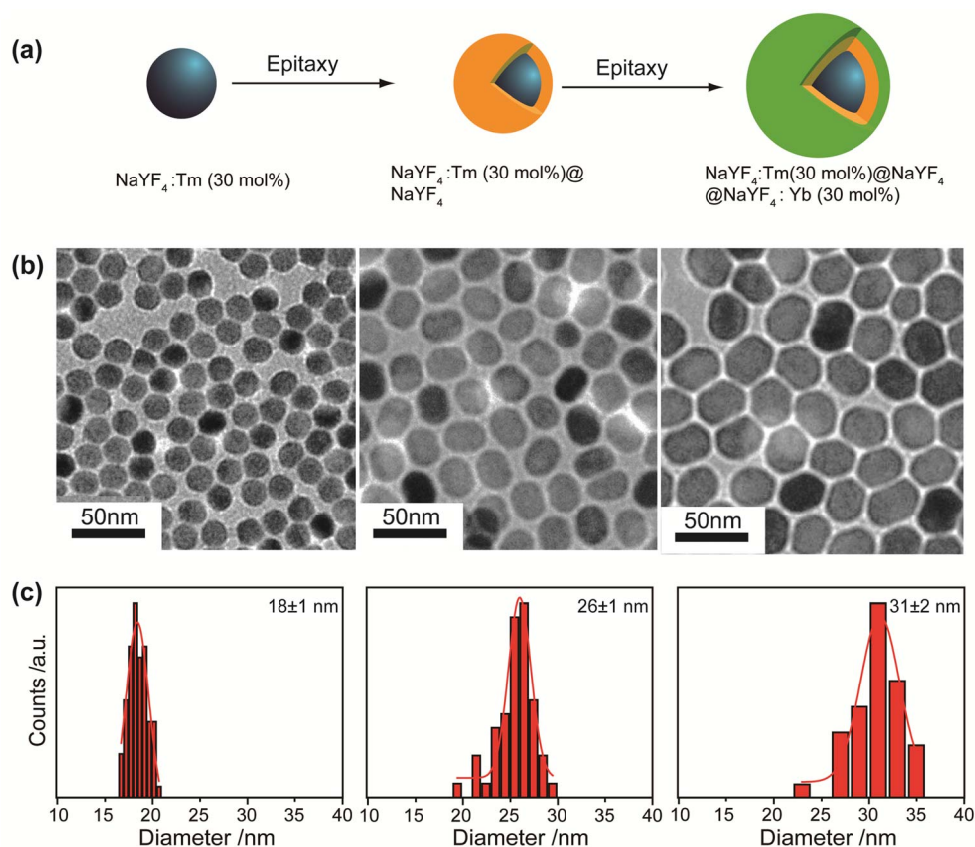


Figure 2.3 (a) Schematic showing the synthesis of a $\text{NaYF}_4:\text{Tm}$ (30 mol%)@ NaYF_4 @ $\text{NaYF}_4:\text{Yb}$ (30 mol%) core@shell@shell heterogeneous structure. Note that the first inert NaYF_4 shell was used as a buffer layer to alleviate the atomic diffusion during the synthesis. (b) Typical TEM images of the core, core@shell, and core@shell@shell nanocrystals, showing a uniform morphology of these particles. (c) Size distribution histograms of these nanoparticles, revealing the first epitaxy shell with a feature thickness of 4 nm, and second epitaxy shell of 2.5 nm in thickness.

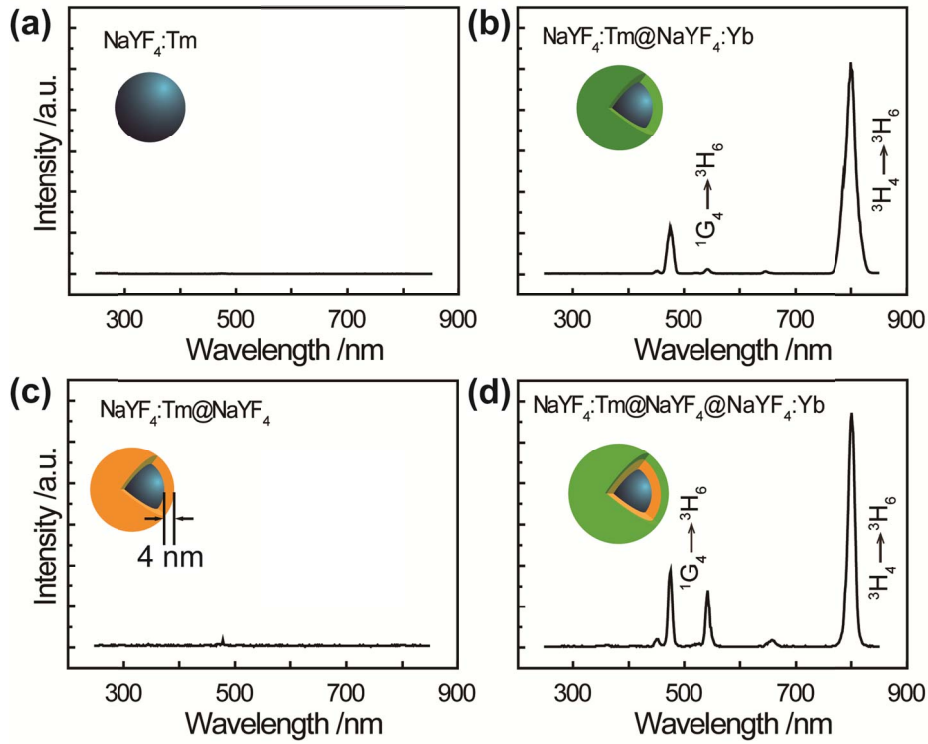


Figure 2.4 Room temperature upconversion spectra of as-synthesized nanocrystals under an excitation of 980-nm laser at a power density of 15 W cm^{-2} . The composition of these nanocrystals are (a) $\text{NaYF}_4:\text{Tm}$ (30 mol%), (b) $\text{NaYF}_4:\text{Tm}$ (30 mol%)@ $\text{NaYF}_4:\text{Yb}$ (30 mol%), (c) $\text{NaYF}_4:\text{Tm}$ (30 mol%)@ NaYF_4 , and (d) $\text{NaYF}_4:\text{Tm}$ (30 mol%)@ $\text{NaYF}_4@ \text{NaYF}_4:\text{Yb}$ (30 mol%), respectively.

2.3.3 Upconversion Luminescence Spectra of Nanocrystals after Diffusion

To prove the existence of atomic diffusion by upconversion spectral evolution, several stringent conditions should be considered in the design of experimentation. First, the concentrations of upconversion nanoparticles for each measurement should be kept constant; second, the solvent used for annealing purpose should be of high boiling point up to 320 °C and high thermal stability; third, the solvent should be benign in chemistry, so that the nanoparticles are not harmed even under high temperature. To meet these requirements, a solution-based annealing system was designed for thermal diffusion experiments (Figure 2.5). 1-octadecene (ODE) was chosen as the solvent because of its high boiling point and thermal stability. Besides, its transparency allows an accurate spectral measurement without emission loss. In a typical diffusion experiment (Figure 2.5), the NaYF₄:Tm (30 mol%)@NaYF₄:Yb core@shell nanocrystals were heated up to 320 °C in the 1-octadecene solvent under argon atmosphere. Aliquots were retrieved at various time intervals, followed by upconversion spectral measurements at room temperature.

As shown in Figure 2.6a, the upconversion spectra of the NaYF₄:Tm (30 mol%)@NaYF₄:Yb core@shell nanocrystals present two characteristic emission peaks of Tm ions at 475 nm and 800 nm, arising from the intra-configuration 4f-4f electronic transitions ¹G₄ → ³H₆ and ³H₄ → ³H₆, respectively. As annealing time increases, the luminescent intensity increases to the maximum in the first 10 min, and then decreases down to zero in 60 min. It is well known that the upconversion emission intensity of Tm is sensitive to its concentration in the Yb-doped crystal matrix, usually exhibiting an inverse parabolic profile in intensity-concentration graph. A similar inverse parabolic profile was found in the intensity-diffusion time graph (Figure 2.6b). Such similarity strongly indicates a positive correlation between Tm concentration and diffusion time. The concentration of Tm ions in the shell layer would increase with increasing diffusion time according to the Fick's law⁵,

$$J = -D \frac{dC}{dx}$$

where, J is the flux of Tm atoms, atoms/(m²s), the number of atoms which pass through a unit area in a unit of time; D is the diffusivity or diffusion coefficient, m²/s; dC/dx is the

concentration gradient, atoms/m⁴.

The diffusion-induced emission evolution can be explained based on foregoing analysis. In the first 10 min, the flux of Tm ions diffused into shell layer and formed an emissive layer by pairing with Yb ions; in the period between 10-30 min, the emissive layer expanded as diffusion time increased, therefore the emission intensity is relatively high in this period; in the last 30 min, the concentration of Tm ions went beyond a critical concentration, leading to severe concentration quenching effect. As a result, the emission intensity decreased down to zero.

Remarkably, the concentration gradient of Yb and Tm in the core@shell heterogeneous structure plays an important role in the diffusion process. To shed more light on this point, a type of homogeneous nanocrystals, NaYF₄:Yb/Tm (18/0.5 mol%) nanocrystals, was prepared in a control experiment. As expected, the emission intensity of such nanocrystals is essentially unaltered in the diffusion experiment (Figure 2.6c-d).

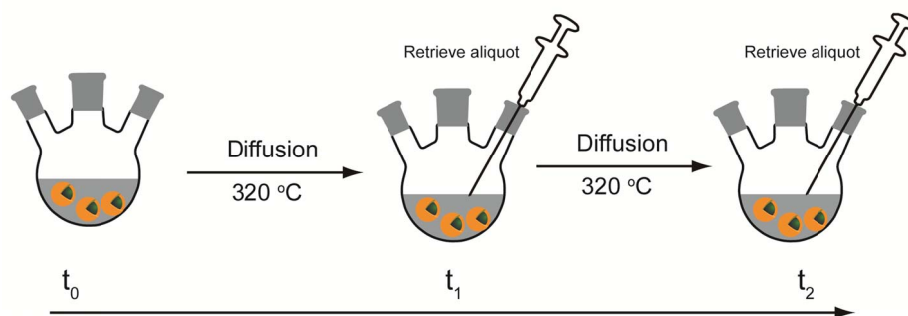


Figure 2.5 Schematic showing the diffusion experimentation. The core@shell nanocrystals were dispersed in ODE, a high-boiling point solvent that allows the diffusion process to occur at 320 °C for certain time. Aliquots were retrieved for real-time spectral measurement.

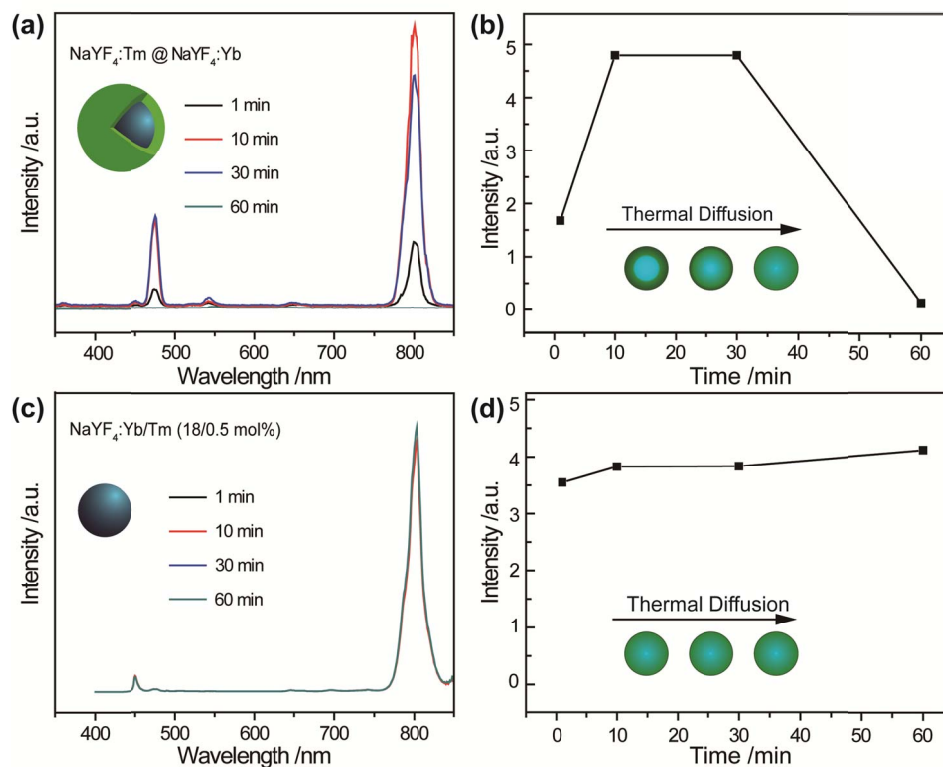


Figure 2.6 (a) Room temperature upconversion spectra of $\text{NaYF}_4:\text{Tm}$ (30 mol%)@ $\text{NaYF}_4:\text{Yb}$ (30 mol%) heterogeneous nanocrystals retrieved from thermal diffusion reaction system at various time intervals. (b) The integrated intensity of upconversion luminescence of heterogeneous nanocrystals evolves against diffusion time. (c) Room temperature upconversion spectra of $\text{NaYF}_4:\text{Yb/Tm}$ (18/0.5 mol%) homogeneous nanocrystals retrieved from thermal diffusion reaction system at various time intervals. (d) The integrated intensity of upconversion luminescence of homogeneous nanocrystals evolves against diffusion time.

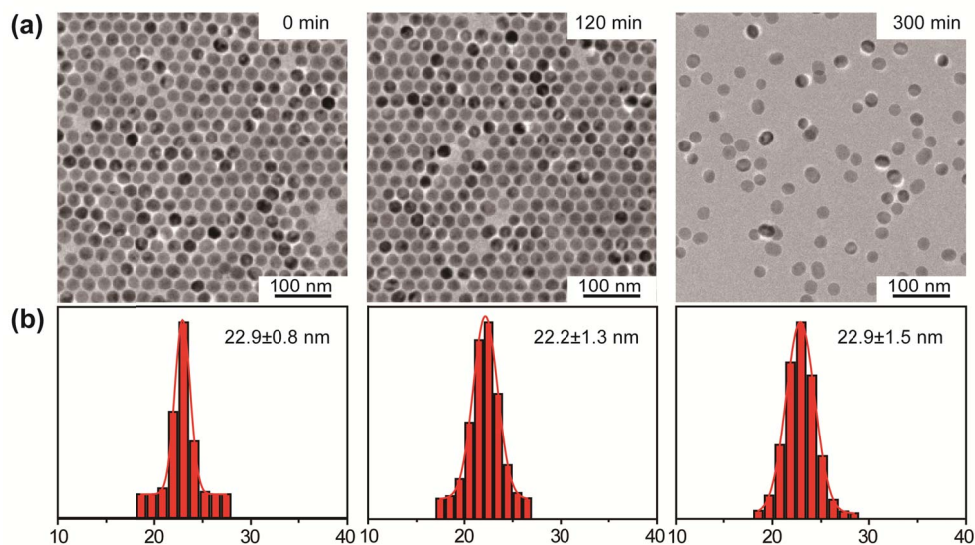


Figure 2.7 A control experiment shows that the morphology of NaYF₄:Tm (30 mol%)@NaYF₄:Yb (30 mol%) core@shell nanocrystals is maintained during thermal diffusion process. (a) TEM images of particles retrieved from the reaction system of 320 °C at varied time intervals. Note that the self-assembly of particles (0 min and 120 min) is mainly caused by the oleic acids tethered on particle surfaces. After long-term treatment (300 min) in octadecene, the oleic acids are partially replaced by octadecene, leading to a disassembly pattern in TEM image. (b) Size distribution histograms of the retrieved particles showing essentially unaltered sizes.

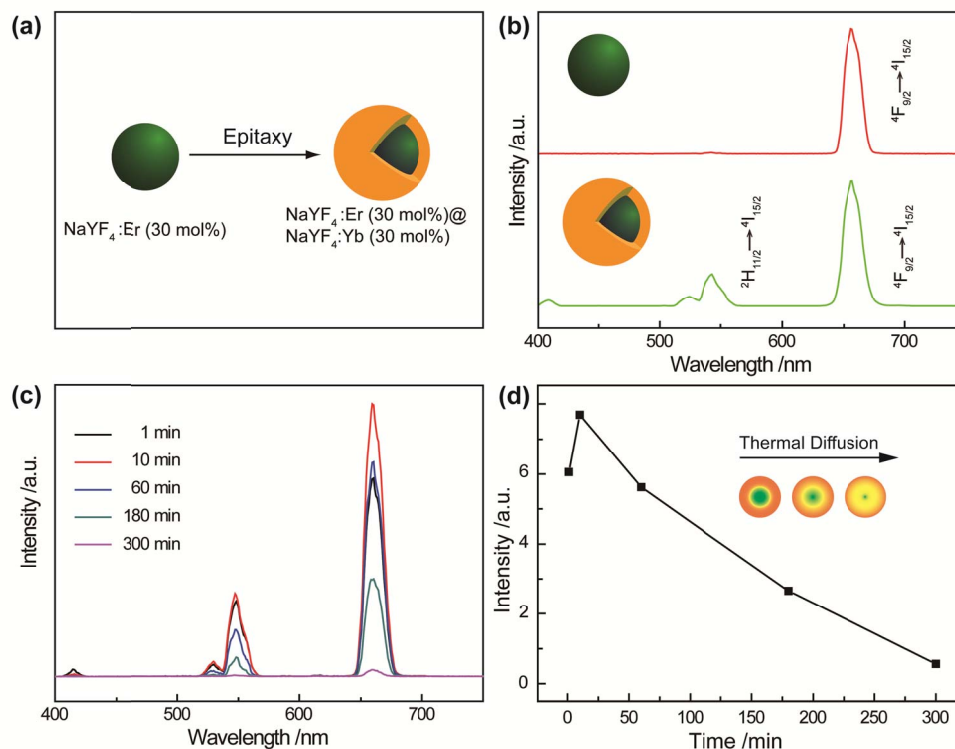


Figure 2.8 A control experiment showing the diffusion of Er ions in crystal lattice. **(a)** Synthetic scheme showing the zero-dimensional epitaxy of $\text{NaYF}_4:\text{Er}$ (30 mol%) nanocrystals. **(b)** Room temperature upconversion spectra of core (red line) and core@shell (green line) nanocrystals under an excitation of 980-nm laser at a power density of 15 W cm^{-2} . It should be noted that the emergence of green emission peak after epitaxy suggests the existence of partial diffusion during 2-hour synthetic process at $270 \text{ }^\circ\text{C}$. **(c)** The evolution of upconversion spectra against thermal diffusion time at 1 min, 10 min, 60 min, 180 min, and 300 min. Note that the diffusion experiment was conducted at $320 \text{ }^\circ\text{C}$, much higher than synthesis temperature. **(d)** The evolution of integrated emission intensity of core@shell nanoparticles against diffusion time.

2.3.4 Ostwald Ripening

It has been reported that the particle size is positively correlated to the emission intensity due to the surface quenching effect. In order to rule out the possibility of size change induced by Ostwald ripening during diffusion experiment at high temperature¹⁰, TEM measurements were conducted to track the size distributions of NaYF₄:Tm (30 mol%>@NaYF₄:Yb (30 mol%) nanocrystals. The TEM data suggest essentially unaltered size distribution of those particles retrieved from various time intervals in the diffusion experiment. Interestingly, the particles did not undergo an Ostwald ripening process even at a temperature up to 320 °C. This is attributable to the weak etching ability of ODE. To validate this point, a mixture of ODE and oleic acid was used as annealing solvent in another control experiment. The nanoparticles were found to be completely dissolved after diffusion experiment (data not shown). It can be explained by the strong etching ability of oleic acid.

To expand the scope of lanthanide ions in the study of diffusion, NaYF₄:Er (30 mol%>@NaYF₄:Yb (30 mol%) nanocrystals were prepared. The thermal diffusion experiment of Er ions displays a similar inverse parabolic profile to that of Tm ions in spectral evolution graph (Figure 2.8), suggesting a general diffusion behavior of the lanthanide ions in fluoride crystal lattice.

2.4 Conclusion

In conclusion, lanthanide-doped nanocrystals with a core@shell structure were used as a platform for thermal diffusion study of large ions, such as Tm and Er. The diffusion behavior of these ions was confirmed by the upconversion spectral evolution. The upconversion luminescent intensity exhibits an inverse parabolic profile against diffusion time, which is rationalized by the Fick's law. Several control experiments were performed to rule out those uncertain factors, such as Ostwald ripening. The methodology involved in this chapter provides a paradigm for large atom diffusion study on nanocrystal level.

2.5 References

1. Lu N. *et al.* Ge diffusion in Ge metal oxide semiconductor with chemical vapor deposition HfO₂ dielectric. *Appl. Phys. Lett.* 2005, **87**(5): 1922.
2. Smith K, Wang C-Y. Solid-state diffusion limitations on pulse operation of a lithium ion cell for hybrid electric vehicles. *J. Power Sources* 2006, **161**(1): 628-639.
3. Tarakci M, Korkmaz K, Gencer Y, Usta M. Plasma electrolytic surface carburizing and hardening of pure iron. *Surf. Coat. Tech.* 2005, **199**(2): 205-212.
4. Chamberlain AL, Fahrenholtz WG, Hilmas GE. Pressureless sintering of zirconium diboride. *J. Am. Ceram. Soc.* 2006, **89**(2): 450-456.
5. Heitjans P, Kärger J. Diffusion in condensed matter: methods, materials, models. Springer Science & Business Media, 2006.
6. Yang D, Hou Z, Cheng Z, Li C, Lin J. Current advances in lanthanide ion (Ln³⁺)-based upconversion nanomaterials for drug delivery. *Chem. Soc. Rev.* 2015, **44**(6): 1416-1448.
7. Boyer J-C, Vetrone F, Cuccia LA, Capobianco JA. Synthesis of colloidal upconverting NaYF₄ nanocrystals doped with Er³⁺, Yb³⁺ and Tm³⁺, Yb³⁺ via thermal decomposition of lanthanide trifluoroacetate precursors. *J. Am. Chem. Soc.* 2006, **128**(23): 7444-7445.
8. Li Z, Zhang Y, Jiang S. Multicolor core/shell structured upconversion fluorescent nanoparticles. *Adv. Mater.* 2008, **20**(24): 4765-4769.
9. Gargas DJ. *et al.* Engineering bright sub-10-nm upconverting nanocrystals for single-molecule imaging. *Nat. Nanotechnol.* 2014, **9**(4): 300-305.
10. Johnson NJ, Korinek A, Dong C, van Veggel FC. Self-focusing by Ostwald ripening: a strategy for layer-by-layer epitaxial growth on upconverting nanocrystals. *J. Am. Chem. Soc.* 2012, **134**(27): 11068-11071.

3 CHAPTER 3

Epitaxy in One-dimensional Upconversion Crystals: Multicolor Barcoding on a Single Particle

3.1 Introduction

Barcoding materials have been widely used as luminescent probes for multiplexed assays in biological species because of their distinct optical characteristics^{1,2}. The use of these materials for anti-counterfeiting applications has also attracted much attention in recent years^{3,4}. However, their application in practical settings has been largely hindered by high-cost materials fabrication, low reaction yields, complex instrumentation set-up, and high background noise when excited by common ultraviolet or visible light sources.

Lanthanide-doped upconversion materials may provide a much needed solution for the above-mentioned problems⁵. First, their fabrication methods are typically based on low-cost bottom-up processes, and can be easily scaled up for massive production^{6, 7}. Second, the morphology of the upconversion materials is highly tunable with features ranging from nano-sized particles to microscale rods⁸, allowing for direct decoding without the concern of the diffraction limit using conventional optical microscopes. The third aspect is that upconversion materials feature large anti-Stokes shifts and long lifetimes, leading to largely reduced background noise^{9,10}. Furthermore, the ability to tune the emission wavelength from UV–Vis to NIR spectral regions offered by photon upconversion enables the generation of a large, diverse library of optical barcodes^{11, 12}. Despite their promise, it has been challenging to prepare multicolored upconversion barcodes using a single spherical nanoparticle due to the resolution limit of conventional optical microscopes.

This chapter presents the rational design and synthesis of multicolor-banded upconversion barcodes based on tip-modified hexagonal-phase NaYF₄ microrods with different activators doped at the tips. With varying sets of activators, I prepare a library of single-crystal-based upconversion barcodes comprising different combinations of three primary colors (red, green, and blue) that are easily readable with conventional optical microscopes. This chapter also demonstrates the use of these optical materials as barcodes for security inking and cell tracking applications.

3.2 Materials and Methods

3.2.1 Reagents

Yttrium(III) nitrate (99.9%), ytterbium(III) nitrate (99.9%), thulium(III) nitrate (99.9%), erbium(III) nitrate (99.9%), sodium hydroxide (NaOH, >98%), ammonium fluoride (NH₄F, >98%), oleic acid (90%), dimethyl sulfoxide (DMSO) were all purchased from Sigma-Aldrich and used as received.

3.2.2 Synthesis of β -NaYF₄ Microrod

The β -NaYF₄ microrods were synthesized by a slightly modified literature procedure via hydrothermal reaction^{13,14}. In a typical experiment, NaOH (0.3 g; 7.5 mmol) was first dissolved in 1.5 mL of DI water, followed by addition of 5 mL of oleic acid and 5 mL of ethanol under vigorous stirring. Thereafter, an aqueous solution of NH₄F (2 M; 1 mL) was added to form a turbid mixture. Subsequently, a 2-mL aqueous solution of Y(NO₃)₃ (Yb³⁺/Tm³⁺ = 20/0.2 mol%; 0.2 M) was added and the solution was kept stirring for 20 min. The resulting mixture was then transferred into a 20-mL Teflon-lined autoclave and heated to 220 °C for 12 h. After cooling down to room temperature, the reaction product was isolated by centrifugation and washed with ethanol. The as-synthesized microrods showed a blue color emission upon excitation at 980 nm. For other emission colors, the doping concentrations of Yb³⁺ and Er³⁺ were adjusted accordingly (Green: Yb³⁺/Er³⁺: 5/0.05 mol%; red: Yb³⁺/Er³⁺: 50/0.05 mol%; yellow: Yb³⁺/Er³⁺: 20/2 mol%). To the synthesis of β -NaYF₄ microrods with different lengths, Y(NO₃)₃ was added in combination with Gd(NO₃)₃ (Y³⁺/Gd³⁺: 70/30 mol% for 0.5- μ m microrods and Y³⁺/Gd³⁺: 55/45 mol% for 0.3- μ m microrods), and the temperature was kept at 200 °C for 3 h.

3.2.3 Synthesis of α -NaYF₄ Nanoparticle

The α -NaYF₄ nanoparticles were synthesized by the same reaction procedure as their hexagonal-phase counterparts, except for the heating temperature and reaction time. The reaction mixture was kept at 180 °C for 3 h instead of 220 °C for 12 h. After cooling down to room temperature, the reaction product was used without further purification as the precursor

for successive epitaxial tip-growth of the β -NaYF₄ microrods.

3.2.4 Synthesis of β -NaYF₄ Microrods with Dual-Color Emissions

Typically, 4 mL of β -NaYF₄ microrods and 1 mL of α -NaYF₄ nanoparticles were mixed under vigorous stirring. The resulting mixture was then transferred into a sealed 10-mL Teflon-lined autoclave and heated at 220 °C for 12 h, at which time the reaction was allowed to cool down to room temperature. The reaction product was obtained by centrifugation and washed three times by ethanol.

3.2.5 Physical Measurements

TEM measurements were carried out on a JEOL-JEM 2010F field emission TEM operated at an acceleration voltage of 200 kV. Elemental mapping was carried out with JED-2300T EDX (energy dispersive x-ray spectrometer) system at 200 kV on a JEOL JEM-2100 LaB₆ TEM. XRD data were collected on a Bruker D8 Advance diffractometer using graphite-monochromatized CuK α radiation ($\lambda = 1.5406 \text{ \AA}$). Luminescence spectra were recorded at room temperature with a DM150i monochromator equipped with a R928 photon counting photomultiplier tube and a 980-nm diode laser. Upconversion luminescence imaging was performed using an upright Olympus BX51 microscope coupled with a 980-nm diode laser through fibre output. Luminescence micrographs were recorded with a Nikon DS-Ri1 imaging system. Digital photographs of security patterns were taken under 980-nm laser excitation by a Nikon D700 camera.

3.2.6 Luminescence Lifetime Measurement of a Single Microrod

The lifetime measurement was performed on a home-built upconversion laser scanning confocal microscope as illustrated in Figure 3.1. The illumination from a single mode fibre-coupled diode laser (350 mW, 975 nm, LEO Photonics Co., Ltd) was collimated by a commercial collimator (F240FC-780, NA = 0.5, Thorlabs) and focused onto a sample slide by an objective lens (60 \times , 0.9 NA, Olympus) via a dichroic mirror (BLP-980R-25, Semrock). The sample slide was placed on a programmed 3-Axis NanoMax Stage (MAX311D/M). The fluorescent signal was collected by the same objective lens and then projected onto a color

CCD camera (2.11 MP, Ds-Vi1, Nikon) after reflected by the dichroic mirror and a flip mirror 1. This step of wide-field fluorescence imaging was applied to roughly position the targets randomly distributed on the sample slide. The confocal microscopy resolution was further achieved by moving the flip mirror 1 out of the optical path. The fluorescence signal was then coupled by a convex lens ($f = 200$ mm) into a 50- μm core diameter optical fibre and detected by an avalanched photodiode (APD) (SPCM-AQRH-14-FC, PerkinElmer Optoelectronics). To support real-time data acquisition and analysis at high speed, one 16-channel analog-to-digital data acquisition (DAQ) card (1.25 MHz bandwidth per channel; PXIe-6358, National Instruments) was connected to a computer. This stage-scanning confocal microscope allows for locating the specific position of a single microrod target on the slide. To accurately measure the lifetime of a specific spot (confocal image pixel) on the microrod, the complete confocal imaging of the microrod was firstly scanned and captured. Subsequently, the tip junction was identified using a green filter (FF01-545/55-25, Semrock). For experiments described in this work, the confocal imaging data were retrieved and analyzed selectively on three typical specific areas (labelled as spot 1, 2, 3 as shown in Figure 3.12) near the tip-junction of the microrod. A series of band-pass filters were used to measure their luminescence lifetimes at the specific emission band. The effective decay time²⁵ τ_{eff} is calculated by

$$\tau_{\text{eff}} = \frac{1}{I_0} \int_0^{\infty} I(t) dt$$

where $I(t)$ denotes the luminescence intensity as a function of time t and I_0 represents the maximum intensity.

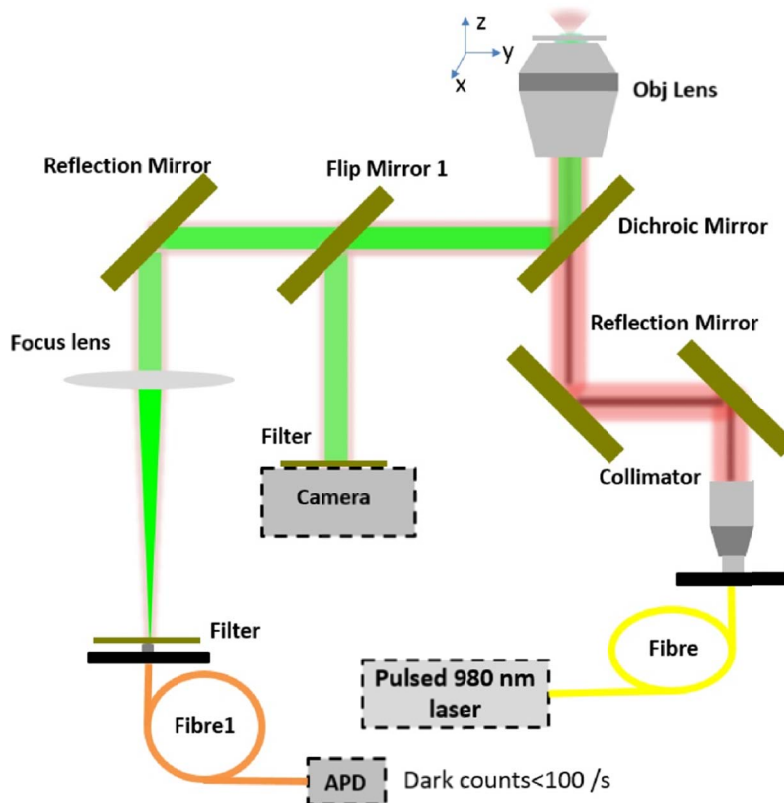


Figure 3.1 Simplified layout of a home-made upconversion characterization system. The system incorporates three basic functions: wide-field microscopy imaging, laser scanning confocal imaging, and lifetime measurement system. This wide-field imaging is used to pinpoint the locations of interest from a large area. The scanning confocal imaging is then used to zoom in and scan the detailed area of a single microrod, and therefore the sensitive lifetime measurement can be achieved to characterize the emitting features at high spatial resolution.

3.2.7 Preparation of Microrod-based Ink for Security Printing

Dimethyl sulfoxide (DMSO) was used to disperse the as-synthesized upconversion microrods for security printing application. In a typical experiment, a cyclohexane solution of upconversion microrods (1 mL; 0.02 M) was first centrifuged at 5000 rpm to precipitate the microrods. The isolated microrods were then mixed with 1 mL of ethanol and 1 mL of HCl aqueous solution (2 M). The resultant mixture was sonicated for 5 min to remove the ligand thoroughly, followed by centrifugation at 5000 rpm. The microrods were then alternatively washed by ethanol and water for 3 times. The ligand-free microrods were re-dispersed in DI/DMSO (v:v; 1:4) to make the security ink. It was found that single-color NaYF₄ microrods (Yb³⁺/Er³⁺: 10/0.05 mol%) show an identical spectrum to tips-modified microrods (Yb³⁺/Er³⁺: 5/0.05 mol% for middle part, and Yb³⁺/Er³⁺: 50/0.05 mol% for the tips). To make a “NUS” pattern onto A4 paper or glass slide, a rubber stamp with an inverse “NUS” pattern was dipped into this ink. Then the stamp was taken out and pressed against the substrate to transfer the pattern onto these substrates.

3.2.8 Cell Coding and Tracking

HeLa cells were seeded in a 35-mm dish and incubated in Dulbecco’s modified eagle medium (DMEM) overnight (37 °C, 5% CO₂). Ligand-free green-emitting upconversion microrods (0.1 mL; 100 µg/mL) in DI water were then added and the mixture was incubated for 6 h. Thereafter, the cancer cells were washed with PBS buffer for 3 times prior to upconversion imaging. The real-time video tracking can be used to confirm the uptake of the microrods into the cells. As shown in Movie S1 (ref 15), the microrods engulfed inside a cell are clearly immobilized without any discernable movement, while the ones coated on the external surface of the cell membrane constantly move as a result of Brownian motion¹⁵. To further confirm that the microrods were indeed internalized in cells, transmission electron microscopy imaging of HeLa cell was performed. Typically, the labeled cells were fixed with Karnovsky’s Fixative (2% paraformaldehyde and 2.5% glutaraldehyde in PBS) for 2 h. Subsequently, they were further fixed in OsO₄ solution (1%) for 1.5 h, followed by dehydration in alcohol and propylene oxide. The resulted cells were embedded in Spurr’s

CHAPTER 3

Resin, and sectioned into slices (~ 100 nm in thickness) with an ultramicrotome. The slices were mounted on the TEM grids and imaged under a JEOL-JEM 2010F field emission TEM.

3.3 Results and Discussion

3.3.1 Resolution of Optical Microscope

Regular light microscopes generally have the best spatial resolution of ~ 200 nm constrained by the optical diffraction limit^{16,17}. To resolve two emission features (or spots), the two emitting objects need to be separated by a distance larger than the diffraction limit. Otherwise, the microscope would not have the necessary resolution power to distinguish them. In my design, NaYF₄ microrods with a length of ~ 2 μm were used as spacer to grow tip-modified rods that can exhibit distinguishable dual-color emissions.

To confirm this, three types of microrods with emitting tips separated by spacers of different lengths were prepared (Figure 3.2). It was found that as the length of the spacer increases from 0.3 μm to 1.7 μm , the two emitting spots are gradually resolved from one merged spot into two independent spots. Meanwhile, it was observed that the reaction yield in the growth of tip-modified microrods decreased when using Gd³⁺-doped microrods as templates. This is ascribed to the lattice expansion in Gd³⁺-doped microrods due to large ionic size of Gd³⁺ relative to Y³⁺, leading to lattice mismatch between the parent rods and the tip precursors. Considering the compromise of synthetic yield induced by Gd³⁺ doping, 1.7- μm spacer was chosen in this work for multicolor tuning on a single upconversion crystal. The use of the 1.7- μm spacer for the growth of tip-modified rods overcomes the diffraction limit, allowing different emission colors easily resolvable at the single crystal level.

3.3.2 Epitaxy Design and Characterization

The lanthanide-doped NaYF₄ multicolor microrods were prepared by a well-established hydrothermal method¹⁸. Such a method was chosen for its flexibility to produce both cubic and hexagonal phase NaYF₄ crystals under almost identical experimental conditions, except for the reaction temperature. In a typical synthesis, the α -NaYF₄:Yb/Er (50/0.05 mol%) nanoparticles and the β -NaYF₄:Yb/Er (50/0.5 mol%) nanorods were first synthesized at 180 °C and 220 °C, respectively.

Figure 3.3a shows the X-ray diffraction pattern of the as-prepared α -NaYF₄:Yb/Er (50/0.05 mol%) nanoparticles, revealing the cubic-phase nature of the particles. It is worth noting that the diffraction peaks are largely broadened when compared to those bulk cubic crystals, suggesting that the samples have a small grain size falling in the nanometer scale¹⁹. Such conjecture was further confirmed by the TEM measurement as shown in Figure 3.3b. These cubic nanoparticles have a feature size around 10 nm, and a feature shape of nanocube, which is in agreement with previous report⁸.

Figure 3.4a and b represent a typical SEM image and a TEM image of the β -NaYF₄:Yb/Er (5/0.5 mol%) nanorods, respectively. These as-prepared nanocrystals are highly uniform in morphology, with a feature length of 1.9 μ m and a feature diameter of 200 nm. X-ray diffraction pattern (Figure 3.4c) evidenced that the nanorods adapt a pure hexagonal-phase in crystallography. These one-dimensional nanocrystals exhibit strong upconversion luminescence under 980-nm laser excitation. Remarkably, the luminescence color can be tuned, over a very broad range covering from 300 nm to 800 nm, through a lanthanide-doping strategy. For example, the three primary colors, red, green, and blue (RGB), can be readily obtained by doping lanthanide-ion-pairs of Yb/Er (50/0.05 mol%), Yb/Er (5/0.05 mol%), and Yb/Tm (30/0.2 mol%), respectively. The corresponding spectra and micrographs of these RGB nanorods were presented in Figure 3.5 a-f. Note that the apparent color of these upconversion nanorods stems from the admixture of the multiple emission bands. A copious color library can be afforded by tuning the relative intensity of those bands, promising a large number of distinct barcodes to be generated by such lanthanide-doping method.

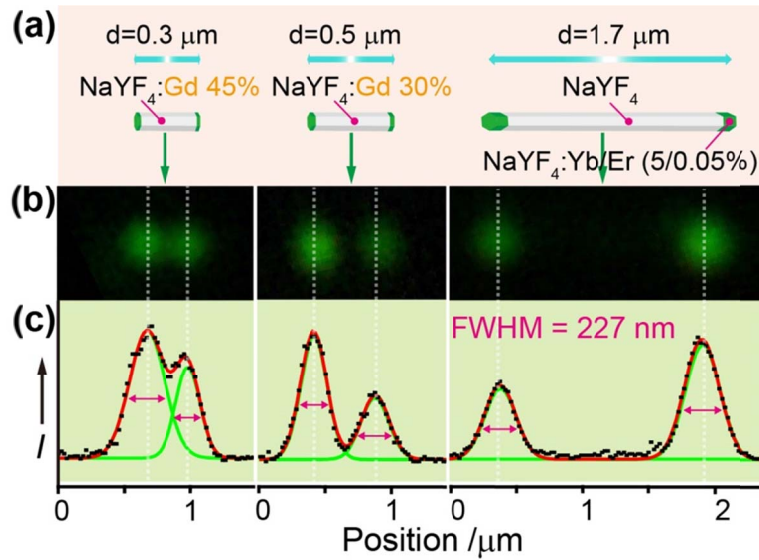


Figure 3.2 (a) Schematic design for determining the diffraction limit of the microscope using three tip-modified microrods with different spacer lengths (0.3, 0.5, and 1.7 μm). (b) Upconversion micrographs of the three microrods showing the emission dots from the tips. (c) Their corresponding emission spectra indicating the degree of the spatial overlap between the two emission dots. The point spread function (red line) of the intensity profile is fitted with Gaussian function (green line), and the full width at half maximum (FWHM) is taken as the resolution. The average FWHM of the six spots is 227 nm, in good agreement with the theoretical value (196 nm at 550 nm estimated using an oil objective lens with a numeric aperture of 1.4). Note that the length of the spacer is tuned by Gd doping at varied concentrations.

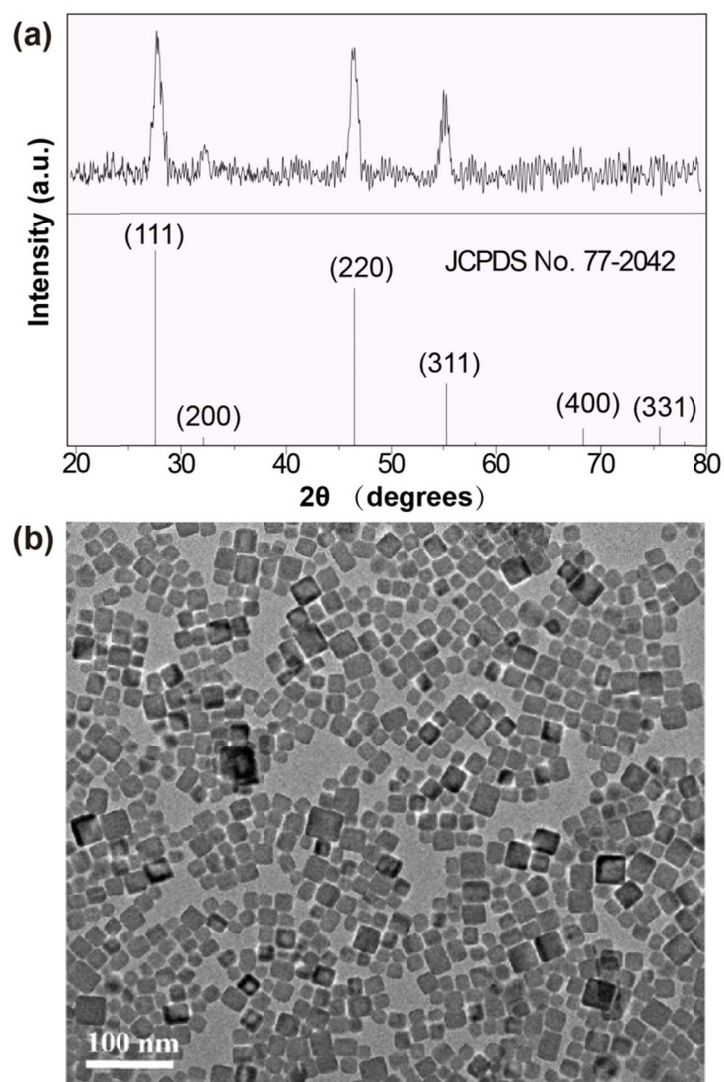


Figure 3.3 (a) XRD characterization of the as-synthesized cubic-phase NaYF_4 :Yb/Er (50/0.05 mol%) nanoparticles used as the precursor for tip-modification of the microrods. (b) The corresponding TEM image of the cubic-phase NaYF_4 nanoparticles.

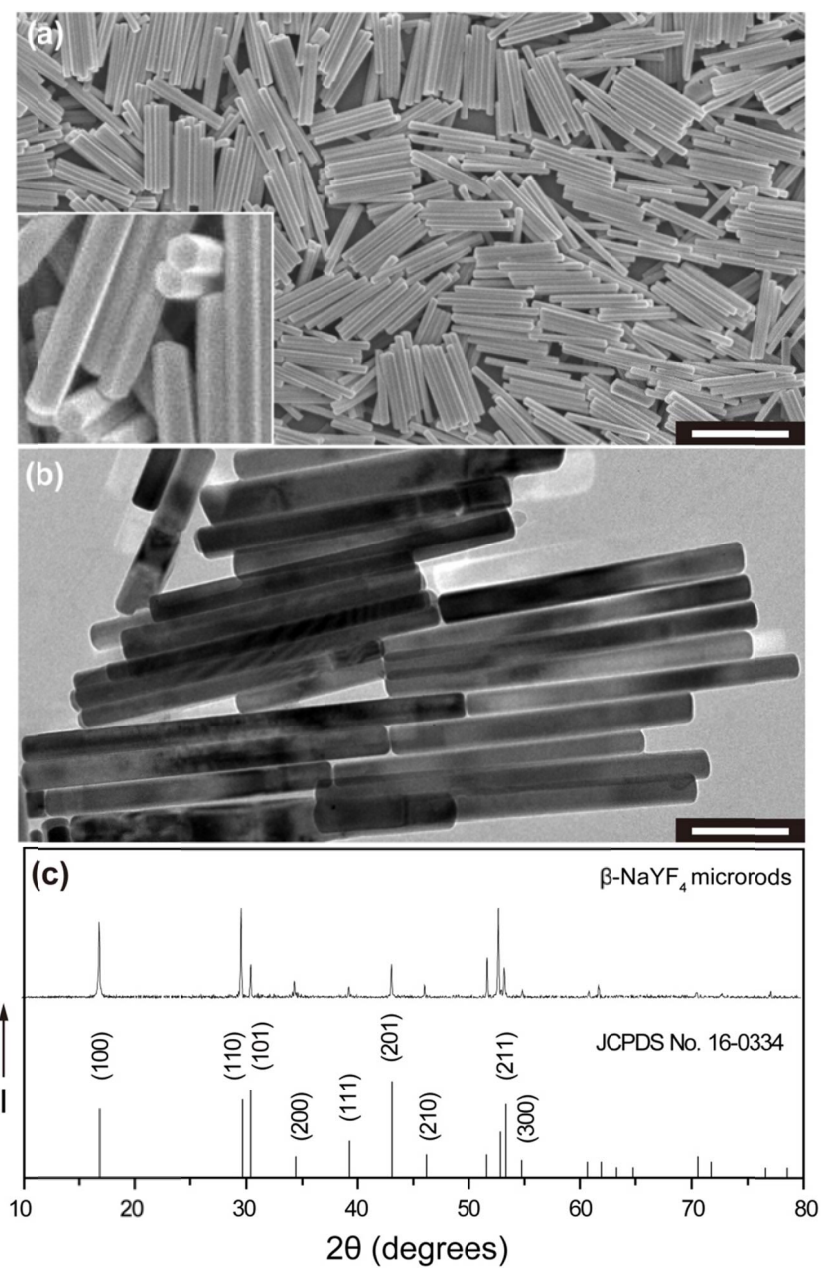


Figure 3.4 (a) A typical SEM image and TEM image (b) of the hexagonal-phase NaYF₄:Yb/Er (5/0.05 mol%) nanorods, showing the high uniformity of the samples. Inset in (a) shows the hexagon-like cross-section of the nanorods. Scale bar represents 2 μm in (a) and 0.5 μm in (b), respectively. (c) XRD pattern of the hexagonal-phase NaYF₄:Yb/Er (5/0.05 mol%) nanorods.

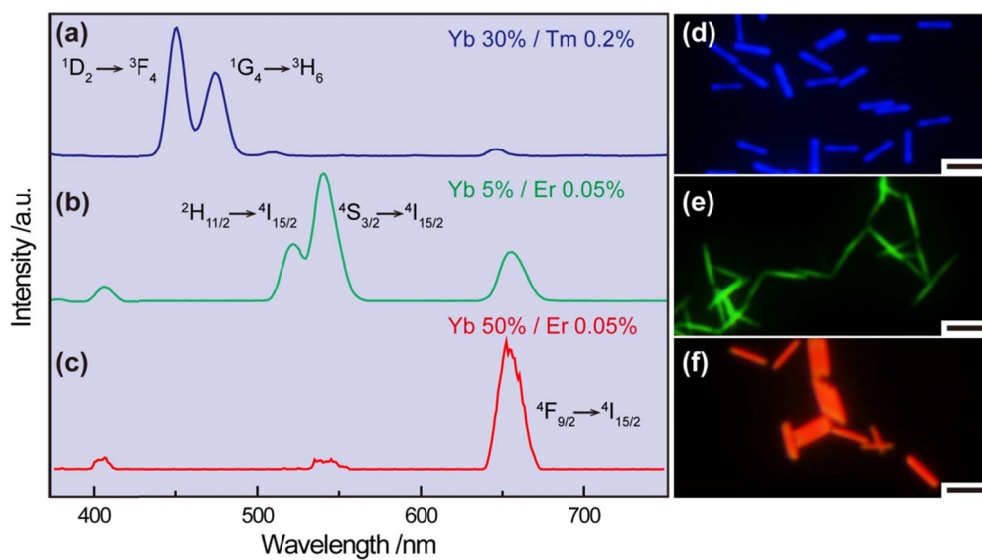


Figure 3.5 (a-c) Room-temperature upconversion emission spectra of hexagonal-phase NaYF_4 microrods with different Yb/Er/Tm doping compositions. The samples were excited at 980 nm with a 2 W diode laser. **(d-f)** The upconversion luminescence micrographs of blue, green, and red NaYF_4 nanorods. Scale bars are 2 μm .

3.3.3 General Considerations on Epitaxy

In order to generate a dual-color-banded barcode with high yield, several considerations should be taken into account. First, the epitaxy on spacer (i.e., NaYF₄ nanorod) should be highly oriented along [001] axis. Fortunately, the hydrothermal condition producing NaYF₄ nanorods genetically fulfills such requirement²⁰. Second, epitaxy precursor should be carefully chosen. Cubic-phase nanoparticles may be used as precursor due to their low thermal stability^{21,22}. Several reports have proven the phase transition from cubic to hexagonal at elevated temperature. Importantly, Veggel's group found a "self-focus" crystal-growth process when cubic and hexagonal phase NaYF₄ nanoparticles were brought to high temperature in admixture²³. Such finding is inspiring since it not only allows the cubic nanoparticles to serve as epitaxy precursor, but also verifies the seeding privilege of hexagonal phase nanoparticles over their cubic phase counterparts. Based on these considerations, I designed a synthetic route as shown in Figure 3.6.

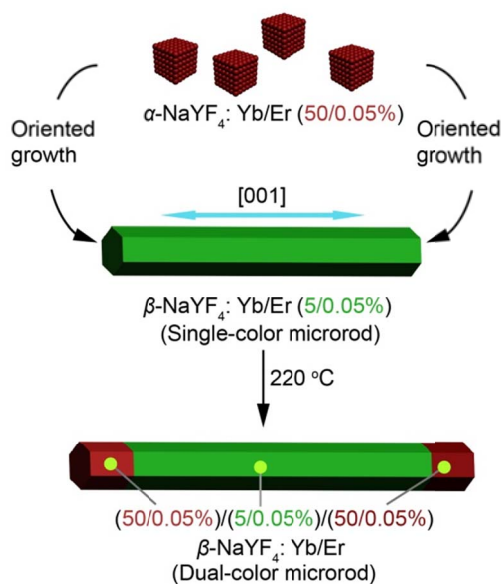


Figure 3.6 Design of the bottom-up synthesis of a dual-color-banded hexagonal-phase NaYF₄:Yb/Er upconversion microrod through an oriented epitaxial growth method. As cubic-phase NaYF₄ nanoparticles tend to dissolve at elevated temperatures due to low thermal stability, they could be used as precursors for successive growth of hexagonal-phase NaYF₄ tips at both ends of the microrods.

3.3.4 Characterization of Dual-Color-Banded Barcodes

Upon addition of α -NaYF₄ nanoparticles as the precursors, successive end-on growth of the β -NaYF₄ microrods can be achieved, as evidenced by the optical microscopic images (Figure 3.7a). This is attributable to favorable epitaxial growth along the long [001] axis of the crystal. Note that the red-emitting tips are heavily doped with 50 mol% of Yb³⁺, while the green-emitting segment is doped with 5 mol% of Yb³⁺. As a result of the heavy atomic nature of Yb, the transmission electron microscopic image shows two dark-colored tips of the segmented rods (Figure 3.7b). High-resolution TEM reveals single-crystalline nature of the rod with a *d*-spacing of 0.30 nm as shown in Figure 3.7b inset, corresponding to (110) plane of β -NaYF₄ (JCPDS No. 16-0334). Elemental scanning over the junction further shows the composition difference between the parent rod and the epitaxial tips (Figure 3.7c). To further gain a quantitative understanding of the composition, spot scan on specific areas was performed (Figure 3.8). Such measurement shows that the Yb concentration in epitaxial tips is 39.5 mol%, a very similar value to that of α -NaYF₄:Yb/Er (50/0.05 mol%) nanoparticle precursors. Such similarity in composition strongly indicates that the crystallization of the epitaxial tip is at the expense of the cubic-phase precursor. In an attempt to broaden the scope of barcoding library, several types of dual-color-banded barcodes were synthesized through a step-by-step method by using primary colors (RGB) as coding units (Figure 3.7d-h).

To confirm the tip growth onto the parent microrod, elemental mapping by STEM was performed on the resulting hybrid rods. The difference in the elemental distribution of Yb³⁺ and Y³⁺ over the rod tip clearly indicates the presence of a junction (Figure 3.9a and b). The HRTEM and corresponding Fourier-transform diffractogram (Figure 3.9c and d) of the junction clearly reveal the single crystalline nature of the epitaxy junction, manifesting the ability to multiplexing colors at single-crystal level.

3.3.5 Epitaxial Growth Monitoring

As mentioned previously, the phase transition of NaYF₄ crystals from cubic phase to hexagonal phase plays an important role in the epitaxial growth. However, it was only observed at reaction systems of high temperature (300 °C)²³. In order to verify the occurrence

of phase-transition under hydrothermal condition (220 °C), XRD measurement on samples before and after hydrothermal treatment was conducted (Figure 3.10). Upon mixing hexagonal-phase nanorods and cubic-phase precursor, the reaction system before hydrothermal treatment exhibits a mixed XRD pattern comprising both characteristic peaks of cubic-phase and hexagonal-phase NaYF₄ crystals. After long-term reaction at 220 °C, the characteristic peaks of cubic phase completely vanished, providing a hard evidence for the occurrence of phase transition. Accompanied with the phase transition, an enhancement on 665-nm emission band was also observed, which is in agreement with the emergence of two red-emitting tips on a green nanorod (Figure 3.7a).

Notably, the use of α -NaYF₄ nanoparticle precursor rather than a lanthanide ionic solution is critical for high yield synthesis of the segmented nanorods (Figure 3.11b). It is found that the direct use of ionic precursors leads to unseeded growth, forming a mixture of two phases including seeding crystals and precursor crystals (Figure 3.11a). This is partially due to the initial ion concentration is larger than the critical nucleation concentration, which encourage the self-nucleation of ionic epitaxy precursor. In stark contrast, the α -NaYF₄ nanoparticle precursor provides a nucleation environment of very low ionic concentration (nearly zero at the beginning) since those ions are tightly trapped in cubic-phase matrix before heating up to 220 °C. The cubic-phase crystal matrix releases lanthanide ions as the temperature increases due to its low thermal stability, and concurrently, the recrystallization over seeding β -NaYF₄ nanorods consumes the released ions. These two processes reach a chemical balance before the α -NaYF₄ nanoparticle precursor is completely depleted.

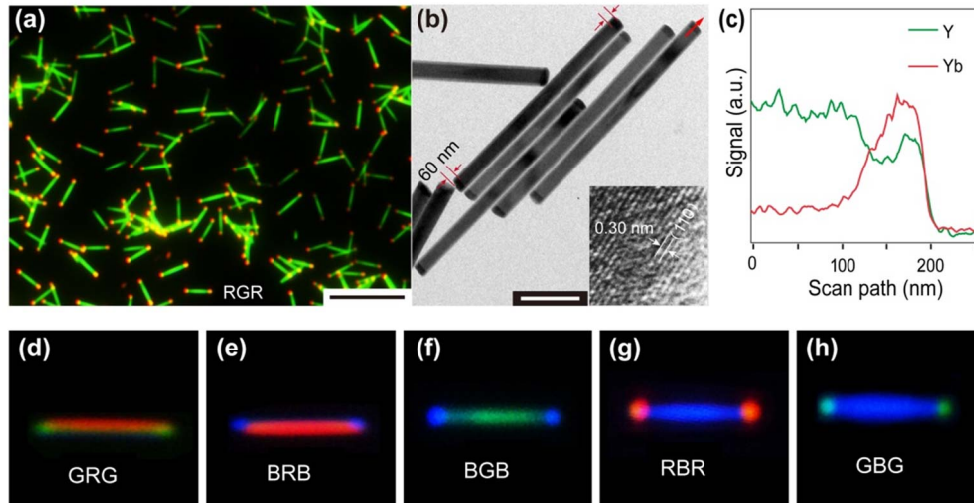


Figure 3.7 (a) Optical micrographs of dual-color (RGR) emitting NaYF_4 microrods after the end-on epitaxial growth over $\text{NaYF}_4:\text{Yb}/\text{Er}$ (5/0.05 mol%, green) nanorods with cubic-phase $\text{NaYF}_4:\text{Yb}/\text{Er}$ (50/0.05 mol%, red) precursors. Scale bar is 5 μm . (b) TEM image of the tip-modified microrods (Inset: HRTEM image). Scale bar is 500 nm. (c) Elemental distribution profile by EELS line scan conducted along the red arrow in (b). (d-h) Upconversion luminescence micrographs of five additional dual-color-banded microrods, obtained by varying the composition of the dopants. Note that two colors are mixed at the junction due to the chromatic aberration and limited resolution of the microscope.

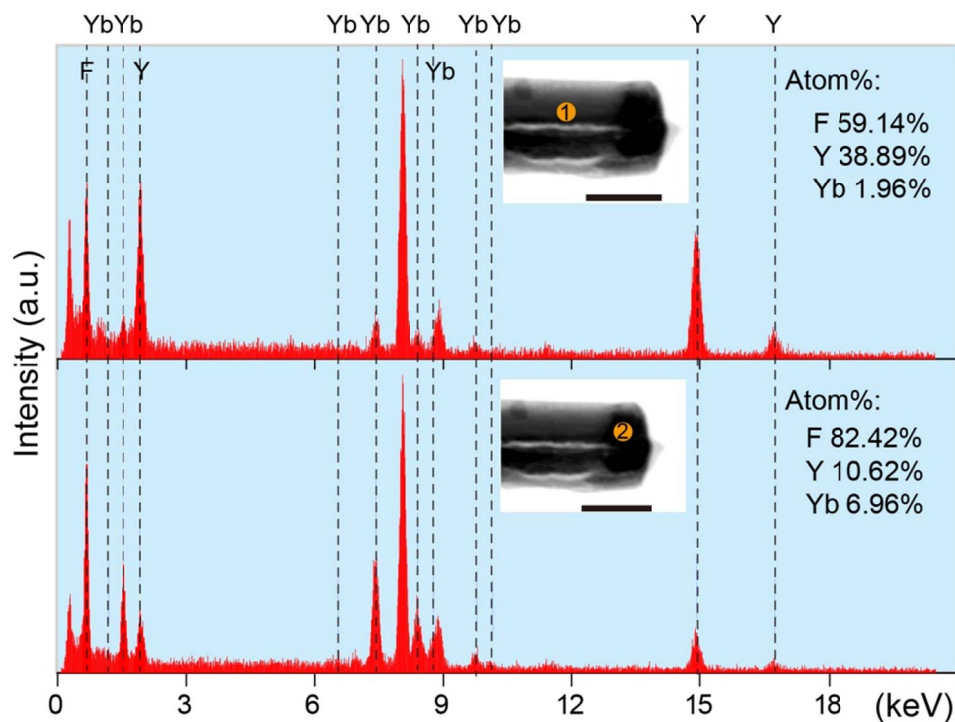


Figure 3.8 Spot scan analysis of an individual dual-color-emitting NaYF_4 microrod ($\text{Yb}^{3+}/\text{Er}^{3+}$:5/0.05 mol% for the parent rod, and $\text{Yb}^{3+}/\text{Er}^{3+}$:50/0.05 mol% for the tips). Characteristic peaks of elemental Y, Yb, and F are indicated in dashed line. The elemental abundances at the position 1 of the parent rod and the position 2 of the tip are also listed. The doping concentration is calculated as Yb in spot 1: $1.96/(1.96+38.89) = 4.8$ mol%, and in spot 2: $6.96/(6.96+10.62) = 39.5$ mol%. Scale bars are 100 nm.

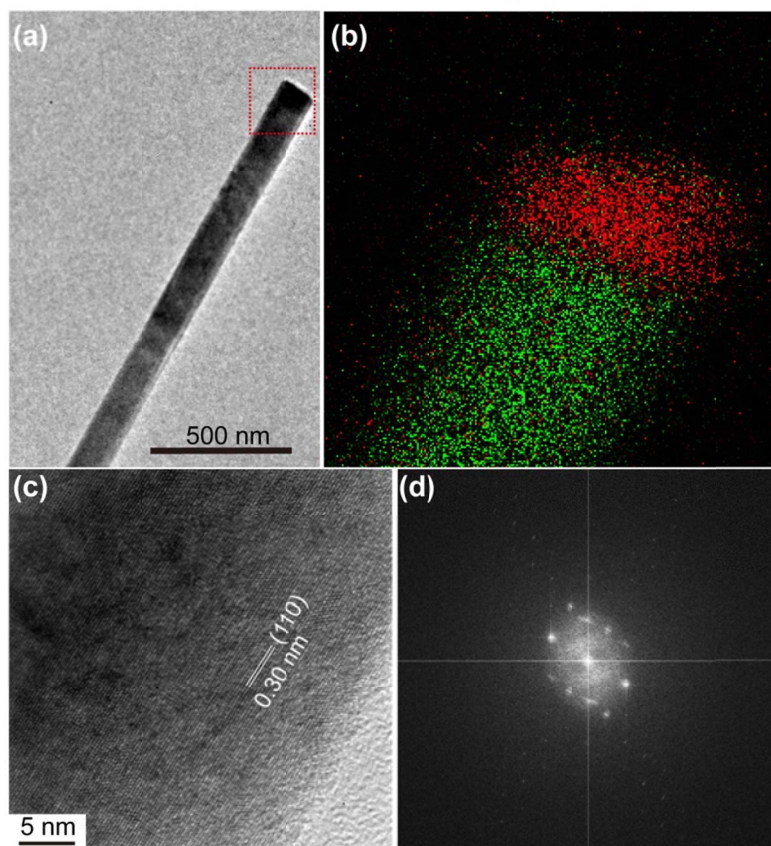


Figure 3.9 (a) A typical TEM image showing the epitaxial junction of a single NaYF₄ microrod. The red dashed box shows the junction site. (b) Elemental mapping of Yb (red) and Y (green) distribution over an epitaxy junction (red dashed box in a) by energy dispersive spectrometer technique. (c) High resolution TEM image of the junction area corresponding to the position of the box marked in a. (d) Corresponding Fourier-transform diffractogram of the junction. The dot pattern reveals the single crystalline nature of the junction.

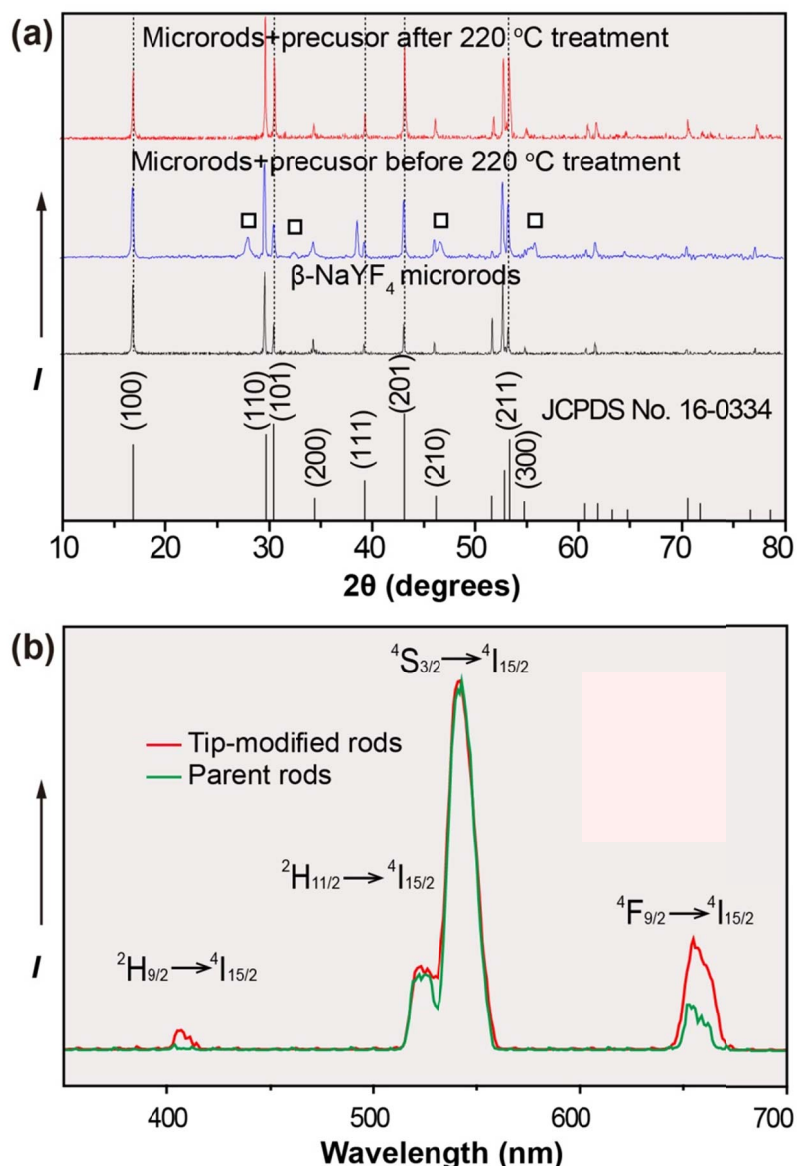


Figure 3.10 (a) XRD characterizations of the tip-modified NaYF_4 ($\text{Yb}^{3+}/\text{Er}^{3+}$:5/0.05 mol% for parent rods, and $\text{Yb}^{3+}/\text{Er}^{3+}$:50/0.05 mol% for the tips) microrods prepared by a hydrothermal reaction at 220 °C in the presence of cubic-phase NaYF_4 nanoparticles and parent hexagonal-phase NaYF_4 microrods. Diffraction peaks corresponding to cubic-phase NaYF_4 are marked with square boxes. (b) Room temperature upconversion emission spectra of the parent rods (green line) and the tip-modified microrods (red line). The two spectra were normalized at 545 nm peak. The microrods modified with NaYF_4 : $\text{Yb}^{3+}/\text{Er}^{3+}$ (50/0.05 mol%) tips showed an emission peak at 655 nm with intensity higher than that of the parent rods. The samples were excited at 980 nm with a 2W diode laser.

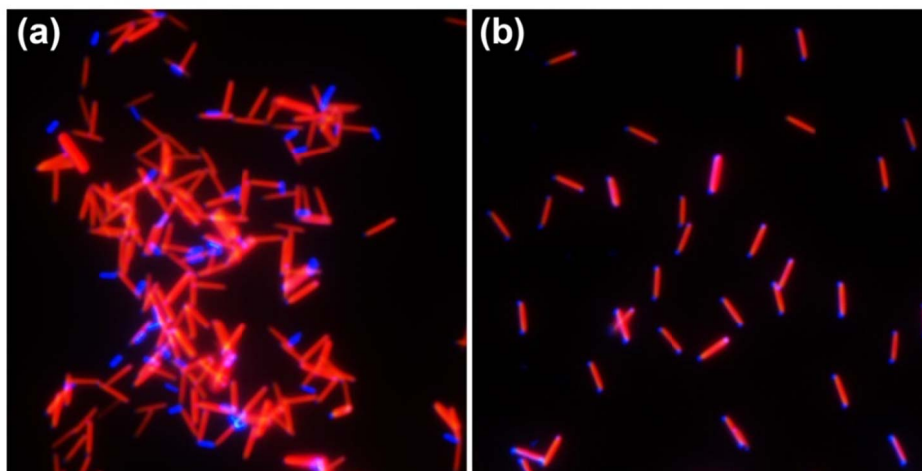


Figure 3.11 Upconversion micrographs of the as-synthesized dual-color-emitting microrods prepared through the use of (a) lanthanide ionic solutions (lanthanide nitrates and NH_4F ; Y:Yb:Tm:F = 0.798:0.2:0.002:5 mol%) or (b) cubic-phase NaYF_4 :Yb/Tm (20/0.2 mol%) nanoparticles. The comparison of the two images clearly indicates the high yield of the end-on tip-epitaxial growth in (b). The low yield in the growth of tip-modified microrods in (a) is likely due to phase separation.

3.3.6 Energy Transfer at the Junction

As an added benefit, the dual-color upconversion nanorod provides a platform to investigate the possibility of energy transfer at the tip junction. To this end, I synthesized YBY-color rods (Y and B denote yellow emission of the tips and blue emission of the parent rod, respectively) following a similar procedure shown in Figure 3.6. In order to gain a pronounced energy transfer effect, a relatively high concentration of Er (2 mol%) is adapted in the tip segment. Figure 3.12a shows a typical upconversion luminescence micrograph of a single nanorod.

Using a confocal microscope, three different spots (Labeled as 1, 2, 3) at the region of the tip junction can be selectively focused and scanned (Figure 3.12b). Notably, the use of different band-pass filters allows us to analyze the individual emission peak of Er^{3+} , for example, green emission at 545 nm ($^4\text{S}_{3/2} \rightarrow ^4\text{I}_{15/2}$) and red peak at 655 nm ($^4\text{F}_{9/2} \rightarrow ^4\text{I}_{15/2}$) (Figure 3.13). Essentially unaltered lifetimes of Er^{3+} recorded at three different spots (Figure 3.12c) were observed, indicating that there is no crosstalk between Tm^{3+} and Er^{3+} activators even at the tip junction. It is reasoned that the intrinsic small absorption cross-section ($\sim 10^{-21} \text{ cm}^2$) of lanthanide ions and the large donor-acceptor distance by spatial separation are largely responsible for the inefficient energy transfer between Tm^{3+} and Er^{3+} .

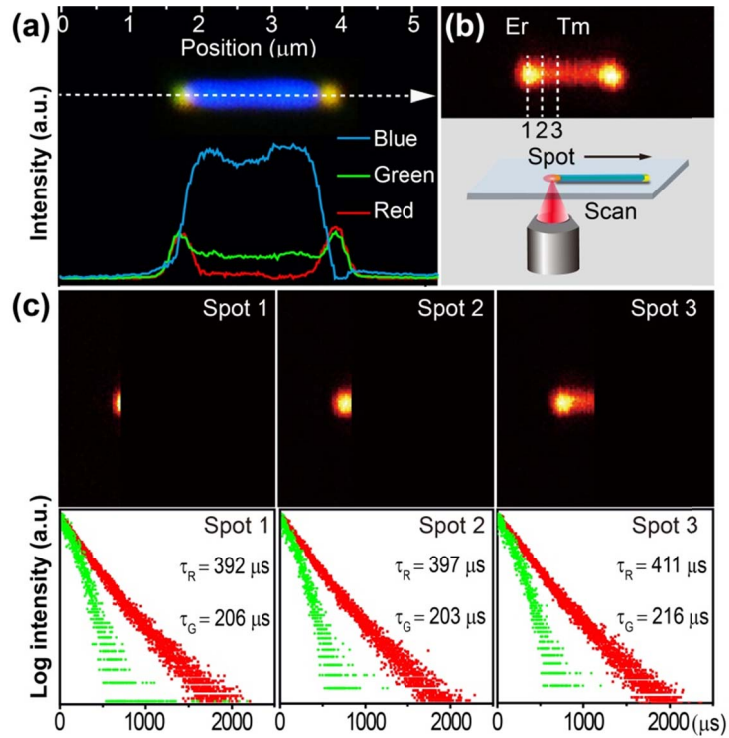


Figure 3.12 (a) Wide-field luminescence image of a single microrod exhibiting YBY dual-color upconversion emission. Note that the color component of the emission can be resolved by RGB acquisition. (b) Confocal microscope image of a different dual-color microrod. (c) The corresponding green (${}^4S_{3/2}$) and red (${}^4F_{9/2}$) emission lifetimes in three different areas (marked with spot 1, 2, 3 shown in b) of the microrod. Note that spot 1 contains only Er^{3+} . Spot 2 contains Er^{3+} and a small amount of Tm^{3+} . Spot 3 is co-doped with Er^{3+} and a large amount of Tm^{3+} .

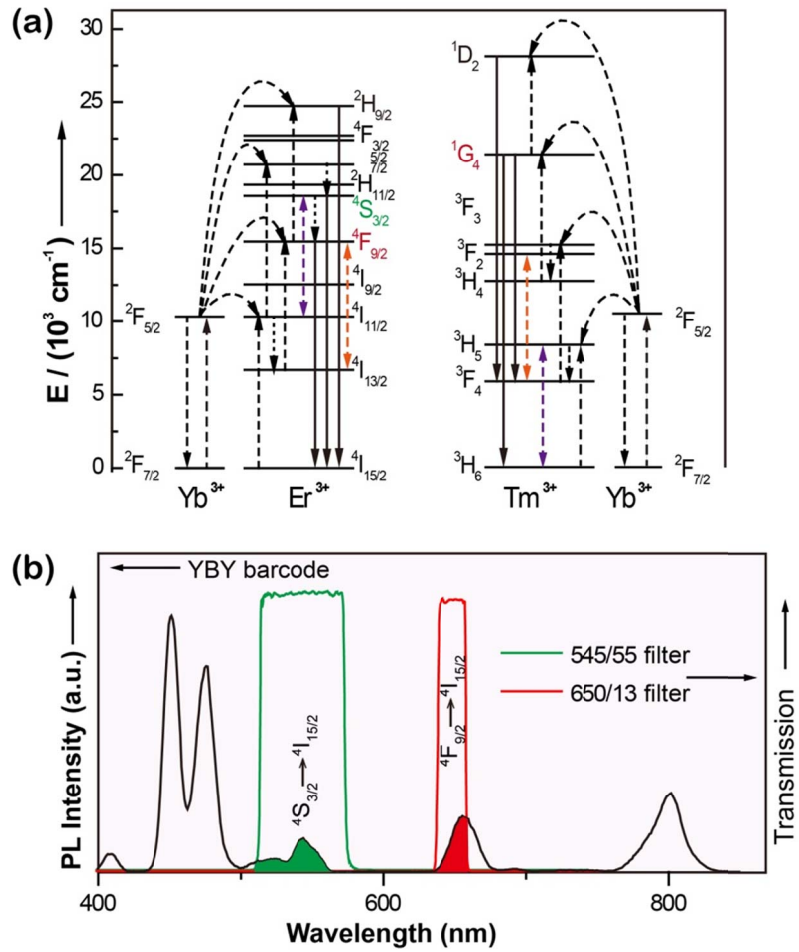


Figure 3.13 (a) Plausible energy transfer pathways between excited Er³⁺ and Tm³⁺ at the tip-junction of a dual-color-emitting (YBY) microrod. The dashed purple and orange arrows show the close match in energy gaps of Er³⁺ and Tm³⁺. However, energy transfer at the tip-junction was not observed, largely due to the intrinsic small absorption cross-section of the lanthanide ions. (b) Upconversion emission spectrum of the tip-modified microrods. Note that transmission spectra of the red and green filters are also shown to reveal the pure chromaticity of the color collected for lifetime measurements. The samples were excited at 980 nm with a 2W diode laser.

3.3.7 Barcoding Crystals for Anti-counterfeiting Application

The use of the as-synthesized multicolor microrods as barcodes for anti-counterfeiting application was further demonstrated in this section. Note that these microrods are dispersible in dimethyl sulfoxide solvent, providing a transparent ink solution under ambient light conditions (Figure 3.14a). As a proof-of-concept experiment, I stamped a solution containing RGR dual-color emitting NaYF₄:Yb/Er nanorods (Yb/Er: 5/0.05 mol% for the green-emitting part and Yb/Er: 50/0.05 mol% for the red-emitting ends) as the security ink onto a paper substrate to create a “NUS” pattern. As a control, an identical pattern using green-color emitting NaYF₄:Yb/Er (10/0.05 mol%) nanorods was generated. When exposed to 980-nm laser light, the two patterns are almost indistinguishable based on emission spectral comparison or color appearance under low magnification (Figure 3.14b and c, insets). Remarkably, we could clearly tell the two patterns apart when zoomed in under high magnification (Figure 3.14b and c). These experiments revealed that the dual-color spatially-coded nanorods can provide added security protection, enabling almost instant verification of patterned features.

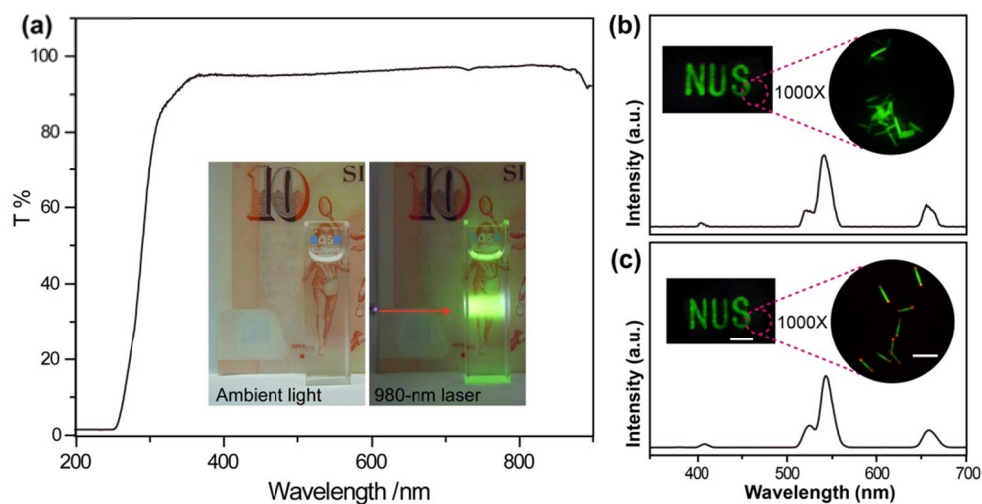


Figure 3.14 (a) Transmission spectrum of the security ink comprising $\text{NaYF}_4:\text{Yb}/\text{Er}$ (10/0.05 mol%) microrods (dispersed in a mixture of DMSO and water). The inserted photos show the transparency ($T > 95\%$ in the range of 400–850 nm) of the nanorod solution under ambient light (left) and the corresponding upconversion luminescence of the solution upon excitation at 980 nm (right). The background is a piece of 10 \$ banknote of Singapore. (b) Luminescence image of a stamped letter S generated with dual-color microrods (shown in 1000 \times magnified image) as the ink. The corresponding upconversion emission spectrum is also shown. Scale bars are 3 μm (right) and 3 mm (left). (c) Luminescence image of a control sample generated with single-color microrods as the ink. Note that the emission spectra (or bulk color appearance) of these two patterns are almost identical. However, their differences in spatial distribution are clearly distinguishable under high magnification.

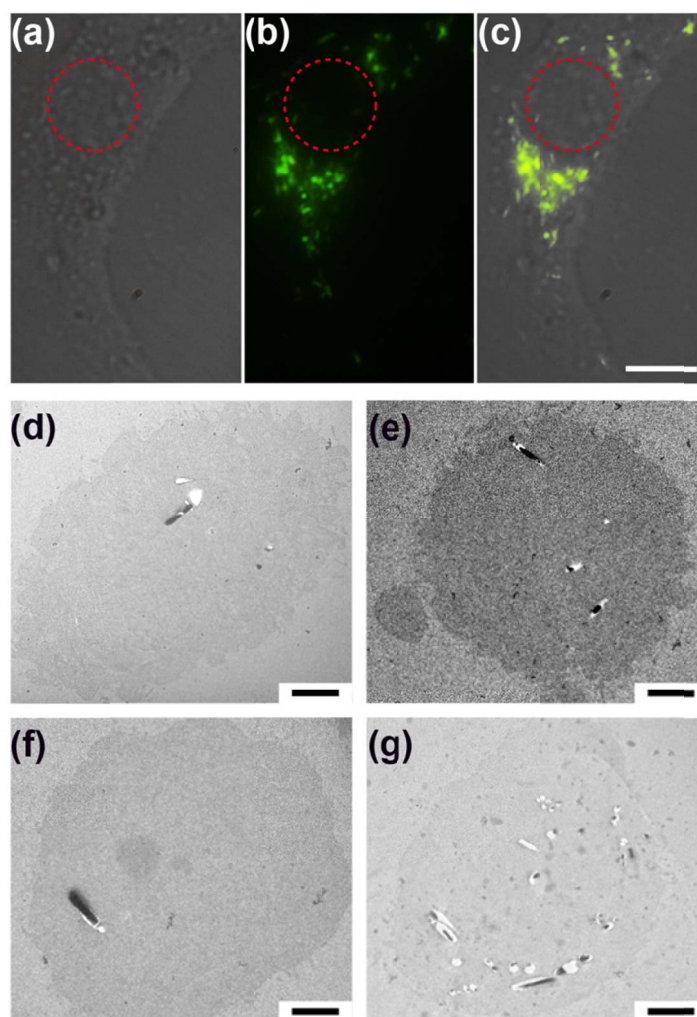


Figure 3.15 (a) Bright-field, (b) upconversion luminescence, and (c) merged images of a single living HeLa cell labeled with green-emitting upconversion microrods. These images were taken with exposure time less than 40 milliseconds. No luminescence was observed in the region of the nucleolus (marked by a dashed circle), indicating that the microrods penetrated through the plasma membrane, but not the nuclear envelope. Scale bar is 8 μm in (c). (d-g) Four typical TEM images of HeLa cells showing that the microrods were indeed internalized by the cells. Note that the breakages in these images are largely induced by slicing during the preparation of cell TEM sample. Scale bar are 3 μm in (d-g).

3.3.8 Barcoding Crystals for Cell Labelling

To explore the use of upconversion nanorods for cell labelling, green emitting nanorods were incubated with HeLa cancer cells for 6 hours. After rinsed with fresh medium, the tagged cells were examined by an optical microscope coupled with a 980-nm laser. As shown in Figure 3.14, a substantial amount of nanorods were uptaken by a single cell, despite the large size of nanorods in the micrometer scale. It is interesting because 100 nm is supposed to be the upper limit of nanoparticles used for cell labelling in previous reports. It is reasoned that the one-dimensional structure of nanorods may play an important role to ease the endocytosis process, analogue to that of carbon nanotube²⁴. Such finding poses positive implications in the quest for multiplexed optical labels.

3.4 Conclusion

My findings in this chapter could provide a convenient model platform for the energy transfer study of lanthanide dopants and bring a better understanding of epitaxial growth to other lanthanide-based anisotropic crystals. The fact that these solution-processable multicolor-banded microrods with good crystalline properties can be easily made on a large scale suggests the prospects of using upconversion phosphor-barcode for optical labeling applications, where low-cost manufacturing of the materials with multi-level optical features are essential. An increased effort dedicating to the investigation of these materials is expected in the near future.

3.5 References

1. Agasti SS, Liong M, Peterson VM, Lee H, Weissleder R. Photocleavable DNA barcode-antibody conjugates allow sensitive and multiplexed protein analysis in single cells. *J. Am. Chem. Soc.* 2012, **134**(45): 18499-18502.
2. He F, Gädt T, Manners I, Winnik MA. Fluorescent “barcode” multiblock co-micelles via the living self-assembly of di- and tri- block copolymers with a crystalline core-forming metalloblock. *J. Am. Chem. Soc.* 2011, **133**(23): 9095-9103.
3. Meruga JM, Cross WM, May PS, Luu Q, Crawford GA, Kellar JJ. Security printing of covert quick response codes using upconverting nanoparticle inks. *Nanotechnology* 2012, **23**(39): 395201.
4. Osberg KD, Rycenga M, Bourret GR, Brown KA, Mirkin CA. Dispersible surface-enhanced raman scattering nanosheets. *Adv. Mater.* 2012, **24**(45): 6065-6070.
5. Goesmann H, Feldmann C. Nanoparticulate functional materials. *Angew. Chem. Int. Ed.* 2010, **49**(8): 1362-1395.
6. Li C, Quan Z, Yang J, Yang P, Lin J. Highly uniform and monodisperse β -NaYF₄:Ln³⁺ (Ln= Eu, Tb, Yb/Er, and Yb/Tm) hexagonal microprism crystals: hydrothermal synthesis and luminescent properties. *Inorg. Chem.* 2007, **46**(16): 6329-6337.
7. Zhang F. *et al.* Uniform nanostructured arrays of sodium rare-earth fluorides for highly efficient multicolor upconversion luminescence. *Angew. Chem. Int. Ed.* 2007, **46**(42): 7976-7979.
8. Wang L, Li Y. Na(Y_{1.5}Na_{0.5})F₆ single-crystal nanorods as multicolor luminescent materials. *Nano Lett.* 2006, **6**(8): 1645-1649.
9. Beurer E, Grimm J, Gerner P, Güdel HU. New type of near-infrared to visible photon upconversion in Tm²⁺-doped CsCaI₃. *J. Am. Chem. Soc.* 2006, **128**(10): 3110-3111.
10. Eliseeva SV, Bünzli J-CG. Lanthanide luminescence for functional materials and biosciences. *Chem. Soc. Rev.* 2010, **39**(1): 189-227.
11. Liu Y, Tu D, Zhu H, Li R, Luo W, Chen X. A strategy to achieve efficient dual-mode

luminescence of Eu^{3+} in lanthanides doped multifunctional NaGdF_4 Nanocrystals. *Adv. Mater.* 2010, **22**(30): 3266-3271.

12. Wang F, Liu X. Upconversion multicolor fine-tuning: visible to near-infrared emission from lanthanide-doped NaYF_4 nanoparticles. *J. Am. Chem. Soc.* 2008, **130**(17): 5642-5643.

13. Wang L, Li P, Li Y. Down- and up- conversion luminescent nanorods. *Adv. Mater.* 2007, **19**(20): 3304-3307.

14. Wang X, Zhuang J, Peng Q, Li Y. A general strategy for nanocrystal synthesis. *Nature* 2005, **437**(7055): 121-124.

15. Zhang Y. *et al.* Multicolor barcoding in a single upconversion crystal. *J. Am. Chem. Soc.* 2014, **136**(13): 4893-4896.

16. Caillat L. *et al.* Multiphoton upconversion in rare earth doped nanocrystals for sub-diffractive microscopy. *Appl. Phys. Lett.* 2013, **102**(14): 143114-143114-143115.

17. Cui J-M, Sun F-W, Chen X-D, Gong Z-J, Guo G-C. Quantum statistical imaging of particles without restriction of the diffraction limit. *Phys. Rev. Lett.* 2013, **110**(15): 153901.

18. Wang X, Zhuang J, Peng Q, Li Y. Hydrothermal synthesis of rare-earth fluoride nanocrystals. *Inorg. Chem.* 2006, **45**(17): 6661-6665.

19. Holzwarth U, Gibson N. The Scherrer equation versus the Debye-Scherrer equation. *Nat. Nanotechnol.* 2011, **6**(9): 534-534.

20. Wang F. *et al.* Simultaneous phase and size control of upconversion nanocrystals through lanthanide doping. *Nature* 2010, **463**(7284): 1061-1065.

21. Li X. *et al.* Successive layer-by-layer strategy for multi-shell epitaxial growth: Shell thickness and doping position dependence in upconverting optical properties. *Chem. Mater.* 2012, **25**(1): 106-112.

22. Zhang F. *et al.* Direct imaging the upconversion nanocrystal core/shell structure at the subnanometer level: Shell thickness dependence in upconverting optical properties. *Nano Lett.* 2012, **12**(6): 2852-2858.

23. Johnson NJ, Korinek A, Dong C, van Veggel FC. Self-focusing by Ostwald ripening:

a strategy for layer-by-layer epitaxial growth on upconverting nanocrystals. *J. Am. Chem. Soc.* 2012, **134**(27): 11068-11071.

24. Kam NWS, Liu Z, Dai H. Carbon nanotubes as intracellular transporters for proteins and DNA: an investigation of the uptake mechanism and pathway. *Angew. Chem.* 2006, **118**(4): 591-595.

25. Wang J. *et al.* Enhancing multiphoton upconversion through energy clustering at sublattice level. *Nat. Mater.* 2014, **13**(2): 157-162

4 CHAPTER 4

Epitaxy Habits in NaLnF₄ System Revealed for Color Multiplexing on Single-crystal Level

4.1 Introduction

Crystal epitaxy has been playing a pivotal role in nanotechnology due to its ability to generate a broad class of heterogeneous materials, including core@shell semiconductor nanoparticles¹, segmented nanowires², sandwiched films³, and hybrid nanoarrays⁴. In particular, epitaxy in lanthanide-doped crystal system has not only enabled the fine control over emission intensity and colors⁵, but also unveiled a new energy upconversion mechanism⁶, i.e., the energy migration upconversion. However, current research in epitaxy over lanthanide-doped crystals is largely limited in epitaxial thickness, usually in nanometer domain. For example, a co-precipitation procedure usually generates a very thin epitaxial shell, typically less than 5 nm in thickness⁷. To achieve desired epitaxy thickness larger than that, one has to repeat the shell-growth procedure multiple times. It is almost impossible for such method to generate a shell thickness beyond 300 nm, a minimum dimension as required by the resolution of an optical microscope when crystals are used for encoding and decoding purpose⁸. Apart from epitaxy thickness, the control over epitaxy orientation has also posed another challenging issue⁹. Although recent studies have made an impressive progress in the regime of nanoscale, the evaluation criterion for epitaxy is mainly based on the shape evolution of nanocrystals. Direct imaging evidence that can identify the orientation of epitaxial crystals is still lacking partially due to the limited resolution of electron microscope in elemental mapping module.

Herein, I report an epitaxy method that is flexible to produce epitaxial shells of tunable thickness, ranging from 300 nm to 2000 nm. Meanwhile, the epitaxy method also enables us to control epitaxy orientation along specific crystalline axis. By using upconversion luminescence as an indicator, the difference between seeding crystal and epitaxial part can be clearly distinguished even if the doping contents are at trace amount level. Eventually, such habits were used to realize color multiplexing on a single-crystal level.

4.2 Materials and Methods

4.2.1 Reagents

Yttrium(III) nitrate (99.9%), ytterbium(III) nitrate (99.9%), thulium(III) nitrate (99.9%), erbium(III) nitrate (99.9%), Yttrium(III) chloride (99.9%), ytterbium(III) chloride (99.9%), thulium(III) chloride (99.9%), erbium(III) chloride (99.9%), sodium hydroxide (NaOH, >98%), ammonium fluoride (NH₄F, >98%), Lutetium(III) chloride hexahydrate (99.9%), oleic acid (90%), sodium citrate (>99%), 1-octadecene (ODE, 90%), Ethylenediaminetetraacetic acid disodium salt dehydrate (EDTA-2Na, >99%), and sodium fluoride (NaF) were all purchased from Sigma-Aldrich and used as received.

4.2.2 Synthetic Methods for Particles of Different Sizes

50-nm NaYF₄ and 150-nm NaYbF₄ Nanoparticles. The β -NaYF₄ nanoparticles were synthesized by a co-precipitation method⁶. In a typical experiment, 3 mL of oleic acid and 7 mL of ODE were mixed with 2 mL aqueous solution of YCl₃ (Yb³⁺/Er³⁺ = 10/0.5 mol%; 0.2 M) in a 50 mL round-bottom flask under vigorous stirring. The resulting mixture was then heated to 150 °C for 1 h to form a transparent lanthanide oleate complex. After cooling down to room temperature, the complex colloidal was added into a methanol solution (6 mL) containing NH₄F (1.6 mmol) and NaOH (1 mmol), followed by evaporation of methanol at 100 °C under stirring. The resulted mixture was then heated to 300 °C and kept at that temperature for 2 h under a flow of nitrogen. The nanoparticles were precipitated by addition of ethanol and collected by centrifugation. Notably, 150-nm NaYbF₄ nanodisks can be also produced following the same procedures as above.

500-nm NaYF₄ Nanodisks. The β -NaYF₄ microdisks were synthesized by a hydrothermal reaction¹⁰. In a typical experiment, NaOH (0.15 g; 3.75 mmol) was first dissolved in 1.5 mL of DI water, followed by addition of 2.5 mL of oleic acid (7.5 mmol) and 2.5 mL of ethanol under vigorous stirring. Thereafter, an aqueous solution of NaF (0.5 M; 2 mL) was added to form a turbid mixture. Subsequently, a 1.2 mL aqueous solution of YCl₃

($\text{Yb}^{3+}/\text{Tm}^{3+} = 10/0.5$ mol%; 0.2 M) was added and the solution was kept stirring for 20 min. The resulting mixture was then transferred into a 14 mL Teflon-lined autoclave and heated to 220 °C for 12 h. After cooling down to room temperature, the reaction product was isolated by centrifugation and washed with ethanol.

5- μm NaLnF_4 (Ln = Yb, Lu, or Y) Microplates. The β - NaLnF_4 microplates were synthesized by a hydrothermal reaction¹¹. Typically, aqueous solutions of sodium citrate (0.5 mL, 0.3 M) and $\text{Ln}(\text{NO}_3)_3$ (2 mL, 0.2 M, Ln = Yb or Lu) were mixed under vigorous stirring to form a milky suspension, into which an aqueous solution of NaF (9.6 mL, 0.5 M) was added to form a transparent colloidal. The resulted colloidal was then transferred to a 14 mL Teflon vessel and heated to 220 °C for 12 h. For the synthesis of 3- μm $\text{NaYF}_4:\text{Yb/Er}$ (20/0.5 mol%) and 1.6- μm $\text{NaYF}_4:\text{Yb/Er}$ (5/0.5 mol%) microplates, different amount of sodium citrate (1.33 mL) and NaF (6.4 mL) were used while keeping other parameters constant.

2- μm NaLnF_4 (Ln = Yb or Y) Microrods. The β - NaYF_4 microdisks were synthesized by a hydrothermal reaction¹². In a typical experiment, NaOH (0.15 g; 3.75 mmol) was first dissolved in 1.5 mL of DI water, followed by addition of 2.5 mL of oleic acid (7.5 mmol) and 2.5 mL of ethanol under vigorous stirring. Thereafter, an aqueous solution of NH_4F (2 M; 0.5 mL) was added to form a turbid mixture. Subsequently, a 1 mL aqueous solution of YCl_3 ($\text{Yb}^{3+}/\text{Er}^{3+} = 80/0.5$ mol%; 0.2 M) was added and the solution was kept stirring for 20 min. The resulting mixture was then transferred into a 14 mL Teflon-lined autoclave and heated to 220 °C for 12 h. After cooling down to room temperature, the reaction product was isolated by centrifugation and washed with ethanol.

10- μm NaLnF_4 (Ln = Yb or Y) Microrods. The β - NaLnF_4 microrods were synthesized by a hydrothermal reaction. Typically, aqueous solutions of EDTA-2Na (3.75 mL, 0.2 M), LnCl_3 (1.5 mL, 0.2 M), NH_4F (4 mL, 2 M), and NaF (8 mL, 0.5 M) were mixed under vigorous stirring to form a transparent suspension, into which aqueous solutions of HCl (1.5 mL, 2 M) and HNO_3 (10 mL, 2 wt%) were added to form a milky colloidal. The resulted colloidal was then transferred to a 40 mL Teflon vessel and heated to 220 °C for 12 h.

4.2.3 Seeded Epitaxial Growth of NaLnF_4 Crystals

General Considerations on Epitaxial Growth. It is noteworthy that the preferable growth orientation is determined by several hydrothermal conditions, including not only surfactant, but also pH value, temperature, concentration of NaF, *etc.* Generally speaking, the orientation preference of epitaxy in seed-free condition retains in seeded growth condition. For example, hydrothermal condition *a* (220 °C, sodium citrate, excessive NaF) favors the crystal growth along *a* axis in the absence of seeding crystals, generating microplate with aspect ratio of 5; meanwhile, such condition affords similar crystals in the presence of certain amount of seed crystals. The amount of pre-added seeding crystals solely determines the size of end product. In practice, the amount of seed crystals can be estimated using the following equation:

$$\frac{n_s}{n_c} = \frac{\rho_{c/s} V_{c/s} / M_{c/s} - \rho_c V_c / M_c}{\rho_c V_c / M_c} \approx \frac{V_{c/s}}{V_c} - 1 = \frac{r_{c/s}^2 h_{c/s}}{r_c^2 h_c} - 1$$

where, n is the mole amount of substance, ρ is the volumetric density of NaLnF₄, V is the volume of NaLnF₄ crystals, M is the molar mass of NaLnF₄, r is the edge length of the cross-section of hexagonal crystal, h is the thickness of the disk, subscripts s , c , and c/s denote the shell, core and core/shell structures, respectively. For example, in order to produce core/shell microplates ($r_{c/s} = 2.5 \mu\text{m}$, $h_{c/s} = 1 \mu\text{m}$) using nanoplates ($r_c = 0.25 \mu\text{m}$, $h_c = 0.1 \mu\text{m}$) as seeds, the molar ratio of shell precursor and seeds is $n_s/n_c \approx 1000$, indicating that 0.4 μmol of seed crystals is sufficient for a thorough epitaxy in a standard trial (0.4 mmol shell precursor).

Preparation of Seeding Crystals. Broadly, all those as-synthesized NaLnF₄ crystals, including 50-nm nanoparticles, 200-nm nanodisks, 500-nm nanodisks, 3- μm microplates, and 2- μm microrods, can be used as seeds for epitaxy study. To qualify a good seeding material, the as-prepared NaLnF₄ crystals were first treated with HCl to remove the surface ligands, generating a class of ligand-free seeds. Typically, a cyclohexane solution of 50-nm NaYF₄ nanoparticles coating with oleic acid (1 mL; 0.02 M) was first mixed with 1 mL ethanol and then centrifuged at 5000 rpm. The isolated particles were mixed with 1 mL of ethanol and 1 mL of HCl aqueous solution (2 M), followed by sonication for 5 min to remove the ligands thoroughly. Subsequently, the particles were centrifuged and alternatively washed by ethanol

and water for 2 times. The ligand-free particles were dispersed in 1 mL water for future use as seeds. Other crystals, such as 200-nm nanodisks, 500-nm nanodisks, 3- μm microplates, and 2- μm microrods, were treated following the same procedures as above to generate decent seed materials.

4.2.4 Epitaxy Along a -axis (a -condition)

The epitaxial growth along a axis of NaLnF_4 seeds was conducted in a hydrothermal reaction using sodium citrate as the surfactant. Typically, aqueous solutions of sodium citrate (0.5 mL, 0.3 M) and $\text{Ln}(\text{NO}_3)_3$ (2 mL, 0.2 M, Ln = Yb or Lu) were mixed under vigorous stirring to form a milky suspension, into which an aqueous solution of NaF (9.6 mL, 0.5 M) was added to form a transparent colloidal. The resulted colloidal was mixed with certain amount of seed crystals (50-nm nanoparticles, 500-nm nanodisks, 3- μm microplates, or 2- μm microrods), and then transferred to a 14 mL Teflon vessel and heated to 220 °C for 12 h.

4.2.5 Epitaxy Along c -axis (c -condition)

The epitaxial growth along c axis of NaLnF_4 seeds was conducted in a hydrothermal reaction using EDTA-2Na as the surfactant. Typically, aqueous solutions of EDTA-2Na (3.75 mL, 0.2 M), LnCl_3 (1.5 mL, 0.2 M), NH_4F (4 mL, 2 M), and NaF (8 mL, 0.5 M) were mixed under vigorous stirring to form a transparent suspension, into which aqueous solutions of HCl (1.5 mL, 2 M) and HNO_3 (10 mL, 2 wt%) were added to form a milky colloidal. The resulted colloidal was mixed with certain amount of 2- μm microrods as seed, and then transferred to a 40 mL Teflon vessel and heated to 220 °C for 12 h.

4.2.6 Physical Measurements

TEM measurements were carried out on a JEOL-JEM 2010F field emission TEM operated at an acceleration voltage of 200 kV. Elemental mapping was carried out with JED-2300T EDX (energy dispersive x-ray spectrometer) system at 200 kV on a JEOL JEM-2100 LaB_6 TEM. XRD data were collected on a Bruker D8 Advance diffractometer using graphite-monochromatized $\text{CuK}\alpha$ radiation ($\lambda = 1.5406 \text{ \AA}$). Luminescence spectra were recorded at room temperature with a DM150i monochromator equipped with a R928 photon counting

CHAPTER 4

photomultiplier tube and a 980-nm diode laser. Upconversion luminescence imaging was performed using an upright Olympus BX51 microscope coupled with a 980-nm diode laser through fiber output. Luminescence micrographs were recorded with a Nikon DS-Ri1 imaging system. Digital photographs of security patterns were taken under 980-nm laser excitation by a Nikon D700 camera. SEM imaging was performed on a JEOL JSM-6701F SEM (field-emission) equipped with cold field emission electron source and accelerating voltage of 5 kV.

4.3 Results and Discussion

4.3.1 Seeding Crystals

The epitaxy method used in this chapter is based on a hydrothermal procedure, in which all those reactants are subject to an environment of high pressure (~30 bar) and high temperature (220 °C) for a substantially long period (12 hour).

In a typical epitaxy experiment, I start with the synthesis of seeding crystals of various sizes spanning from 50 nm to 3 μm in diameter. Note that the size of the particles is determined by both the composition of crystal and the specific synthetic method. For example, given using an identical co-precipitation method, 50-nm NaYF₄ nanocrystals and 150-nm NaYbF₄ nanocrystals can be produced, respectively, due to the composition difference (Figure 4.1); given using an identical material like NaYbF₄, 150-nm nanocrystals and 5-μm microcrystals can be produced by co-precipitation method and hydrothermal method, respectively (Figure 4.1b and Figure 4.2c). Interestingly, the morphology of the microcrystals can be tailored from disks into rods by the use of different surfactants (Figure 4.3), such as citric acid and ethylenediaminetetraacetic acid (EDTA). Notably, the hydrothermal conditions for preparation of seeding crystals will be further used as the epitaxy conditions for controlled epitaxy in thickness and orientation (*vide infra*).

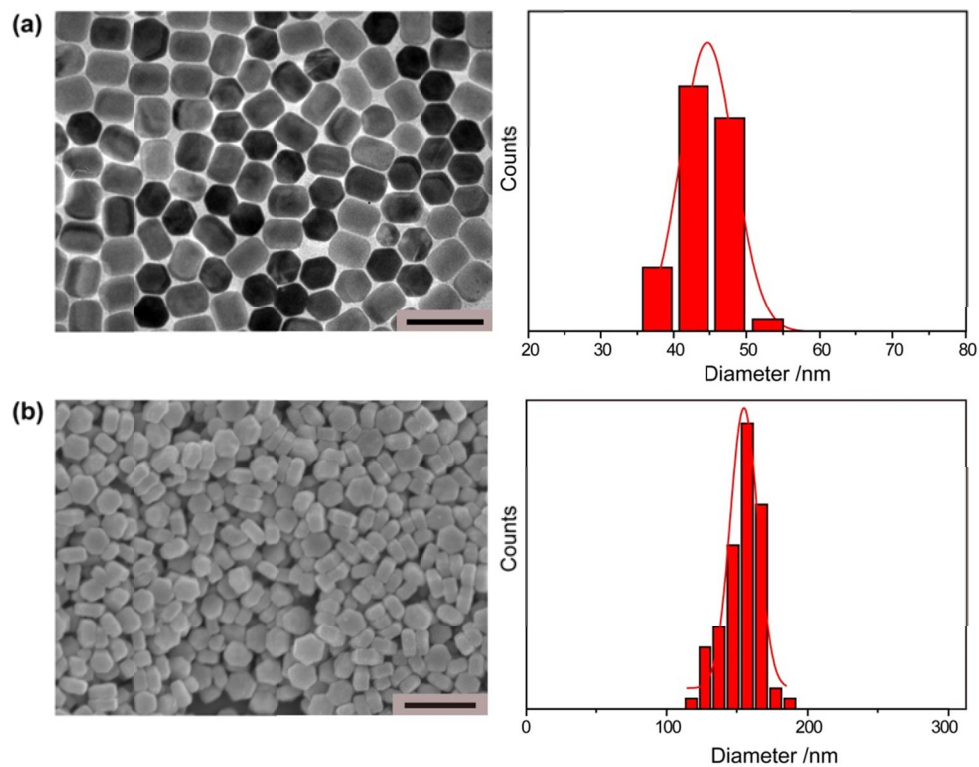


Figure 4.1 (a) A typical TEM image showing the as-synthesize NaYF₄ nanocrystals with a feature size of 47 nm. Scale bar is 100 nm. (b) A typical SEM image showing the as-synthesize NaYbF₄ nanocrystals with a feature size of 158 nm. Scale bar is 400 nm. Note that these two types of nanocrystals with different sizes were synthesized through an identical co-precipitation method.

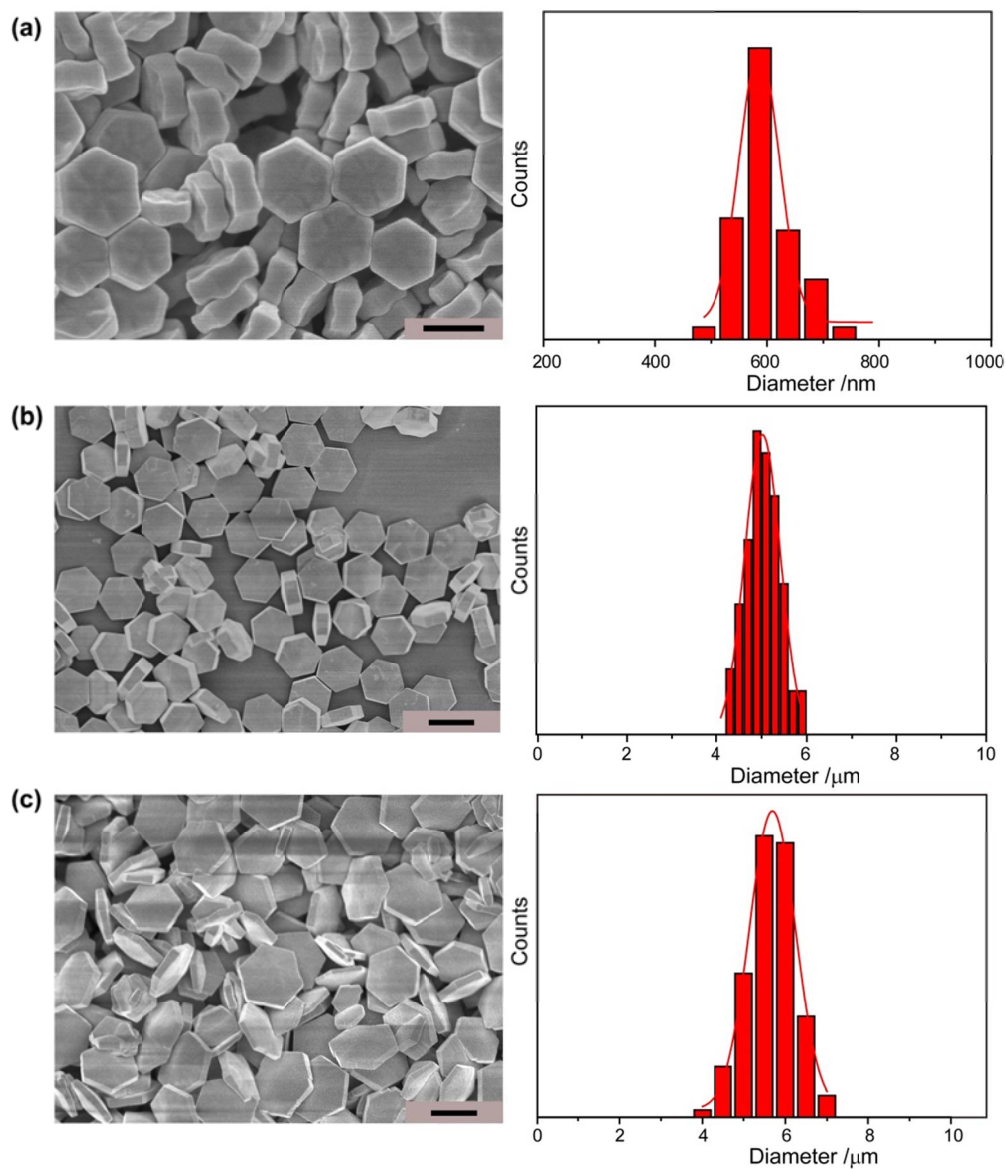


Figure 4.2 Typical SEM images of as-synthesized NaLnF₄ hexagon-like crystals by using a hydrothermal reaction: (a) NaYF₄ (b) NaLuF₄ and (c) NaYbF₄. Scale bar represents 500 nm in (a), and 5 μm in (b) and (c), respectively.

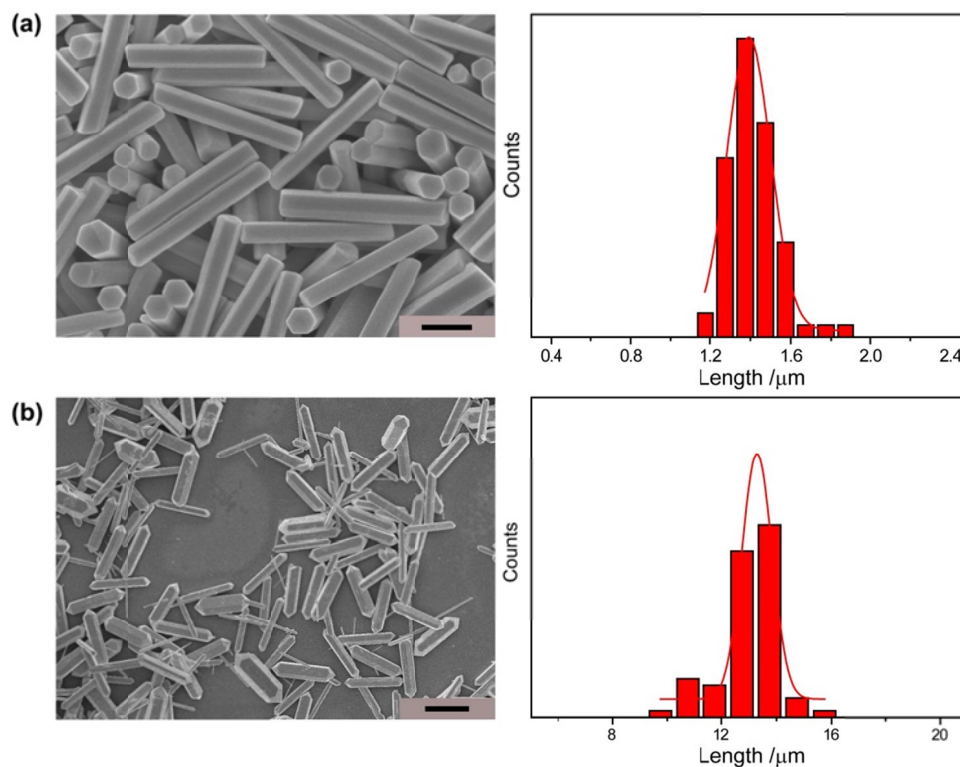


Figure 4.3 Rod-like NaLnF₄ crystals of various lengths synthesized through a hydrothermal method. **(a)** SEM image of NaYF₄ nanorods with a feature length of 1.5 μm. Scale bar represents 1 μm. **(b)** SEM image of NaYbF₄ nanorods with a feature length of 13 μm. Scale bar represents 10 μm.

4.3.2 Epitaxy on Seeding Crystals

Next, an epitaxy precursor comprising of NaF, H₂O, sodium citrate and LuCl₃, was prepared at room temperature. To conduct an epitaxy experiment, seeding crystals and epitaxy precursor were simply mixed in a certain molar ratio (see page 71) and sealed the reaction system in a hydrothermal reactor before moving into a heating oven (Figure 4.4a). Note that Yb/Er and Yb/Tm pairs were intentionally doped into core and shell, respectively, to introduce distinct upconversion luminescent colors that can be used as indicators to evaluate the yield and uniformity of core@shell product. Since the dimensions of both the core (3- μ m in diameter) and the shell (700 nm in thickness, Figure 4.4c) are larger than optical diffraction limit (300 nm), a conventional optical microscope coupled with a 980-nm laser becomes available for examining the morphology and quality of epitaxy structure. Figure 4.4d represents an upconversion luminescent image of the seeding crystal, clearly showing its hexagonal morphology and a yellowish color. After epitaxy in hydrothermal condition, almost all of the seeding crystals were rimmed with bluish shell crystals (Figure 4.4e), exhibiting a high uniformity of epitaxy product. The high epitaxy yield can be attributed to the closely matching of the crystalline lattices between NaYF₄ and NaLuF₄. In fact, those hybridized epitaxies among NaYF₄, NaYbF₄ and NaLuF₄ material systems are all workable due to their similar lattice constants.

The compositional difference of the heterogeneous structure was further revealed by an elemental mapping measurement (Figure 4.4f). It is noted that the upconversion luminescence induced by the trace amount doping of Yb/Tm is particularly useful to identify the epitaxial thickness or orientation when the host materials of core and shell are identical or similar in atomic number, where elemental mapping technique is disabled. For example, NaYbF₄@NaLuF₄ poses an overlapped signal (characteristic peaking at Yb-L _{α} = 7.4 keV, and Lu-L _{α} = 7.6 keV) during electron mapping process, leaving the upconversion luminescence an indispensable means to distinguish core and shell (Figure 4.5). Interestingly, the epitaxy orientation is found highly preferred along *a* axis rather than *c* axis, as evidenced by the difference of increments in diameter (~1.6 μ m) and thickness (~0.2 μ m). Although being

orientated, the epitaxy provides a fully coverage of inert shell over the core (Figure 4.6), efficiently alleviating the surface quenching effect. Such passivation effect is verified by a 30% enhancement in emission intensity from a single particle before and after epitaxy (Figure 4.4g).

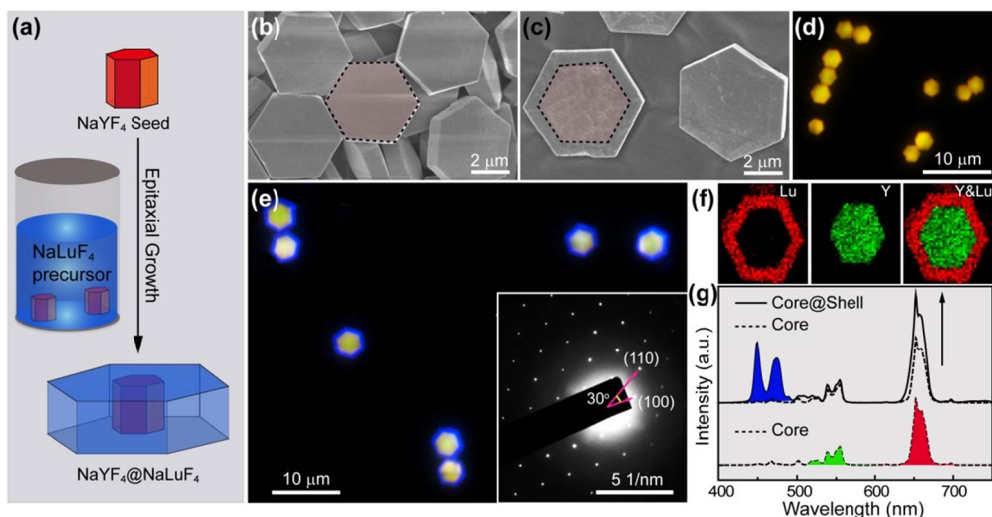


Figure 4.4 (a) Schematic shows the epitaxy process conducted in a hydrothermal reactor containing seeding crystals, and epitaxy precursor comprising Na⁺, Lu³⁺, F⁻, sodium citrate (surfactant). (b) Typical scanning electron microscopic image of hexagonal-phase NaYF₄:Yb/Er (20/0.5 mol%) seeding crystals. (c) Scanning electron microscopic image of NaYF₄:Yb/Er (20/0.5 mol%)@NaLuF₄:Yb/Tm (5/0.5 mol%) core@shell crystals that are obtained from an epitaxial growth over NaYF₄:Yb/Er (20/0.5 mol%) seeding crystals. The highlighted pink hexagon shows an identical shape and size to the core crystal. (d-e) Luminescent micrographs of the core and core@shell crystals under an excitation of a 980-nm laser. Inset in e shows the selected area electron diffraction pattern taken at the edge of a single core@shell crystal. (f) Elemental mapping image conducted on a single core@shell microcrystal by the use of an energy dispersive x-ray (EDX) spectrometer. (g) Upconversion emission spectra of a single core and core@shell crystal, respectively. The arrow indicates an emission enhancement that is granted by a shell passivation effect. Note that three parallel measurements were conducted to avoid random errors on single-particle spectra collection.

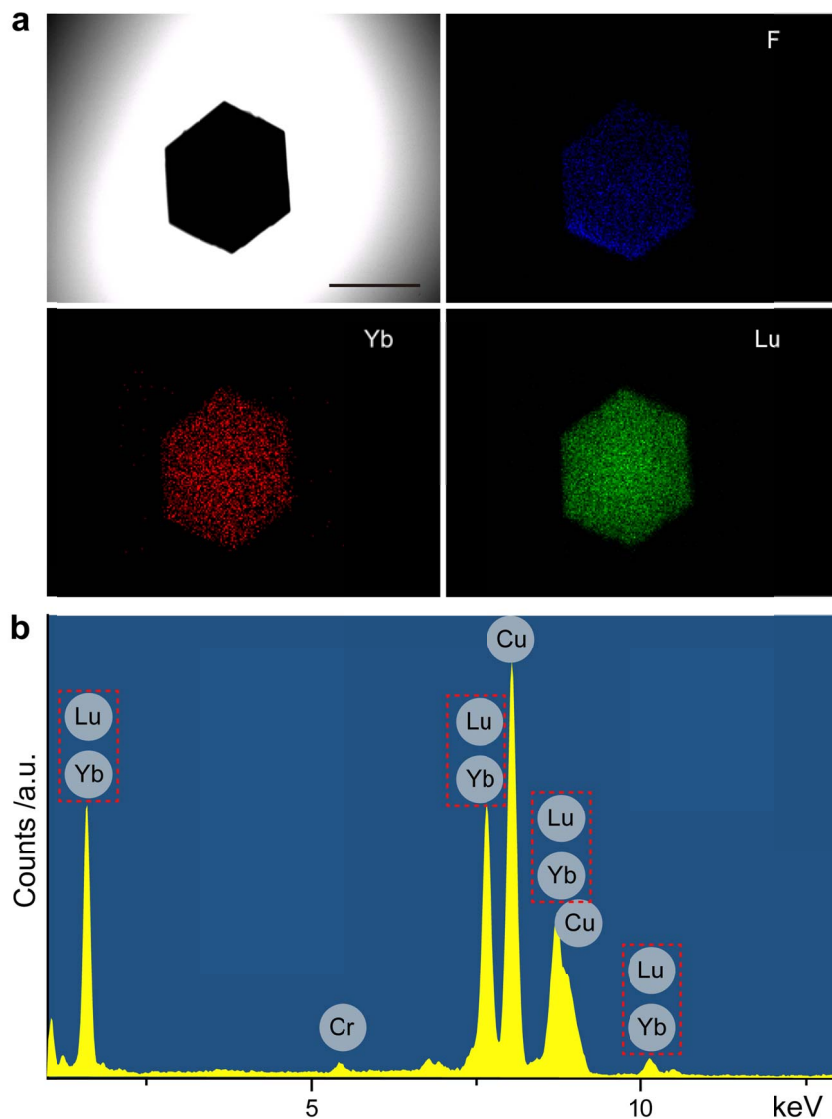


Figure 4.5 (a) A typical TEM image and corresponding elemental mapping images of $\text{NaYbF}_4 @\text{NaLuF}_4$ core@shell crystals. Scale bar is 3 μm . Note that the characteristic energy peaks for Yb and Lu in energy-dispersive x-ray spectroscopy (EDX) are essentially overlapping, making the EDX technique not capable of distinguishing these two elements. As a result, the elemental mapping is not able to render a clear core@shell heterogeneous structure. (b) EDX spectrum of a single $\text{NaYbF}_4 @\text{NaLuF}_4$ core@shell crystal, showing the overlap of characteristic peaks of Yb and Lu elements.

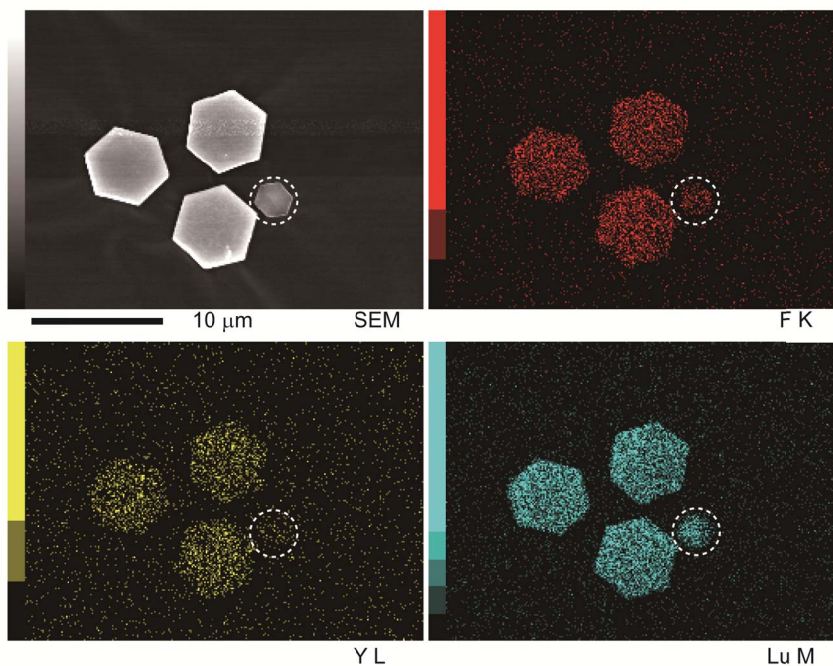


Figure 4.6 A typical SEM image and corresponding elemental mapping images of $\text{NaYF}_4:\text{Yb}/\text{Er}$ (20/0.5 mol%)@ $\text{NaLuF}_4:\text{Yb}/\text{Tm}$ (5/0.5 mol%) core@shell crystals. Note that the SEM elemental mapping technique is specified to probe the surface composition with limited depth (depending on acceleration voltage). The elemental maps show a much stronger Lu signal rather than Y, indicating that the core@shell structure is fully covered with a NaLuF_4 crystal layer. The dashed circle shows a second phase generated from the synthesis, comprising mainly NaLuF_4 crystals as evidenced by the strong Lu signal.

4.3.3 Kinetics and Thermodynamics of Epitaxy

To shed light on the kinetics of epitaxy, five parallel experiments using emissive core (1.6- μm $\text{NaYF}_4\text{:Yb,Er}$ crystals) and non-emissive epitaxy precursor (NaYbF_4 precursor) were conducted. To yield a set of samples showing the evolution of crystal epitaxy, they were subsequently quenched by wind-cooling at varied time intervals using a regular electrical fan. Remarkably, such hydrothermal-based epitaxy approach readily affords gram-scale uniform core@shell crystals (~ 50 mg per trial), providing sufficient amount of samples for statistical analysis. Those obtained samples were examined by upconversion luminescence microscope, X-ray diffraction spectroscopy (XRD) and scanning electron microscope (SEM), respectively. Luminescent micrographs (Figure 4.7) show that the epitaxy was initiated from the seeding crystal and started to grow symmetrically along the crystalline a axis. The dimensions of those samples were plotted against reaction time according to SEM data analysis (Figure 4.7, right panel). The thickness of shell increased from 500 nm to 2 μm after the whole epitaxy reaction. Notably, the whole epitaxy process exhibits diverse epitaxy speeds, based on which it can be categorized into three stages, the initial stage (0-0.5 h), the fast-growing stage (0.5-2 h), and the Ostwald rippling stage (2-10 h). In the first stage, the epitaxy precursor forms, as temperature increasing ($T < 220$ $^\circ\text{C}$), a large amount of NaYbF_4 (cubic-phase) nanocrystals; in the second stage, those nanoparticles undergo a phase-transition from cubic-phase to hexagonal-phase ($T = 220$ $^\circ\text{C}$), and concurrently recrystallize onto seeding crystals. In the last stage, Ostwald rippling occurs among NaYbF_4 particles of different sizes, leading to a slight increment of the crystal size from 5.3 μm to 5.5 μm . Such kinetic study in epitaxy enables us to quantitatively measure the epitaxy speed (i.e., the line-segment-slope in Figure 4.10a) along crystal axis. For example, the epitaxy speeds in hydrothermal condition are determined to be ~ 43 nm/min along a axis and ~ 7 nm/min along c axis in fast-growing stage, both being 2 orders of magnitude faster than that in conventional co-precipitation method. These data allow us to obtain desired epitaxy thickness by simply quenching the epitaxy reaction at certain reaction time.

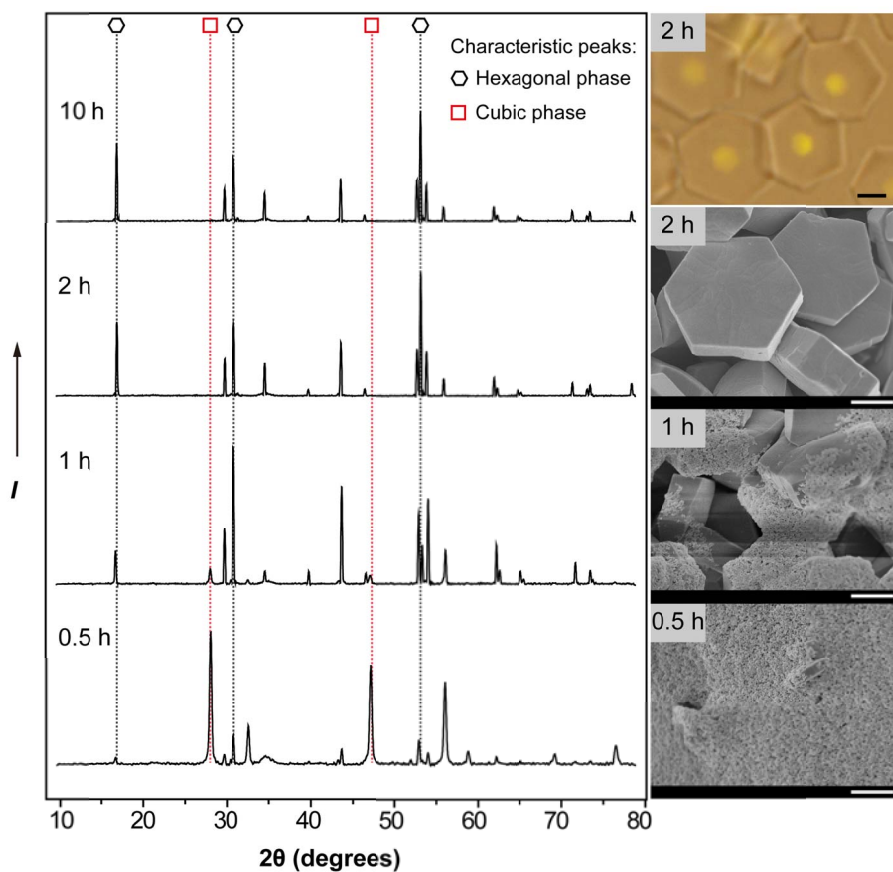


Figure 4.7 Kinetic study of a typical epitaxy growth in NaYbF_4 crystal system. Left panel shows the XRD pattern evolution against reaction time, suggesting that the epitaxy of the NaYbF_4 crystals involves a phase transition of epitaxy precursor from cubic phase to hexagonal phase. The dashed lines in red and dark represent the characteristic diffraction peaks of cubic phase and hexagonal phase, respectively. Right panel shows three SEM images (three at the bottom) of epitaxy product at various reaction times, and a bright field optical micrograph (at the top) taken under 980-nm laser excitation. Note that 1.6- μm $\text{NaYF}_4\text{:Yb/Er}$ (5/0.5 mol%) microcrystals were used as seeds in these kinetic experiments. All scale bars are 1 μm in right panel.

As an alternative tool to achieve tunable epitaxy thickness, control over feeding ratio of shell-precursor/seed seems more superior when compared to quenching method due to the fact that it allows generating pure target crystals without any byproduct (i.e., cubic-phase nanocrystals). Indeed, high-quality hexagonal $\text{NaYbF}_4:\text{Er}@\text{NaYbF}_4$ crystals were generated in a set of thermodynamic experiments where all epitaxial growths were allowed to fully complete in sufficient reaction times (~ 12 hours). It is observed that the shell thickness increases from 300 nm to 1700 nm along with the increasing ratios of shell-precursor/seed from 100 to 800 (Figure 4.8). Such finding provides us a versatile method to produce upconversion particles with tunable sizes spanning from nano- to micro- region. It should be mentioned, however, the particle can't be arbitrarily enlarged by increasing the amount of shell-precursor. A maximum diameter of 5.4 μm was found at feeding ratio of 2000, where another phase (~ 2.1 μm in diameter) comprising pristine NaYbF_4 composition emerged (Figure 4.10b). Interestingly, when no seeding crystals are introduced into epitaxy system (shell/seed ratio $\rightarrow \infty$ in seedless condition), the shell precursor forms uniform NaYbF_4 crystals with a feature size of ~ 5.7 μm under an identical experimental condition (Figure 4.2c). It is thus reasonable to postulate that seeded growth condition is incapable to produce larger particles when compared to seedless growth condition. To verify this assumption, a similar thermodynamic experiment was conducted in another material system, i.e., NaLuF_4 epitaxy system (Figure 4.9). Our experiment results show that, NaLuF_4 crystals that formed in seedless condition have a feature diameter about 5.2 μm (Figure 4.2b); when certain amount of NaYF_4 nanoparticles were introduced as seeding crystals beforehand, the obtained epitaxial product has a maximum diameter of 3.5 μm , which is indeed smaller than those crystals synthesized in seedless condition. Such an epitaxy habit may benefit us on selecting suitable systems for epitaxial growth. For example, in order to obtain an epitaxial product with a target size of 10 μm , the epitaxy system should have an ability to produce crystals larger than 10 μm under a seedless condition. This epitaxy habit will be further testified in one-dimensional NaLnF_4 crystal systems in the following section.

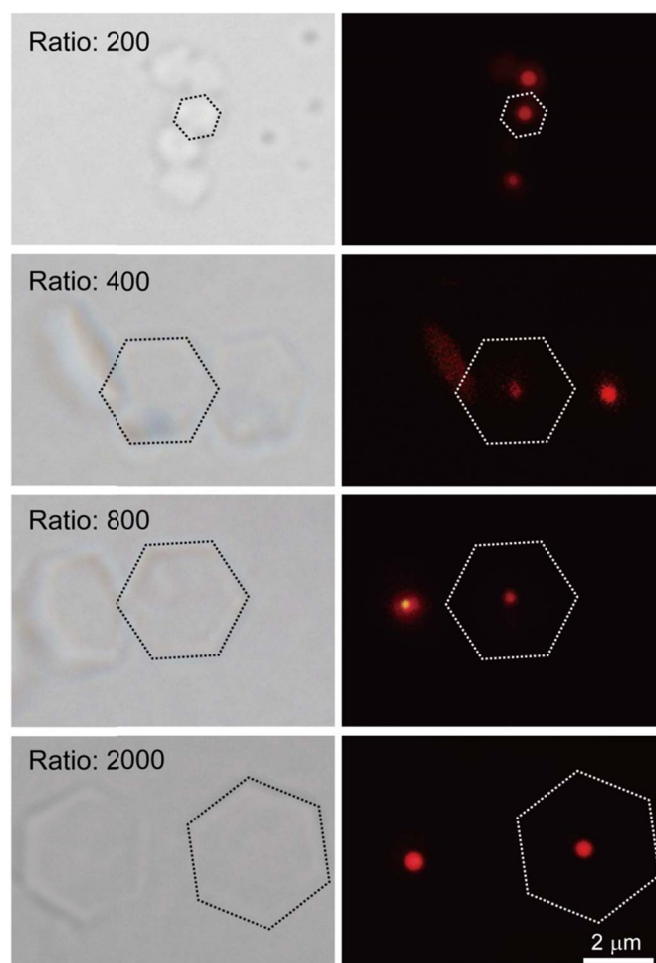


Figure 4.8 Thermodynamic study of a typical epitaxy growth in NaYbF_4 crystal system. Optical microscope images of $\text{NaYbF}_4\text{:Er@NaYbF}_4$ core@shell microcrystals, showing the diameter evolution as the feeding ratio of precursor/seeds increases. Note that the seeding crystals used in these thermodynamic experiments are 150-nm $\text{NaYbF}_4\text{:Er}$ (0.5 mol%) nanocrystals.

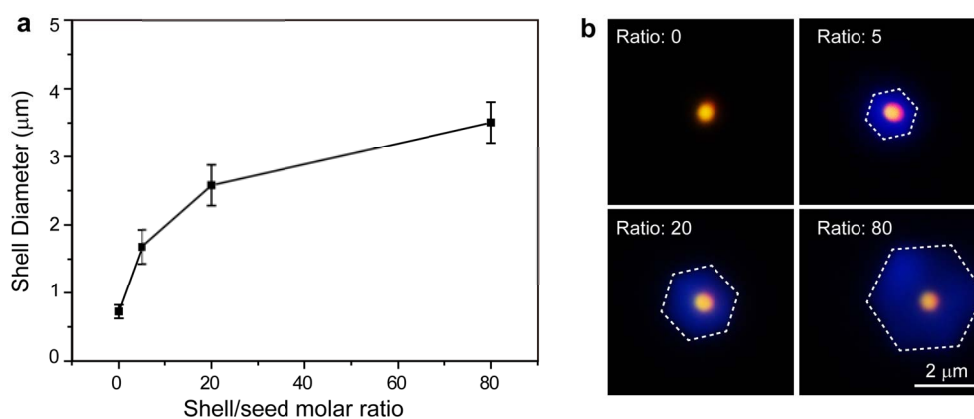


Figure 4.9 Control experiment shows the existence of a maximum size around 3.5 μm in NaLuF_4 crystals epitaxy system. **(a)** Diameter of end product in a NaLuF_4 :Yb/Tm (5/0.5 mol%) epitaxial system increases with increasing feeding molar ratios of shell-precursor/seed. Note that the seeding crystals are small hexagonal NaYbF_4 :Er (0.5 mol%) crystals of a diameter of 800 nm. **(b)** Representative upconversion luminescent micrographs of as-synthesized epitaxial crystals under various feeding ratios. Scale bar is 2 μm .

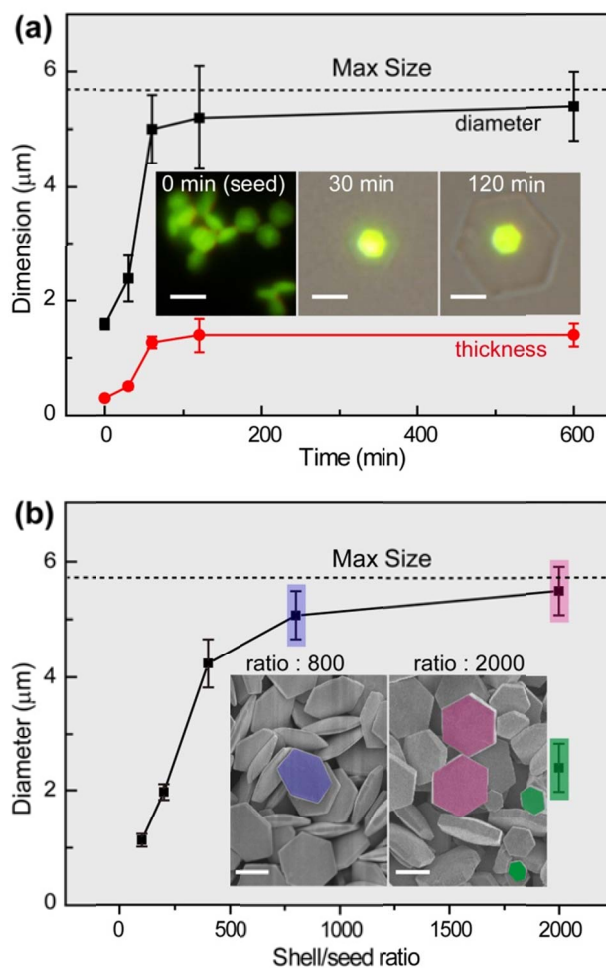


Figure 4.10 Kinetic and thermodynamic study of a typical epitaxy growth in NaYbF₄ system, showing a maximal crystal size limited by seedless hydrothermal condition. **(a)** Dimension evolution curve of NaYbF₄ crystals in thickness and diameter against epitaxy time when green emitting NaYF₄:Yb/Er (5/0.5 mol%) crystals (1.6 μm in diameter) were used as seeds. Insets represent the optical micrographs of samples retrieved in varied time intervals. **(b)** Diameter of thermodynamic product in a NaYbF₄ epitaxial system increases with increasing feeding ratios of shell-precursor/seed. Inset shows two scanning electron microscopic images of NaYbF₄ crystals that are obtained at a shell/seed ratio of 800 and 2000, respectively. An excessive feeding of epitaxy precursor (shell/seed ratio: 2000) results in a phase separation, as shown in pink and green color. Note that small NaYbF₄:Er (0.5 mol%, 150 nm in diameter) nanodisks were used as seeding crystals in the thermodynamic study. All scale bars are 2 μm. The dashed lines in both figures show a size of the crystals (5.7 μm) that obtained under a seedless hydrothermal condition.

4.3.4 Epitaxy Orientation Control

In an attempt to control the epitaxy orientation, I developed another hydrothermal procedure that can afford one-dimensional NaYbF₄ crystals of 13 μm in length. In this procedure, ethylenediaminetetraacetic acid (EDTA), instead of citric acid, was used as surfactant to encourage an orientated growth along *c* axis. Note that, however, the preferred orientation of crystallization is not exclusively determined by surfactant, but by a set of synergistic conditions, such as temperature, ion concentration, solvent, pH, and surfactant. With regard to conciseness, the hydrothermal condition generating 2D plate-like crystals was denoted as *a*-condition, while that generating 1D rod-like crystals as *c*-condition in the following context. *C*-condition was used as epitaxy system to conduct epitaxial growth over rod-like seeding crystals. It is found that the epitaxy preference along *c* axis is maintained in a seeded system, generating a class of segmented crystals as shown in Figure 4.11. As expected, the epitaxial length increases with increasing epitaxy-precursor/seed ratio before reaching a maximum length of 13 μm (Figure 4.3b). Such finding is consistent with those epitaxy habits pertaining in *a*-condition, indicating that the existence of a maximum epitaxy size is a general feature of hydrothermal-reaction based epitaxy regardless of the variation of epitaxy conditions. Another notable observation is that, the epitaxy orientation is not influenced by the morphology of the seeding crystals. To elucidate this point, rod-like crystals were used, instead of plate-like crystals, as seeding crystals to conduct epitaxy in *a*-condition. As shown in Figure 4.11 e-g, a set of rod-centered prism-like crystals were obtained, strongly indicating that the epitaxy preference along *a* axis is maintained just as that when using plate-like crystals as seeds.

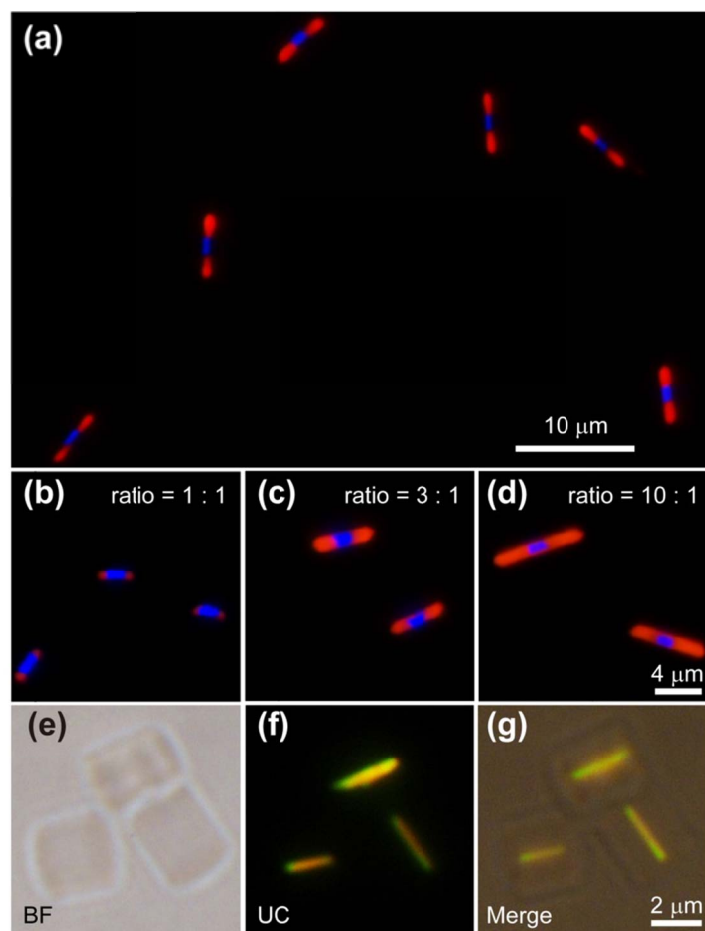


Figure 4.11 Epitaxy orientation control over c axis and a axis when using NaYF_4 nanorods as the seeding crystals. **(a)** An optical micrograph showing the high-yield segmented one-dimensional crystals that are obtained from c -orientated epitaxy (c -condition). The composition of these segmented crystals is $\text{NaYbF}_4:\text{Er}$ (0.5 mol%, red)/ $\text{NaYF}_4:\text{Yb/Tm}$ (5/0.5 mol%, blue)/ $\text{NaYbF}_4:\text{Er}$ (0.5 mol%, red). **(b-d)** Luminescent micrographs of segmented crystals with varied epitaxy lengths that are controlled by molar ratio of epitaxy-precursor/seed in reaction system. **(e-g)** Optical micrographs of core@shell hexagonal prism crystals that are obtained from a -condition. The seeding crystal is composed of $\text{NaYF}_4:\text{Yb/Er}$ (20/0.5 mol%, yellowish) nanorod, while the shell crystal comprises pristine NaYbF_4 crystal. Note that all these luminescent images were taken under an excitation of 980-nm laser.

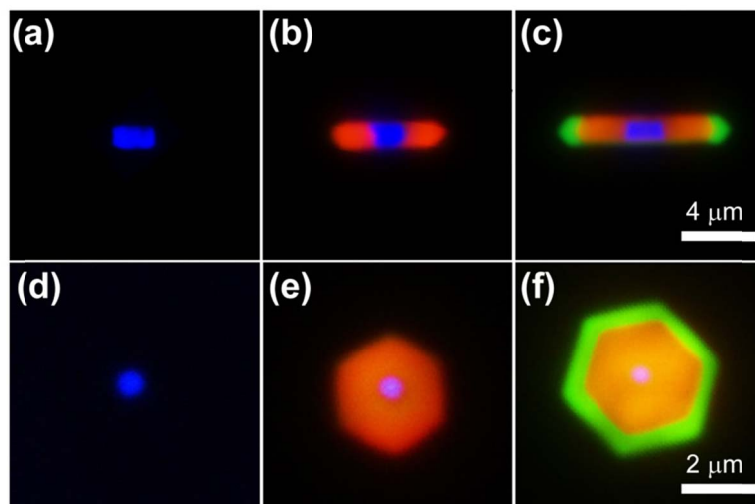


Figure 4.12 Construction of multicolor NaLnF_4 crystals by multi-step epitaxy. **(a-c)** Optical micrographs showing the evolution of a one-dimensional crystal. **(a)** shows a seeding $\text{NaYF}_4:\text{Yb/Tm}$ (60/2 mol%) microrod; **(b)** shows a three-segment microrod after first epitaxy; the red segment is comprised of $\text{NaYbF}_4:\text{Er}$ (2 mol%); **(c)** shows the five-segment microrod; the green segment is comprised of $\text{NaLuF}_4:\text{Yb/Er}$ (5/2 mol%). **(d-f)** Optical micrographs showing the evolution of a two-dimensional crystal. The composition of epitaxy precursor is identical to that used in **a-c**. Note that all these luminescent images were taken under an excitation of 980-nm laser.

Based on the above experiments, two fundamental epitaxy habits under hydrothermal conditions can be generalized. First, the epitaxial growth in seeding condition has a tendency to form crystals of a similar morphology to that produced in a seedless condition; second, the epitaxy orientation is not determined by the morphology of seeding crystals, but determined by the epitaxy environments. Such habits are particular useful since they allow us to design and synthesize heterogeneous upconversion crystals of high complexity by simply controlling the feeding of epitaxy precursor. For example, multicolor upconversion crystals can be generated by multi-step alternative feeding of epitaxy precursors of various doping-pairs, such as $\text{Yb}^{3+}/\text{Tm}^{3+}$, and $\text{Yb}^{3+}/\text{Er}^{3+}$. This strategy is workable because the epitaxy system allows the crystals to keep growing before reaching their maximum. Indeed, by use of multi-step feeding approaches, multi-color single crystals of five segments were successfully synthesized as shown in Figure 4.12a-c. Apart from the one-dimensional crystals, two-dimensional multicolor crystals can also be readily afforded following a similar multi-step epitaxy procedure (Figure 4.12d-f). However, the yield of the target product decreases as the complexity of the multicolor crystals getting high after multi-step reactions.

4.4 Conclusion

In conclusion, I developed a hydrothermal-based epitaxy approach that is able to produce upconversion heterogeneous crystals in large quantity and good quality. Based on a systematic study of the kinetics and thermodynamics of epitaxy in NaLnF_4 crystal system, two basic epitaxy habits that govern the epitaxial growth in hydrothermal condition were established. Such finding is able to guide one to synthesize upconversion crystals of high complexity on single-crystal level. Work in other material systems is underway to validate the generality of the epitaxy habits.

4.5 References

1. Dabbousi B. *et al.* (CdSe) ZnS core-shell quantum dots: synthesis and characterization of a size series of highly luminescent nanocrystallites. *J. Phy. Chem. B* 1997, **101**(46): 9463-9475.
2. Yan R, Gargas D, Yang P. Nanowire photonics. *Nature. Photon.* 2009, **3**(10): 569-576.
3. Wang J. *et al.* Epitaxial BiFeO₃ multiferroic thin film heterostructures. *Science* 2003, **299**(5613): 1719-1722.
4. Lauhon LJ, Gudiksen MS, Wang D, Lieber CM. Epitaxial core-shell and core-multishell nanowire heterostructures. *Nature* 2002, **420**(6911): 57-61.
5. Zhang F. *et al.* Direct imaging the upconversion nanocrystal core/shell structure at the subnanometer level: shell thickness dependence in upconverting optical properties. *Nano Lett.* 2012, **12**(6): 2852-2858.
6. Wang F. *et al.* Tuning upconversion through energy migration in core-shell nanoparticles. *Nat. Mater.* 2011, **10**(12): 968-973.
7. Li Z, Zhang Y. An efficient and user-friendly method for the synthesis of hexagonal-phase NaYF₄:Yb,Er/Tm nanocrystals with controllable shape and upconversion fluorescence. *Nanotechnology* 2008, **19**(34): 345606.
8. Jacob Z, Alekseyev LV, Narimanov E. Optical hyperlens: far-field imaging beyond the diffraction limit. *Opt. Express* 2006, **14**(18): 8247-8256.
9. Zhang C, Lee JY. Prevalence of anisotropic shell growth in rare earth core-shell upconversion nanocrystals. *ACS Nano* 2013, **7**(5): 4393-4402.
10. Fu J. *et al.* Controlled growth and up-conversion improvement of sodium yttrium fluoride crystals. *Eur. J. Inorg. Chem.* 2013, **2013**(8): 1269-1274.
11. Li C, Quan Z, Yang P, Yang J, Lian H, Lin J. Shape controllable synthesis and upconversion properties of NaYbF₄/NaYbF₄:Er³⁺ and YbF₃/YbF₃:Er³⁺ microstructures. *J. Mater. Chem.* 2008, **18**(12): 1353-1361.

12. Wang F. *et al.* Simultaneous phase and size control of upconversion nanocrystals through lanthanide doping. *Nature* 2010, **463**(7284): 1061-1065.

5 CHAPTER 5

Subwavelength Imaging Through Ion-beam Induced Upconversion Luminescence

5.1 Introduction

Photoluminescent probes play an indispensable role in labeling and manipulating biological species for many areas of application such as molecular imaging at the subcellular level, *in vivo* biodetection, and targeted intracellular delivery of therapeutics^{1,2}. In particular, lanthanide-doped upconversion nanocrystals have recently gained considerable attention for use as biomarkers due to their unique ability to convert low-energy light into high-energy photons, coupled with the absence of photobleaching and photoblinking³. However, an infrared laser, either in continuous- or pulsed-wave mode, is generally needed to implement photon upconversion. The use of the laser as the excitation source inevitably imposes an inherent constraint for high-resolution imaging because of the Abbe's diffraction limit⁴. Here we report, for the first time, the observation of photon upconversion through excitation of lanthanide-doped nanocrystals under a beam of helium ions. This approach enables simultaneous luminescence imaging and 3D mapping of cellular structures with a spatial resolution of sub-30 nm.

It has been well established that hexagonal-phase NaYF₄ is one of the most efficient host materials frequently utilized for preparing upconversion nanocrystals. The upconversion nanocrystals are typically doped with ytterbium (Yb³⁺) sensitizer ions, which absorb infrared radiation centering at 980 nm and non-radiatively transfer their absorption to activator ions such as thulium (Tm³⁺), erbium (Er³⁺) or holmium (Ho³⁺)^{5,6}. Prospects of the lanthanide-doped nanocrystals, including non-photobleaching, free of autofluorescence, tunable emission wavelengths and controllable phase-size, have exhibited unprecedented potential in a variety of research fields, especially for bioimaging and biomedical applications. However, the existing bioimaging studies were only confined to ensemble imaging, and any particulars on single nanoparticle level were therefore unachievable due to the resolution limitation resulting from the diffraction barrier of infrared excitation light in the case of conventional microscopy, or even confocal microscopy.

To overcome the diffraction limit, a variety of optical super-resolution techniques, for

instance stimulated emission depletion microscopy, have been developed⁷. Alternatives to optical super-resolution techniques involve using particle beam microscopy, such as electrons or ions, with the advantage that charged particles have much shorter de Broglie wavelengths⁸. For example, electron microscopy-based cathodoluminescence has been utilized successfully for high-resolution fluorescence imaging⁹. However, electrons suffer large angle scattering when interacting with matter, which in turn sacrifices the resolution, and therefore electron microscopy-based techniques are limited at imaging surface features or ultrathin slices.

In contrast, the use of mega-electron-volt (MeV) focused helium ions offers significant advantages, as MeV focused ions can pass through a thick biological sample (up to several microns) with very little deviation in their trajectories (Figure 5.2). Furthermore, we reason that ion beam as another form of energy can also induce luminescence, or even photon upconversion, in lanthanide-doped nanocrystals. Herein, we use MeV focused ion beam as the excitation source, to reveal the mechanisms of ion beam induced fluorescence in lanthanide-doped NaYF₄ nanocrystals. Furthermore, we utilize the high-resolution potential of MeV ions for subwavelength luminescence imaging.

5.2 Materials and Methods

5.2.1 Reagents

Yttrium(III) nitrate (99.9%), ytterbium(III) nitrate (99.9%), thulium(III) nitrate (99.9%), erbium(III) nitrate (99.9%), Yttrium(III) acetate hydrate (99.9%), ytterbium(III) acetate hydrate (99.9%), thulium acetate hydrate (99.9%), sodium hydroxide (NaOH, >98%), ammonium fluoride (NH₄F, >98%), oleic acid (90%) were all purchased from Sigma-Aldrich and used as received.

5.2.2 Synthesis of NaYF₄:Yb/Tm (x/y mol%) Nanorods.

The NaYF₄ microrods (~ 2 μm in length) were synthesized via hydrothermal reaction¹⁰. In a typical experiment, NaOH (0.3 g; 7.5 mmol) was first dissolved in 1.5 mL of DI water, followed by addition of 5 mL of oleic acid and 5 mL of ethanol under vigorous stirring.

Thereafter, an aqueous solution of NH_4F (2 M; 1 mL) was added to form a turbid mixture. Subsequently, a 2-mL aqueous solution of $\text{Y}(\text{NO}_3)_3$ ($\text{Yb}^{3+}/\text{Tm}^{3+} = x/y$ mol%; 0.2 M) was added and the solution was kept stirring for 20 min. The resulting mixture was then transferred into a 20-mL Teflon-lined autoclave and heated to 220 °C for 12 h. After cooling down to room temperature, the reaction product was isolated by centrifugation and washed with ethanol.

5.2.3 Synthesis of $\text{NaYF}_4:\text{Yb}/\text{Tm}$ (60/2 mol%) Nanoparticles

The NaYF_4 nanoparticles (~ 100 nm in diameter) were synthesized by a co-precipitation method¹¹. In a typical experiment, 3 mL of oleic acid and 7 mL of ODE were mixed with 2 mL aqueous solution of YCl_3 ($\text{Yb}^{3+}/\text{Tm}^{3+} = 60/2$ mol%; 0.2 M) in a 50 mL round-bottom flask under vigorous stirring. The resulting mixture was then heated to 150 °C for 1 h to form a transparent lanthanide oleate complex. After cooling down to room temperature, the complex colloidal was added into a methanol solution (6 mL) containing NH_4F (1.6 mmol) and NaOH (1 mmol), followed by evaporation of methanol at 100 °C under stirring. The resulted mixture was then heated to 300 °C and kept at that temperature for 2 h under a flow of nitrogen. The nanoparticles were precipitated by addition of ethanol and collected by centrifugation.

5.2.4 Physical Measurements

Those as-synthesized nanocrystals, including nanorods and nanoparticles, were examined under a transmission electron microscopy (TEM, JEM-2100F) operating at an acceleration voltage of 200 kV and a scanning electron microscopy (SEM, JEOL JSM-6701F) working at an acceleration voltage of 5 kV. Powder X-ray diffraction (XRD) data was recorded on a Siemens D5005 X-ray diffractometer with $\text{Cu K}\alpha$ radiation ($\lambda = 1.5406 \text{ \AA}$). Upconversion photoluminescence spectra were obtained by the use of a spectrometer (QE65000, Ocean Optics) equipped with a 980-nm continuous-wave diode lasers as the excitation source. Upconversion photoluminescence imaging was performed under an upright Olympus BX51 microscope coupled with a 980-nm diode laser through fiber output. The photoluminescence micrographs were recorded with a Nikon DS-Ri1 imaging system.

5.2.5 Ion-beam Microscopy Construction

The 1.6 MeV helium ion beam was produced by a High Voltage Engineering Europa Singletron ion accelerator, focused down to the sample by using a spaced triplet of compact Oxford Microbeams OM52 magnetic quadrupole lenses and scanned over the sample using electrostatic deflection (Figure 5.1a and 5.2b). Ion induced fluorescence in the sample was collected by a customized double-piece parabolic mirror, focused using a convergent lens down to the core of an optical fibre. Two 2 mm diameter holes were designed on each piece of the parabolic mirror to allow entering and exiting of the ion beam. Fluorescence light was guided out of the vacuum chamber ($\sim 10^{-6}$ mbar) by the fibre via an optical feedthrough. Fluorescent photons were then captured and detected by the Hamamatsu photomultiplier tube R7400P for ionoluminescence imaging or by the spectrometer (QE65000) for spectral measurement. A photon counting unit C9744 was used together with the PMT for counting the photons detected. The signal outputted from the C9744 unit was subsequently processed by an analog to digital converter before the acquisition by IONDAQ program for imaging. After interacting with the sample, directly transmitted ions were detected by a silicon charged-particle-detector (surface barrier, ORTEC[®]) located on the axis of the beam behind the sample for scanning transmission ion microscopy (STIM) imaging of the sample. The signal outputted from the surface barrier detector was first pre-amplified in case of being buried in the noise during the transmission. The pre-amplified signal was then converted to digitals by ADC 1 and inputted into IONDAQ for STIM imaging.

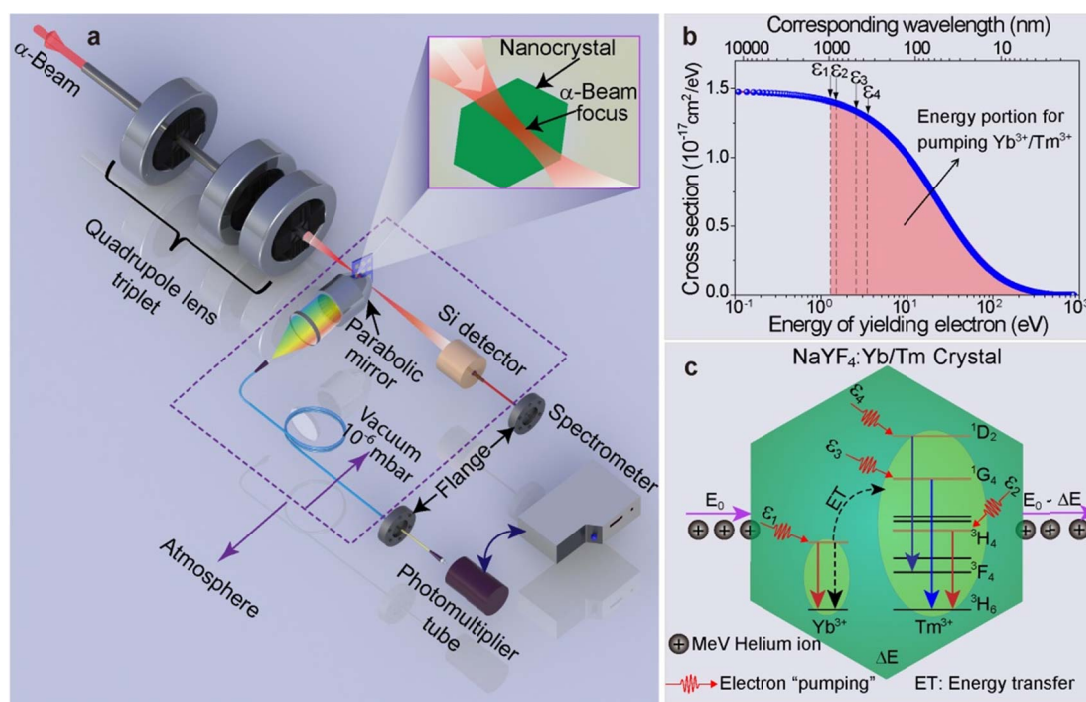


Figure 5.1 Experimental set-up and excitation-emission mechanism. (a) Schematic of the experimental set-up. A beam of MeV α -particles (He^+) was focused down to the sample by using a spaced triplet magnetic quadrupole lenses. The ion beam induced fluorescence in nanocrystals was collected by a customized double-pieced parabolic mirror and coupled into the fibre core. The fluorescence photons guided out of the vacuum (10^{-6} mbar) chamber were captured either by a photomultiplier tube for imaging or by a spectrometer for spectral measurement. Simultaneously, two aligned holes of the parabolic mirror allow the ion beam to enter the mirror, to penetrate in the sample and to exit the mirror. The exiting ions of certain energy-loss were detected by the Si surface barrier detector. (b) Energy distribution of the yielding electrons resulted from ionization process by the MeV α -particles in the nanocrystals, showing cross-sections of electrons with specific energies. (c) Proposed excitation-emission mechanism. The energetic ions (E_0) deposit certain amount of energy (ΔE) to the crystal, and causes ionization of atoms inside the crystal. Subsequently, by an electron-hole recombination process, the yielding electrons release and transfer their energy to lanthanide ions ($\text{Yb}^{3+}/\text{Tm}^{3+}$), making both Yb^{3+} and Tm^{3+} ions excited from their ground states. We term this process the ‘electron pumping’. At the same time, the excited Yb^{3+} up-converts its energy to surrounding Tm^{3+} ions, thus enhancing the population of excited states of Tm^{3+} , e.g., $^3\text{H}_4$, $^1\text{G}_4$, and $^1\text{D}_2$.

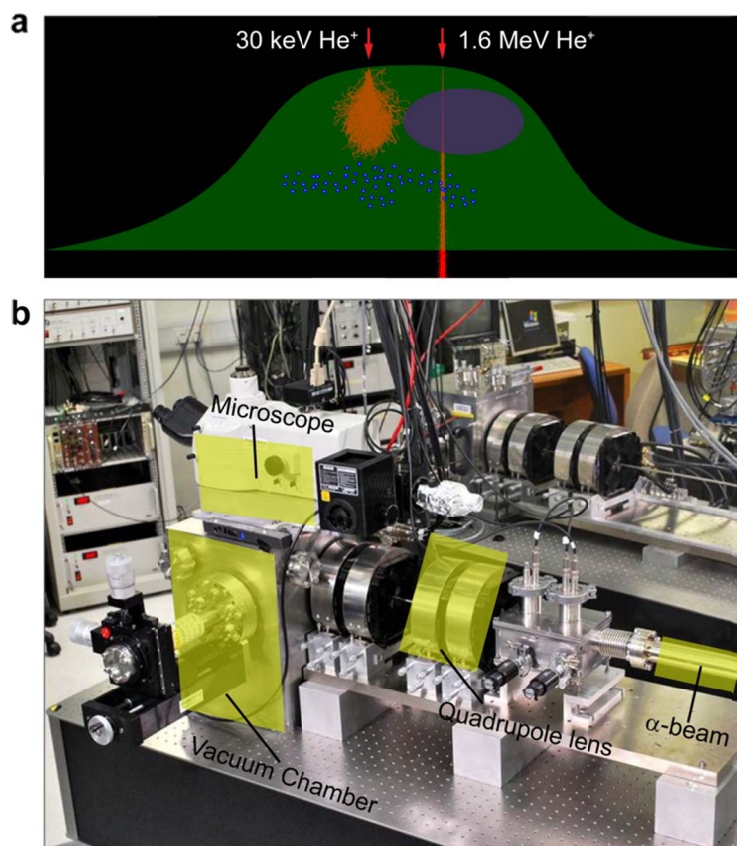


Figure 5.2 (a) Schematic showing the different penetration ability of slow (30 keV) and fast (1.6 MeV) α -beam. (b) Photograph of the home-made α -beam microscope. Briefly, the MeV α -beam was aligned by the quadrupole lenses, and then focused on the samples situated in a vacuum chamber. The generated luminescence was collected by a parabolic mirror, and subsequently directed into an optical fiber. These fluorescent signals were recorded by a photomultiplier tube or a spectrometer for imaging or spectral analysis purposes, respectively.

5.3 Results and Discussion

5.3.1 Theoretical Simulation on Energy Distribution of Ionized Electrons

Interaction of energetic helium ions (particles) with matter leads to a variety of energy-loss processes among which atomic ionization is the most dominant energy deposition channel¹². Therefore, only atomic ionization will be considered in this paper. To confirm that the ionization process in NaYF₄:Yb,Tm crystal is able to yield electrons holding sufficient energy to pump photon upconversion, we performed theoretical calculations on the energy distribution of the generated electrons using Hansen-Kocbach-Stolterfoht model⁹. Figure 5.1b shows that a yielding electron carrying energy larger than 1.265 eV (i.e., 980 nm in wavelength) holds a large portion (calculated as 97.5% of the probability) of the total cross section, suggesting a high possibility to generate upconversion luminescence through α -beam induced ‘electron pumping’. Based on energy matching principle, we propose an energy transfer mechanism in NaYF₄:Yb,Tm crystal system (Figure 5.1c). It should be pointed that for those yielding electrons whose energy is higher than 1.265 eV but not matches the absorption of Yb³⁺/Tm³⁺, they may further lose their energy by processes like ionization, collision and phonon generation, till producing a matching energy that can be used to pump Yb³⁺ or Tm³⁺.

5.3.2 Experimental Evidence for Ionoluminescence

To validate the above proposition, we prepared a set of NaYF₄:Yb,Tm nanorods via a hydrothermal procedure, and systematically investigated their spectroscopic property under α -beam excitation. Scanning microscopic imaging suggests that the size of the as-synthesized hexagonal-phase nanorods exhibits a uniform distribution (Figure 5.4a). When doped Yb³⁺ or Tm³⁺ as single activators, these nanorods give rise to characteristic emissions of Yb³⁺ or Tm³⁺, respectively (Figure 5.4b, upper two panels). These results verify that both Yb³⁺ and Tm³⁺ can directly harvest the energy of yielding electrons from α -beam excitation, which displays a superior prospect over the 980-nm laser excitation since 980-nm laser only allows Yb³⁺ to act as an energy harvester (Figure 5.3). Interestingly, in Yb/Tm (60/2 mol%) co-doped case, the

visible emission (450 nm and 480 nm) of Tm^{3+} displays a prominent enhancement when compared to Tm (2 mol%) singly-doped sample. It is then reasonable to conclude that the presence of Yb^{3+} enhances the Tm emissions at short wavelength. To shed more light on this point, we prepared a series of $\text{NaYF}_4:\text{Yb,Tm}$ nanorods with varied Yb-doping concentrations (10-98 mol%) while keeping Tm-doping concentration of 2 mol% as constant. We collected their luminescence spectra under α -beam excitation, and integrated the overall emission intensities (I_{Tm} and I_{Yb}) of Tm and Yb ions, respectively (Figure 5.5a). The intensity ratios, $I_{\text{Tm}}/I_{\text{Yb}}$, were plotted against Yb-doping concentrations to show the relative intensity change of Tm and Yb emissions. Note that the relative ratio metric is the only meaningful tool in such spectral analysis since the uncertainty of excited sample amount makes the absolute intensity values incomparable. As shown in Figure 5.5b, the intensity ratio ($I_{\text{Tm}}/I_{\text{Yb}}$) increases from 3.3 to 10.2 as Yb-doping concentration increases from 10 mol% to 50 mol%, and then decreases down to 3.3 as Yb-doping concentration further increases to 98 mol%. Such inverse parabolic profile provides a strong evidence for the energy transfer between Yb and Tm ions¹³. Particularly, the rising stage of $I_{\text{Tm}}/I_{\text{Yb}}$ indicates the energy transfer from Yb to Tm, resulting in a pronounced enhancement in short wavelength. Therefore, we term this process as another form of energy “upconversion”. The descending stage of $I_{\text{Tm}}/I_{\text{Yb}}$ can be explained by the back-energy-transfer from Tm to Yb ion as Yb-doping concentration increasing, analogous to the scenario in photon upconversion process when using 980-nm laser as the excitation source¹⁴. On a separate note, the ratio metric analysis of these luminescence spectra also suggests an optimal Yb-doping concentration for imaging purpose. For example, the sensitive range of the photon detector (Hamamatsu PMT R7400P) for imaging falls into the visible range from 400 nm – 750 nm. To obtain a strong signal from lanthanide-doped nanocrystals, the NaYF_4 sample with Yb/Tm (60/2 mol%) doping was adapted for alpha-beam microscopic imaging since its visible emission takes up over 40% out of the total emission (Figure 5.5c).

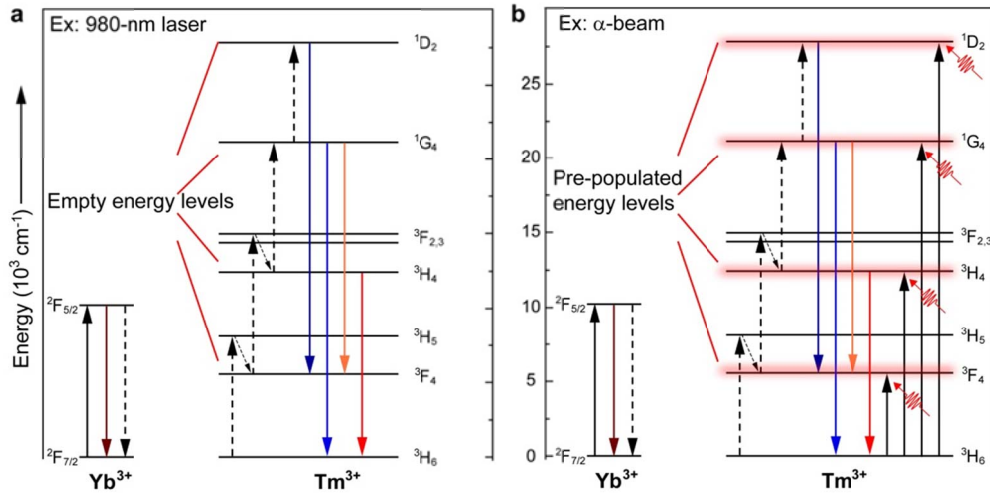


Figure 5.3 Superior prospect of α -beam excitation over 980-nm laser. **(a)** Energy diagram showing a typical energy transfer upconversion (ETU) process in NaYF₄:Yb/Tm crystal when excited by a 980-nm laser. ETU features a ladder-like process in which energy levels were populated and accumulated in a from-low-to-high manner. **(b)** Energy diagram showing the energy transfer process in NaYF₄:Yb/Tm crystal when excited by an α -beam. Unlike the interaction between 980-nm laser and crystal in ETU process, the interaction between α -beam and crystal lattice produce a large number of excitons, carrying energies ranging from 0.1 eV to 1000 eV. Such energies not only populate a large number of Yb ions, but also populate a substantial amount of Tm ions prior to ETU process from Yb³⁺ to Tm³⁺, largely enhancing the energy upconversion process.

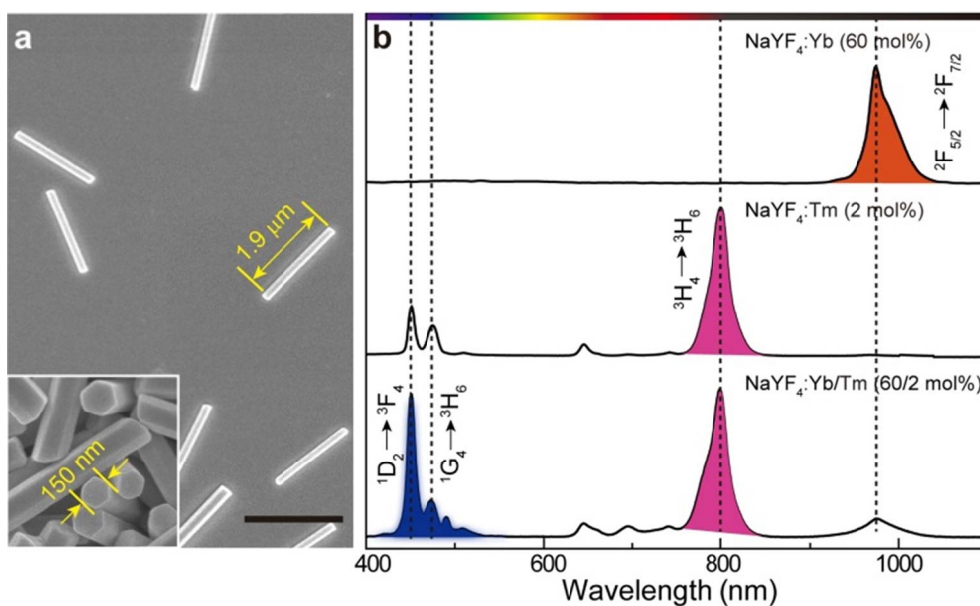


Figure 5.4 Spectral verification and optimization of doping concentration. **(a)** Scanning electron microscopy image of the as-synthesized Yb³⁺/Tm³⁺ doped NaYF₄ nanorods for spectral study. The inserted image shows hexagonal cross sections of these nanorods with a width of about 150 nm and length of about 1.9 μm. The sizes are much depended on doping concentrations. The scale bar is 2 μm. **(b)** Spectra of the nanorods with different doping strategies of Yb³⁺ and Tm³⁺: singly-doping and binary-doping strategy. When singly-doped with Tm³⁺ or Yb³⁺, the nanorods show the emission respectively, indicating both Yb³⁺ and Tm³⁺ can absorb the energy released from excitons induced by α-particles. In the binary-doped case, i.e., NaYF₄:Yb/Tm (60/2 mol%), the blue emissions, i.e., 480 nm (¹G₄ → ³H₆) and 450 nm (¹D₂ → ³F₄), originated from Tm³⁺ are enhanced, indicating that Yb³⁺ plays an significant role to up-convert its energy into ¹D₂ of Tm³⁺.

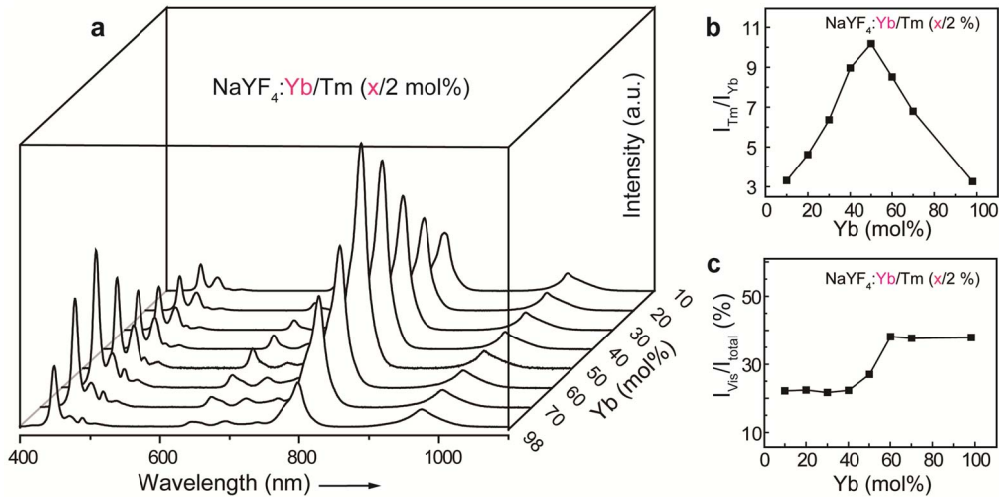


Figure 5.5 Spectroscopic investigation of upconversion luminescence in NaYF₄:Yb/Tm crystals under α -beam excitation. **(a)** Luminescence spectra of NaYF₄:Yb/Tm crystals under α -beam excitation, showing a strong intensity dependence on Yb-doping concentration. **(b)** Integrated intensity ratio of characteristic emissions from Tm and Yb was plotted against Yb-doping concentrations. **(c)** Optimization of Yb-doping concentration for maximum emission output in the visible range (400-750 nm). In order to obtain a high response in signal acquisition for PMT, 60 mol% of Yb-doping concentration was selected as the optima for imaging purpose.

5.3.3 Subwavelength Imaging of Upconversion Nanorods

Except for the merits of MeV α -beam discussed above, advantage can also be taken for high-resolution imaging since the α -beam can be readily focused down to sub-30 nm in spot size^{15,16}. In a proof-of-concept experiment for subwavelength resolution demonstration, images of NaYF₄:Yb/Tm (60/2 mol%) nanorods were taken at a fluence of around 15000 helium ions per second, and recorded in 512 × 512 pixel arrays by detecting the α -particles induced fluorescence (ionoluminescence) (Figure 5.6d-e). The nanorod in Figure 5.6e was selected and magnified from the box region depicted in Figure 5.6d. To ascertain the resolution of the ionoluminescence images, the intensity point spread function along the arrow (Figure 5.6d) was extracted and fitted using a modified Gaussian model⁹. The lateral resolution was determined to be the full width at half maximum (FWHM), around 28 nm. These results indicate that ionoluminescence technique is able to image the lanthanide-doped nanorods with a spatial resolution of at least 30 nm. In comparison, the images of the same sample area were taken by conventional optical microscopy equipped with 980 nm diode laser (Figure 5.6a). The fitted FWHM using the same nanorod was measured to be 253 nm (Figure 5.6b-c), exhibiting a typical diffraction limited resolution. The subwavelength resolution of α -beam microscopy can be instantly verified by the comparison in image clarity (Figure 5.6b and e).

To take advantage of the 30 nm spatial resolutions imaging capability of α -beam microscopy, we need to ensure that iono-bleaching, which is a measure of reduction in photon emission under ion exposure, does not pose a major obstacle. These nanorods can remain about 80% of initial fluorescence intensity after exposing in the ion beam half an hour or so (data not shown). It should be pointed out that, within the first 11 minutes (1.5×10^{14} ions/cm²), a good quality image can be already achieved with less than 10% iono-bleaching, indicating that NaYF₄:Yb/Tm nanocrystals are substantially stable to iono-bleaching, thus are very suitable for ionoluminescence imaging.

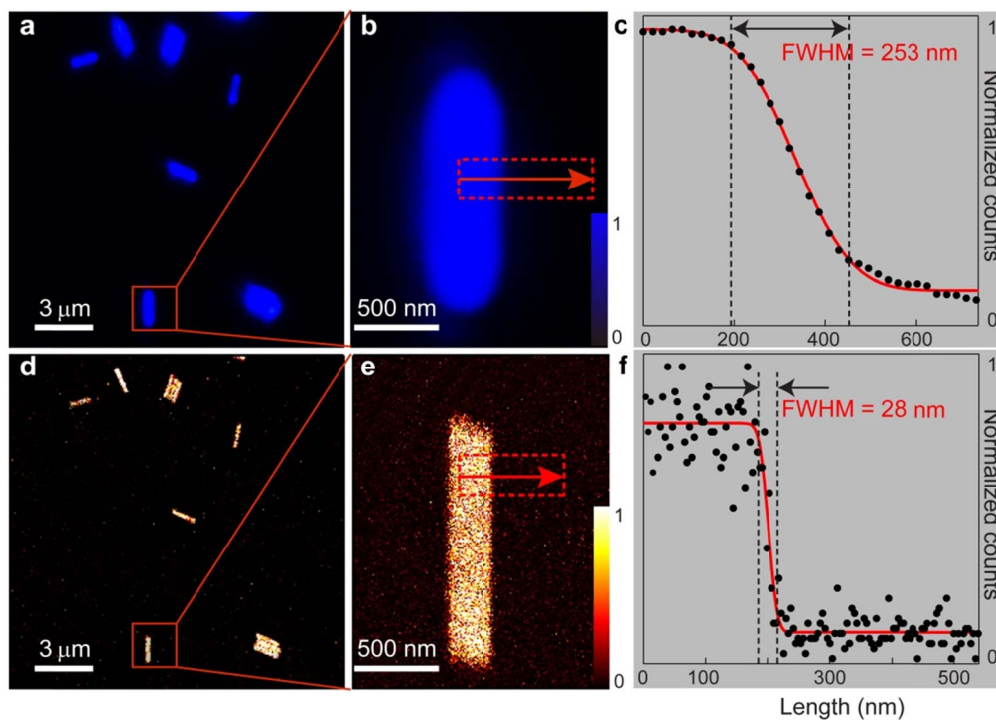


Figure 5.6 Ionoluminescence imaging and ionobleaching of $\text{NaYF}_4:\text{Yb/Tm}$ (60/2 mol%) nanorods. (a) Conventional microscopy fluorescence image taken by 980 nm diode laser excitation. (b) Optical fluorescence image extracted from the box region in a. (c) Intensity spread function along the red arrow in b, showing a 253 nm resolution of the conventional optical microscopy. (d) Ionoluminescence image of the same sample area to a, but taken under α -beam excitation through a scanning mode. (e) Ionoluminescence image extracted from the box region in d. (f) Intensity spread function along the red arrow in e, showing a 28 nm resolution of the α -beam microscopy.

5.3.4 Subwavelength Imaging of Upconversion Nanocrystals in Cell

The ability of MeV helium ion beam to induce efficient upconversion and image the lanthanide-doped nanorods at sub-30 nm spatial resolution without distinct iono-bleaching makes it a promising tool for nanoscale imaging applications. Importantly, the combination use of scanning transmission ion microscopy (STIM) and ionoluminescence techniques enables us to do structural and fluorescence imaging of a whole cell simultaneously. As a proof of concept, we imaged human cervical carcinoma cells (Hela) that had been exposed to NaYF₄:Yb/Tm (60/2 mol%) nanoparticles of mean diameter 95 ± 12 nm (Figure 5.7a). The HeLa cells were seeded on 100 nm thick silicon nitride windows, dehydrated by critical point drying, and scanned using a 1.6 MeV helium ion beam focused to sub-30nm spot sizes (Figure 5.7b). By detecting the energy loss of forward transmitted ions using the Si surface barrier detector, a density map of the cell can be generated using STIM. Thereafter, a three dimensional presentation of the density map can be produced, showing the cellular structural information (bottom in Figure 5.7b). At the same time, α -particles induced fluorescent photons can be captured by the PMT, and a fluorescence map of nanoparticles inside the cell can be then produced pixel by pixel using ionoluminescence technique (top left in Figure 5.7b). The coupling of STIM and ionoluminescence imaging technique allows us to locate the nanoparticles inside the whole cell by merging the fluorescence image and density maps as shown in Figure 5.7c. Additionally, it is worth noting that, due to the high-resolution imaging ability of ionoluminescence imaging technique, single nanoparticles inside the cell can be resolved (marked with arrows, bottom left image of Figure 5.7c), and separation between nanoparticles or clusters of nanoparticles can also be differentiated. As a comparison of the resolution, fluorescence image with the same area taken by a conventional microscopy equipped with a 980 nm diode laser is also shown in Figure 5.7c (top left). This image was extracted from the fluorescence image of the same individual nanorod, showing a much poor resolution limited by the diffraction barrier of light.

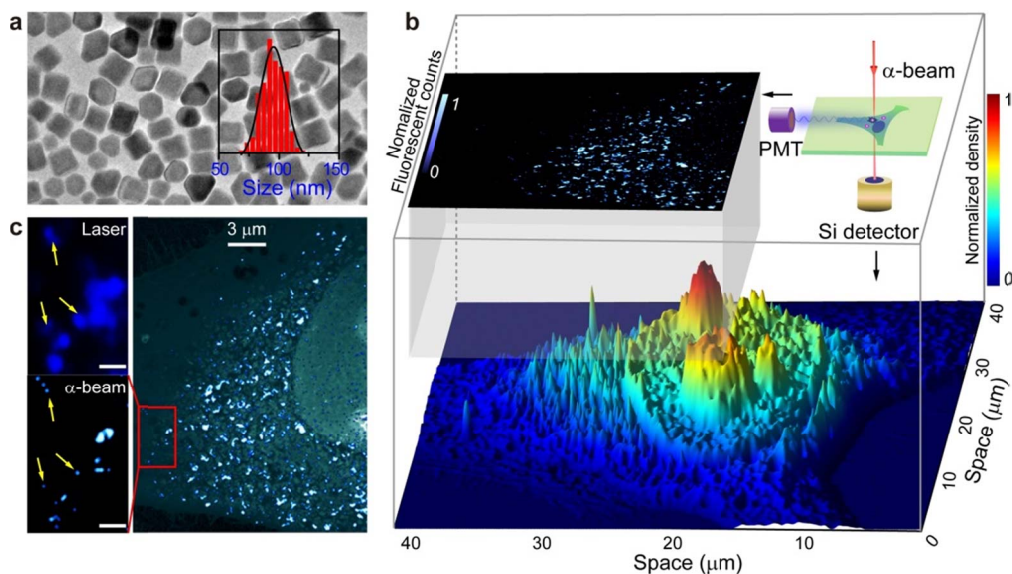


Figure 5.7 Simultaneous structure and fluorescence imaging in a single HeLa cell. **(a)** Transmission electron microscopy image of the as-synthesized NaYF₄:Yb/Tm (60/2 mol%) nanoparticles. The inserted histogram shows size distribution (mean diameter of 95 ± 12 nm) of these nanoparticles. **(b)** Simultaneous structure and fluorescence imaging in a whole HeLa cell with the uptake of nanoparticles shown in **a**. By detecting the energy loss of forward transmitted ions using the Si surface barrier detector, a density map of the cell can be generated using scanning transmission ion microscopy (STIM). A three dimensional presentation of the density map shows the cellular structural information (bottom). At the same time, α -particles induced fluorescent photons can be captured by the PMT and a fluorescence map of nanoparticles inside the cell can be then generated (top left). **(c)** Fluorescence image overlapped with the structural image (STIM) showing the location of nanoparticles inside the cell (right). In the ionoluminescence image (bottom left), single nanoparticles (marked by arrows) can be resolved, showing a much higher resolution against the conventional 980 nm diode laser induced fluorescence image (top left). The bottom left ionoluminescence image was magnified from the red box region depicted in the right overlapped image. Scale bars in the left two images are 1 μ m.

5.4 Conclusion

In conclusion, we have demonstrated that the upconversion nanocrystals NaYF₄:Yb/Tm can be driven by MeV α -particles. Intriguingly and importantly, the pre-population of the excited states of Tm³⁺ stemming from direct absorption can significantly facilitate the up-converting processes, making the upconversion more efficient compared with infrared pumping, e.g., 980 nm diode laser. Additionally, the MeV ion beam has the ability to image the lanthanide-doped nanorods at sub-30 nm spatial resolution without distinct ion-bleaching, providing a promising prospect for high resolution imaging probed by lanthanide-doped nanocrystals. It is also deserved to be specially mentioned that, by using lanthanide-doped nanoparticles as the fluorescent probes, simultaneous structure and fluorescence imaging of a whole cell with high-resolution, has been successfully achieved using our newly developed ionoluminescence technique using together with STIM. We believe that our demonstration will provide an important step forward for fluorescent nanoparticles probed biological and biomedical studies at the single whole cell level, for example the quantified statistic of intracellular bio-distribution of drugs in the field of targeted drug delivery.

5.5 References

1. Alivisatos P. The use of nanocrystals in biological detection. *Nat. Biotech.* 2004, **22**(1): 47-52.
2. Atreya R. *et al.* In vivo imaging using fluorescent antibodies to tumor necrosis factor predicts therapeutic response in Crohn's disease. *Nat. Med.* 2014, **20**(3): 313-318.
3. Auzel F. Upconversion and anti-Stokes processes with f and d ions in solids. *Chem. Rev.* 2004, **104**(1): 139-173.
4. Caillat L. *et al.* Multiphoton upconversion in rare earth doped nanocrystals for sub-diffractive microscopy. *Appl. Phy. Lett.* 2013, **102**(14): 143114.
5. Gnach A, Bednarkiewicz A. Lanthanide-doped up-converting nanoparticles: Merits and challenges. *Nano Today* 2012, **7**(6): 532-563.
6. Liu J-n. *et al.* Simultaneous nuclear imaging and intranuclear drug delivery by nuclear-targeted multifunctional upconversion nanoprobos. *Biomaterials* 2012, **33**(29): 7282-7290.
7. Rittweger E, Han KY, Irvine SE, Eggeling C, Hell SW. STED microscopy reveals crystal colour centres with nanometric resolution. *Nature Photon.* 2009, **3**(3): 144-147.
8. Udalagama CNB. *et al.* An automatic beam focusing system for MeV protons. *Nuclear Instruments and Methods in Physics Research Section B: Beam Interactions with Materials and Atoms* 2005, **231**(1-4): 389-393.
9. Udalagama C, Bettiol A, Watt F. Stochastic spatial energy deposition profiles for MeV protons and keV electrons. *Physical Review B* 2009, **80**(22): 224107.
10. Zhang Y. *et al.* Multicolor barcoding in a single upconversion crystal. *J. Am. Chem. Soc.* 2014, **136**(13): 4893-4896.
11. Wang F, Deng R, Liu X. Preparation of core-shell NaGdF₄ nanoparticles doped with luminescent lanthanide ions to be used as upconversion-based probes. *Nat. Protocols* 2014, **9**(7): 1634-1644.
12. Tringe JW. *et al.* Radiation damage mechanisms for luminescence in Eu-doped GaN.

J. App. Phy. 2007, **101**(5): 054902.

13. Zhao J. *et al.* Single-nanocrystal sensitivity achieved by enhanced upconversion luminescence. *Nat. Nanotechnol.* 2013, **8**: 729-734.

14. Wang F, Liu X. Upconversion multicolor fine-tuning: visible to near-infrared emission from lanthanide-doped NaYF₄ nanoparticles. *J. Am. Chem. Soc.* 2008, **130**(17): 5642-5643.

15. Chen X. *et al.* High-resolution 3D imaging and quantification of gold nanoparticles in a whole cell using scanning transmission ion microscopy. *Biophys. J.* 2013, **104**(7): 1419-1425.

16. Chen X. *et al.* Whole-cell imaging at nanometer resolutions using fast and slow focused helium ions. *Biophys. J.* 2011, **101**(7): 1788-1793.

6 CHAPTER 6

Conclusion and Outlook

The primary work in this thesis was focused on the epitaxial growth of NaLnF_4 crystals, including zero-dimensional, one-dimensional, and two-dimensional crystals. Two epitaxy systems, including oil-based co-precipitation and hydrothermal-based epitaxy system, were examined in terms of epitaxy speed, dimension, and orientation, respectively. These epitaxy experiments readily afford a large amount of heterogeneous crystals of high uniformity in a bottom-up manner. The usefulness of these heterogeneous single-crystals was demonstrated in each individual chapter.

In Chapter 2, a class of core@shell NaYF_4 nanocrystals was generated by 0-D epitaxy technique in an oil-based co-precipitation system. These heterogeneous nanostructures are particularly useful in thermal diffusion experiment because the diffusion of lanthanide ions through core/shell interface can be sensitively reflected on their upconversion luminescence spectra. Several control experiments indirectly prove the significant role of heterogeneous structure during thermal diffusion process.

In Chapter 3, a set of nanorods with spatially resolvable colors were generated by 1-D epitaxy technique in a hydrothermal reaction. These nanorods were demonstrated to be particularly useful in anti-counterfeiting application. On a separate note, the use of multicolored rods as cell tags was also demonstrated, which extends the scope of current cell labelling agents.

In Chapter 4, heterogeneous NaLnF_4 microplates were prepared by 2-D epitaxy technique in a hydrothermal environment. By taking advantage of the large crystal size, the epitaxy orientation was instantly verified by using a conventional optical microscope. The kinetic and thermodynamic behaviors of epitaxial growth were systematically investigated, which suggests several epitaxy habits. The epitaxy habits were further utilized to guide the

synthesis of multicolor upconversion particles with versatile control over both dimension and epitaxy orientation.

In Chapter 5, upconversion nanocrystals, including nanorods and nanoparticles, were used as luminescent probes for subwavelength imaging purpose. Instead of commonly used NIR lasers, ion-beam was used as another form of excitation source for luminescence generation. The mechanism of ionoluminescence from lanthanide-doped nanocrystals was explored by a careful comparison of luminescence spectra arising from samples of various doping concentrations. It was found that both energy upconversion and downconversion contribute to the ionoluminescence generation.

In summary, this thesis presents a systematic study on crystal epitaxy of NaLnF_4 material system. Among many epitaxy parameters such as lanthanide species, morphology of seeding crystals and epitaxy environment, it was found that the epitaxy environment plays a dominant role in governing both epitaxy dimension and epitaxy orientation. These findings allow us to fine control the epitaxy behavior in NaLnF_4 crystal systems, and to produce a class of heterogeneous nano- or micro- structures on single-crystal level. The single-crystal nature of the heterogeneous crystals may render a class of optical units for advanced applications in microcavity-based lasers or polarized-waveguide-based optical devices.

Current epitaxy study on upconversion crystals has been boosted by a large body of experimental data involving core@shell structures, segmented microrods, and encaged microdisks. External epitaxy environment has been demonstrated as a significant factor in the control of the epitaxial orientation. However, other intrinsic factors including lattice mismatch and bonding strength remain untouched. Such a challenging topic may provide both a future direction to crystal epitaxial growth and a deep insight to involved mechanism.

I. Curriculum Vitae

Personal Information

Name: Yuhai Zhang

Date of birth: 09/1984

Nationality: China

Major: Chemistry

Email: zyh628628@gmail.com

Address: Department of Chemistry, National University of Singapore ,
3 Science Drive 3, Singapore 117543

Education

Aug. 2011 ~ Jul. 2015 Ph. D. candidate

Department of Chemistry, National University of Singapore (with Dr. Xiaogang Liu)

Sep. 2008 ~ Jul. 2010 M.Eng., Bionano Technology

Kyungwon University, Seongnam, South Korea

Sep. 2003 ~ Jul. 2007 B.Sc., Chemistry

Shandong University, Jinan, Shandong, China

Research Projects

- Thermal diffusion study in upconversion core@shell nanocrystals through the use of zero-dimensional epitaxy technique.
- Multicolor barcoding in a single upconversion microrod by the use of one-dimensional epitaxy technique.
- The quest for crystal epitaxy habits: a case study in two-dimensional lanthanide-doped microcrystals.
- Subwavelength image through ion-beam induced luminescence from lanthanide-doped nanocrystals.

II. List of Publications

1. Liu, D., Xu, X., Du, Y., Qin, X., **Zhang, Y.**, Ma, C., Wen, S., Ren, W., Goldys, E., Piper, J., Dou, S., Liu, X., & Jin, D. Three-dimensional controlled growth of monodisperse sub-50 nm heterogeneous nanocrystals. *Nature Communications*. 2015, in press.
2. Mi, Z., **Zhang, Y. (co-first-author)**, Vanga, S., Chen, C., Tan, H., Watt, F., Liu, X., & Bettiol, A. A. Subwavelength imaging through ion-beam-induced upconversion. *Nature Communications*. 2015, in press.
3. Liu, X., Deng, R., **Zhang, Y.**, Wang, Y., Chang, H., Huang, L., & Liu, X. Probing the nature of upconversion nanocrystals: instrumentation matters. *Chemical Society Reviews*. 2015, *44*, 1479-1508.
4. **Zhang, Y.**, Zhang, L., Deng, R., Tian, J., Zong, Y., Jin, D., & Liu, X. Multicolor barcoding in a single upconversion crystal. *Journal of the American Chemical Society*. 2014, *136*, 4893.
5. **Zhang, Y.**, & Liu, X. Nanocrystals: Shining a light on upconversion. *Nature Nanotechnology*. 2013, *8*, 702. (Research highlight).
6. **Zhang, Y.**, Son, S. J., & Ju, H. Anodized aluminum oxide membranes of tunable porosity with platinum nanoscale-coating for photonic application. *Current Applied Physics*, 2012, *12*, 1561-1565.
7. **Zhang, Y.**, & Son, S. J. Fluorescent magnetic silica nanotubes with high photostability prepared by the conventional reverse micro-emulsion method. *Bull. Korean Chem. Soc*, 2012, *33*, 4165.
8. Namgung, R., **Zhang, Y.**, Fang, Q. L., Singha, K., Lee, H. J., Kwon, I., Jeong, Y., Park, I., Son, S., & Kim, W. Multifunctional silica nanotubes for dual-modality gene delivery and MR imaging. *Biomaterials*, 2011, *32*, 3042-3052.

III. Symposia/Conferences Attended

1. Poster presentation at “International Symposium on Optoelectronics, Materials, and Energy (iSOME-2014)” organized by Nanjing Tech University, Nanjing, China, 2014.
2. Poster presentation at the International Conference “7th International Conference on Materials for Advanced Technologies” organized by The Materials Research Society of Singapore, Singapore, 2013.
3. Poster presentation at the International Conference “41st International Conference on Coordination Chemistry (ICCC 41)” organized by Singapore National Institute of Chemistry (SNIC), Singapore, 2014.